**Wafer-Scale Alignment of Semiconducting Carbon Nanotubes from Solution**

By

**Katherine R. Jinkins**

A dissertation submitted in partial fulfillment of
the requirements for the degree of

**Doctor of Philosophy**
**(Materials Science)**

at the

**UNIVERSITY OF WISCONSIN-MADISON**

**2020**

Date of final oral examination: 07/17/2020

The dissertation is approved by the following members of the Final Oral Committee:

**Michael S. Arnold**, Professor, Materials Science and Engineering
**Arganthaël Berson**, Lecturer, Mechanical Engineering
**Padma Gopalan**, Professor, Materials Science and Engineering
**Irena Knezevic**, Professor, Electrical and Computer Engineering
**Reid Van Lehn**, Assistant Professor, Chemical and Biological Engineering

# Abstract

Carbon nanotubes are unique one-dimensional materials that exhibit extraordinary properties, including high stability, large elastic modulus, and exceptional charge and thermal transport, making them promising candidates for future mechanical, optical, and electronic devices. Electrical measurements of individual nanotubes have demonstrated room-temperature ballistic conductance and 3× higher current density than state-of-the-art Si field-effect transistors (FETs). While these results are exciting; to achieve the high on-current required for future carbon nanotube technologies to become viable, electronic devices must incorporate multiple nanotubes aligned in parallel. Alignment is especially critical to minimize sheet resistance and reduce charge carrier scattering in devices. However, the alignment of carbon nanotubes at intermediate packing densities in a scalable technique has plagued the electronics community for decades. In this work, we develop, explore, and elucidate three possible solutions to this long-standing challenge.

First, we elucidate the mechanism of the floating evaporative self-assembly (FESA) technique, in which stripes of aligned nanotubes are deposited onto substrates by dosing a carbon nanotube ink at a water/substrate interface. We track the key interfaces directly at the substrate during FESA and show that the nanotube alignment occurs from the buried ink/water interface. We also demonstrate improved control over the bandwidth and band spacing of aligned carbon nanotubes and align nanotubes across a 2.5 × 2.5 $cm^2$ substrate, an important step towards high-volume production. Ultimately, though, FESA cannot yield uniform, continuous films of aligned nanotubes over the wafer-scale, so other techniques are explored.

We use the understanding gained toward the FESA mechanism to develop another alignment technique, tangential flow interfacial self-assembly (TaFISA), to fabricate uniform films of highly aligned carbon nanotubes for short channel FETs. In this process, we demonstrate that an ink/water interface can induce liquid crystal assembly of carbon nanotubes. Flowing this two-dimensional nematic assembly of nanotubes, globally aligns the nanotubes. By translating a substrate through this flowing ink/water interface, uniform films of highly aligned (within ±5.7°) nanotubes are deposited across 10 cm wide substrates. Due to the underlying lyotropic liquid crystal phenomena, the nanotube ordering improves with increasing concentration and decreasing temperature. The exceptional alignment leads to excellent FET performance with high on-state current density averaging 520 µA $µm^{-1}$ at a $V_{DS}$ of -0.6 V. We also perform a more detailed investigation of experimental parameters that can affect the interfacial assembly, including nanotube ink solvent, substrate surface water contact angle, and modification of the water subphase.

We also study the effect of shear on nanotube ink, without the ink/water interface as used in the FESA and TaFISA technique. We elucidate the effect of shear rate on nanotube alignment and find that the alignment increases with increasing shear rate following a power law dependence. We also demonstrate control over the nanotube packing density by tailoring the carbon nanotube ink concentration and ink volume. FETs are fabricated with their charge transport direction parallel and perpendicular to the alignment. The parallel FETs exhibit 7× faster charge carrier mobility of 101 $cm^2\ V^{-1}\ s^{-1}$, while also simultaneously displaying high on/off ratio of $10^5$. Deposition conditions are extensively optimized to enable alignment within a ± 27° window at nearly ideal packing density of 50 nanotubes $µm^{-1}$ over large-area 10 × 10 $cm^2$ substrates. These quasi-aligned films are promising candidates for long-channel FETs (e.g., in displays, sensors, and flexible electronics), where some misalignment is necessary to allow charge percolation.

We additionally report our work utilizing solution-based shear to fabricate ultrathin films of aligned cellulose nanocrystals. Cellulose nanocrystals (CNC) exhibit excellent mechanical and piezoelectric properties, making this material attractive for use in high-performance coatings. Toward this goal, we use confined shear-based alignment to fabricate ultrathin films of aligned CNC. The shear rate is varied from 19 to 19000 $s^{-1}$ to improve the half-width at half-maximum of the spread in CNC alignment from 130 to 30°. The CNC solution volume and concentration are both used to independently control the film height.

# Acknowledgments

This work would not be possible without the mentorship, support, and encouragement of many people, some of whom I list here.

First, I would like to thank the members of my committee, Prof. Mike Arnold, Dr. Arganthaël Berson, Prof. Padma Gopalan, Prof. Irena Knezevic, and Prof. Reid Van Lehn for providing vital feedback and help to guide my research and thesis.

I would like to thank all the former and current Arnold group members for all of their advice, help, and friendship, including: Dr. Nate Safron, Dr. Robert Jacobberger, Dr. Meng-Yin Wu, Dr. Gerald Brady, Dr. Matt Shea, Dr. Jialiang Wang, Dr. Austin Way, Vivek Saraswat, Andrew Witte, Tsuyoshi Takahashi, Sean Foradori, Abitha Dhavamani, Frederick Li, Xiaoqi Zheng, and Dr. Shalini Lal. I would also like to thank the multiple undergraduate students I had the pleasure of working with during my time at the University of Wisconsin-Madison, including: Alvin Lee, Johan Holm, Jason Chan, Thomas Sabel, Turner Williams, Deming Kong, John McGinley, Shuai Yuan, Casey Brown, Maxwell Goldberg, Samantha Joers, Vanessa Meschke, Emily Proehl, and Shunzhang Li.

Additionally, I would like to thank all of our extremely productive collaborators, including Dr. Arganthaël Berson at the University of Wisconsin-Madison, Prof. Padma Gopalan and students Dr. Jonathan Choi, Dr. Wei Wei, Jonathan Dwyer, and Anjali Suresh at the University of Wisconsin-Madison, Prof. Hal Evensen and Kjerstin Gronski at the University of Wisconsin-Platteville, and Prof. Chongwu Zhou and Zhen Li at the University of Southern California.

I would like to thank my amazing undergraduate mentors and research advisors, Prof. Yan Wu and Prof. James Hamilton at the University of Wisconsin-Platteville, Prof. Edward Conrad at the Georgia Institute of Technology, Prof. Rainer Fries at Texas A&M University, and my many supportive undergraduate professors including: Prof. Hal Evensen, Prof. Gokul Gopalakrishnan, Prof. Tomm Scaife, and Prof. W. Doyle St. John for teaching me how to conduct research, preparing me for graduate school, and being exceptional mentors who encouraged me to work hard to achieve my goals.

I would like to thank my family, and especially my parents, Richard and Patricia Jinkins, who have encouraged me from day 1 to dream big and strive for excellence in everything I attempt. Your love and support have been instrumental to my success and happiness in life.

I am grateful for the financial support for my graduate studies from the National Science Foundation for a Graduate Research Fellowship, and the University of Wisconsin-Madison for a Wisconsin Distinguished Graduate Fellowship.

I would like to especially thank my advisor, Mike Arnold. You have been best graduate advisor I could have hoped for. You have pushed me to be a better researcher, writer, and scientist and your enthusiasm for science and ‘exciting results’ has always been contagious and made the long hours and late nights much easier. Thank you for mentoring me and helping me succeed in my graduate research.

Finally, and most importantly, I would like to thank my husband, Bobby. You have always been there for me throughout my PhD and I cannot begin to describe how thankful I am for all your help and encouragement. You have kept me well-fed, provided scientific feedback on experiments and papers, ensured I took time to relax, and helped me always remember and focus on the truly important parts of life, such as spending time with you. I love you. Thank you.

# Table of contents

# List of figures

**Figure 2.3**. Dose FESA is a controllable process for nanotube alignment. (a) Interband spacing and bandwidth as a function of substrate lift rate. Bandwidth is invariant while interband spacing increases linearly with lift-rate. (b) SEM micrographs of substrates prepared using lift rates of 5, 11, and 15 mm $min^{-1}$. The aligned bands are black in these micrographs.

**Figure 2.4**. (a) Bandwidth and packing density of deposited aligned nanotubes increase with increasing concentration. Packing density initially increases and then quickly saturates at ~24 nanotubes $\mu m^{-1}$. (b) SEM micrographs showing packing density and alignment at 0.75 and 7 μg $mL^{-1}$. (c-d) Traces of ink/air/substrate and ink/water/substrate contact lines in the frame of the substrate from concentrations (c) 0.25 μg $mL^{-1}$ and (d) 10 μg $mL^{-1}$. Larger concentrations show more pinning/depinning of the contact lines. In this figure, the substrate lift rate is held constant across experiments at 7 mm $min^{-1}$.

**Figure 2.5.** Dose FESA is a scalable process for creating aligned arrays of nanotubes. (a-c) Dose FESA substrate of aligned nanotubes on a centimeter, millimeter, and nanometer scale, respectively. (a) and (b) are optical photographs. In (a), the aligned nanotube bands appear purple. In (b) the aligned bands are dark. (c) shows an SEM micrograph of dense, well-aligned nanotubes at the top of a band.

**Figure 3.1.** Experimental apparatus for studying interfacial assembly in TaFISA and effect of flow on alignment. (a) Polymer wrapped arc-discharge carbon nanotube used in this work. (b) Experimental apparatus for TaFISA. (c) Magnified view of ink/water interface and alignment process shown in (b). (d,e) SEM of TaFISA films obtained without flow and with flow. The inset in (e) is a histogram (manually extracted) of orientation angle, weighted by nanotube length. The horizontal-axis varies from –90 to 90°. (f) SEM from FESA film. The scalebar in (f) is 250 nm and applies to (d-f). (g-i) Raman spectroscopy maps of relative carbon nanotube density from each respective film in (d-f). Color scalebar at right of panel (i) is linear and applies to (g-i). The scalebar in (i) is 250 μm and applies to (g-i). Histograms of relative nanotube density from the Raman maps are included as insets in each panel.

**Figure 3.2.** Quantifying effect of flow rate on ordering in TaFISA films. (a-c) SEM images from TaFISA films fabricated with volumetric flow rates of 0, 1, and 4 mL $min^{-1}$, respectively, overlaid with local director orientations obtained from two-dimensional fast Fourier transform analysis. The scalebars in (a-c) are 1 μm, and images without overlays are shown in **Fig. B5**. (d-f) Director orientation distributions at flow rates of 0, 1, and 4 mL $min^{-1}$. The dashed line in (f) is the Gaussian fit of the local orientation histogram from **Fig. 3.1i**. (g-i) POM images from TaFISA films fabricated with volumetric flow rates of 0, 1, and 4 mL $min^{-1}$, respectively. Scalebar in (i) is 250 μm and applies to (g-i). SEM image inset in (h) shows -1/2 (blue) and +1/2 (red) liquid crystal defects in TaFISA films. Scalebar in inset is 2 μm.

**Figure 3.3.** Effect of concentration on TaFISA films. (a-d) SEM images of TaFISA films fabricated using nanotube ink concentrations of 0.1, 1, 5, 25, and 100 μg $mL^{-1}$, respectively. The scalebar in (e) is 500 nm and applies to (a-e). (f) Carbon nanotube packing density as a function of ink concentration.

**Figure 3.4.** Effect of temperature on TaFISA films. (a-c) POM images from TaFISA films deposited at 35, 23, and 10 °C, respectively. The scalebar in (c) is 200 μm and applies to (a-c). In (c), faint horizontal lines are observed spaced with a regular period of 29.6 μm. The substrate motor lift-rate of 2666.7 μm $s^{-1}$ divided by the line period corresponds to a frequency of 90 Hz, matching a frequency of 90 Hz inherent to the substrate lift motor control; therefore, these faint lines are artifacts. Histograms of POM image pixel intensity are shown in the insets to (a-c). (d) SEM image from the sample in (c). The scalebar in (d) is 500 nm.

of perfluoroalkoxy (PFA) is situated on the substrate to define the area for the ink to flow. The top plate has a tubing inlet to allow ink and solvent to flow across the substrate. Four bolts (M6 × 0.75) with 1.7 N-m of torque are used directly around the substrate to attach the top plate to the bottom plate and seal the channel. The remaining three bolts are hand-tightened. After tightening, the PFA mask compresses until the top plate hits the stainless steel spacers outside the channel mask.

**Figure 5.2.** Effect of shear rate on nanotube alignment. (a) Half-width at half-maximum (HWHM) of alignment within a confined shear aligned nanotube film measured via polarized Raman spectroscopy as a function of shear rate plotted on a linear-log scale. Alignment increases with increasing shear rate, following a power-law with an exponent of -0.10, regardless of the method used to adjust shear (blue squares—volumetric flow rate is varied, orange circles—channel height is varied). The inset is the same data plotted on a linear-linear scale. (b) The percent mass abundance of nanotubes with a given rotational diffusion coefficient as calculated from the nanotube length distribution fit from Brady et al.[3] The red dashed line at 386 $s^{-1}$ in both graphs in (a) and in (b) is the rotational diffusion coefficient with the greatest percent abundance in our nanotube inks. (c-d) SEM micrographs of nanotubes deposited on 90 nm of $SiO_2$ on Si using a shear rate of 19 and 9600 $s^{-1}$, respectively, from the volumetric flow rate series. The fluid flow direction is top to bottom of the page. Scale bar is 500 nm.

**Figure 5.3.** Effect of nanotube ink concentration and ink volume on packing density. (a) Plot of packing density versus ink concentration (at constant ink volume of 250 µL). (b-e) SEM images of four films from part (a) prepared at ink concentrations of 2.8, 42, 140, and 280 µg $mL^{-1}$, respectively, with resulting packing densities of 0.7, 14, 31, and 36 $\mu m^{-1}$, respectively. Scale bar is 500 nm. The fluid flow direction is from top to bottom of the page. In part (a), the packing density increases steeply with increasing ink concentration until a density of ~30 $\mu m^{-1}$ is reached, and then increases more slowly. Our hypothesis is that the packing density begins to saturate at 30 $\mu m^{-1}$ because at this density, newly deposited nanotubes must adhere to the substrate by sticking to previously deposited nanotubes as opposed to sticking to the bare substrate. (f) Plot of packing density as a function of nanotube ink volume (at constant ink concentration of 14 µg $mL^{-1}$). For these data, the channel height is 120 µm, the volumetric flow rate is 100 mL $min^{-1}$, and the channel width is 9.4 mm.

**Figure 5.4.** FETs fabricated from confined shear aligned nanotube films. (a-b) SEM micrographs of FETs in which the direction of nanotube alignment is oriented parallel (a) and perpendicular (b) to the channel that is defined by the source and drain electrodes. Scale bar is 500 nm. (c) Representative $I_{DS}$ versus $V_{GS}$ curves measured at $V_{DS}$ of -1 V of the parallel (green) and perpendicular (purple) nanotube FETs with $L_{ch}$ = 1 µm and packing density of 59 $\mu m^{-1}$. (d) Extracted hole mobility of parallel (green) and perpendicular (purple) nanotube FETs as a function of $L_{ch}$ using a packing density of 59 $\mu m^{-1}$. (e) Extracted hole mobility of parallel FETs as a function of $L_{ch}$ using a packing density of 15 (orange stars), 29 (blue hexagons), and 59 (green triangles) $\mu m^{-1}$. (f) Average hole mobility of parallel FETs with $L_{ch}$ = 2 – 5 µm as a function of nanotube packing density. For this data, the PFA mask and channel height are 127 µm and 120 µm, respectively. The ink volume is 250 µL. The volumetric flow rate is 100 mL $min^{-1}$. The width of nanotube deposition for each film is 10.5 mm. The mobility plotted in parts d-f is calculated using the array capacitance (see main text).

**Figure 5.5.** Confined shear aligned nanotube film deposited across an 8 × 8 $cm^2$ area on 90 nm of $SiO_2$ on Si. (a) Raman spectroscopy map of the nanotube packing density overlaid on an optical image of the sample. The white dashed line indicates the approximate edges of the mask used to define the deposition channel. (b) SEM micrograph of the aligned nanotubes (light contrast) within the confined shear aligned film shown in (a). Scale bar is 1 µm.

# **Chapter 1.** Introduction

**1.1 Atomic structure and electronic properties of semiconducting single-walled carbon nanotubes.** The physical structure of single-walled carbon nanotubes can be visualized by rolling a sheet of graphene (i.e., $sp^2$ hybridized carbon atoms in a honeycomb lattice) into a one-dimensional cylinder. The rolling process, shown in **Fig. 1.1a**, is defined by two indices (n, m) that are the number of discrete increments moved across the honeycomb lattice vector directions $\boldsymbol{a_1}$ and $\boldsymbol{a_2}$ as defined in **Fig. 1.1a**. These indices and lattice vectors define the chiral vector $\boldsymbol{C_h} = n\boldsymbol{a_1} + m\boldsymbol{a_2}$ and the diameter $d_{CNT} = |\boldsymbol{C_h}|/\pi$ of the nanotube.[1] The chiral vector indicated in **Fig. 1.1a** corresponds to a (4,2) nanotube—structure shown in **Fig. 1.1b**. Depending on the way the sheet is rolled, there are three different types of carbon nanotubes that can be formed: armchair (n = m), zigzag (m = 0), or chiral (all other cases). Importantly, these chiral indices dictate the electronic structure of carbon nanotubes. In the case where the chiral indices satisfy n - m = 3j (where j is an integer), allowed K-space lines will intersect the K-points within the Brillouin zone, resulting in a near zero bandgap, or metallic in electrical behavior. If the chiral indices $n-m \neq 3j$, then the K-space lines will not intersect the K-points and the carbon nanotube will be semiconducting. This is shown in **Fig. 1.1c** for a (4,2) nanotube. From this definition, during typical production of carbon nanotubes, two-thirds of carbon nanotubes will be semiconducting and one-third will be metallic. Tight-binding calculations have been used to estimate a diameter dependent bandgap ($E_g$) of semiconducting carbon nanotubes $E_g = \gamma\ (2R_{c\text{-}c}/d_{CNT})$, where $d_{CNT}$ is the nanotube diameter, $R_{c\text{-}c}$ is the C-C bond length, and $\gamma$ is the hopping matrix element (~3 eV).[4] This tunable bandgap property of carbon nanotubes makes carbon nanotubes attractive candidates for many electronic devices, from solar energy, where larger bandgaps corresponding to optical wavelengths are required, to transistors, where smaller bandgaps are needed.

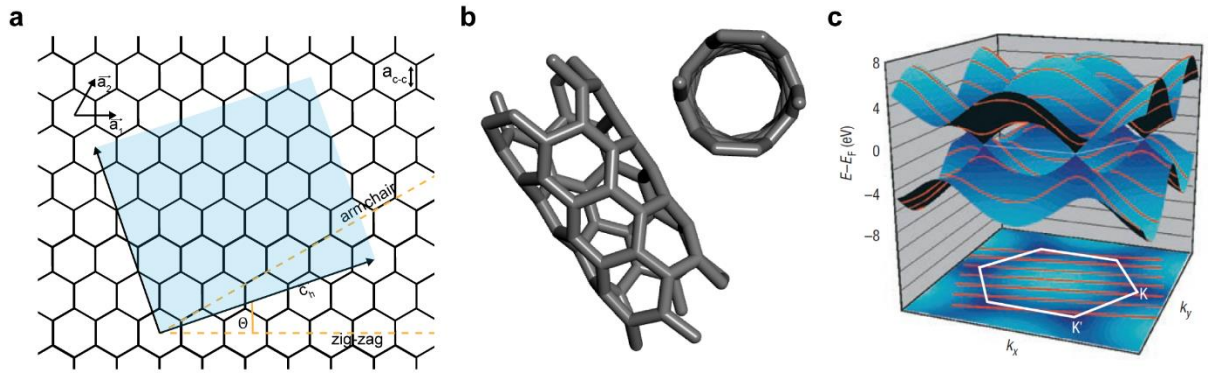


**Figure 1.1.** Physical and electronic structure of semiconducting single-walled carbon nanotubes. (a) Schematic of two-dimensional graphene lattice and corresponding lattice vectors and chiral indices that define the physical structure of a nanotube. Specifically, a (4,2) carbon nanotube is depicted here. (b) Visualization of the unit cell of a (4,2) carbon nanotube shown from the side and down the length of the nanotube. (c) Band structure (top) and Brillouin zone (bottom) of graphene. The red parallel lines are the discrete energy subbands for a nanotube overlaid on the graphene Brillouin zone. If the lines pass through the K-points, then the nanotube is metallic, otherwise, the nanotube is semiconducting. **Fig. 1.1c** is reproduced from Ref. [1]. Copyright (2007) Nature Publishing Group.

Indeed, one of the most exciting applications of semiconducting carbon nanotubes is their integration as the active semiconducting channel in field-effect transistors (FETs). Measurements based on individual semiconducting carbon nanotubes have shown that nanotubes exhibit high carrier velocity,[5,6] high current carrying capacity,[7] and exceptional electrostatic control due to their thin, one-dimensional bodies.[1] Ballistic conduction at room-temperature was first realized in FETs based on single semiconducting carbon nanotubes more than a decade ago[8,9] and additionally FETs with a sub-10 nm channel length based on single carbon nanotubes have demonstrated 3× higher current density than Si metal-oxide-semiconductor FETs (MOSFETs).[7] Because of their nanometer-sized dimensions, carbon nanotubes can also enable continued down-scaling of FETs for logic applications as silicon approaches its limits. The excellent mechanical properties of carbon nanotubes also enable applications such as flexible[10,11] and stretchable electronics.[12] These unique and exceptional charge transport properties have motivated an enormous research effort toward understanding the physical properties and potential applications of semiconducting carbon nanotubes.

**1.2 Exceptional electronic properties of aligned carbon nanotube films.** In order to implement semiconducting carbon nanotubes into future electronic devices, FETs must contain multiple carbon nanotubes to achieve high on-current. Extensive work has been performed toward integrating random networks of carbon nanotubes into FETs,[11,13–15] however, high-performance FETs must comprise aligned carbon nanotubes. Alignment of carbon nanotubes is vital to reduce resistive nanotube-nanotube crossings within the film morphology to enable high transistor drive current and mobility.[16,17] Modeling has shown that carbon nanotube FETs need to consist of parallel, aligned arrays of densely-packed semiconducting carbon nanotubes spaced at an ideal packing density of ~100 nanotubes $\mu m^{-1}$ to achieve optimum performance.[2,18] An ideal carbon nanotube back gate FET structure is shown in **Fig. 1.2a**. Top source and drain electrodes are deposited on an aligned carbon nanotube array with ideal packing densities between 100-200 $\mu m^{-1}$. The conductance through the nanotube channel is modulated through the gate dielectric and underlying gate electrode that the nanotubes are deposited on top of (shown in blue in **Fig. 1.2a**).

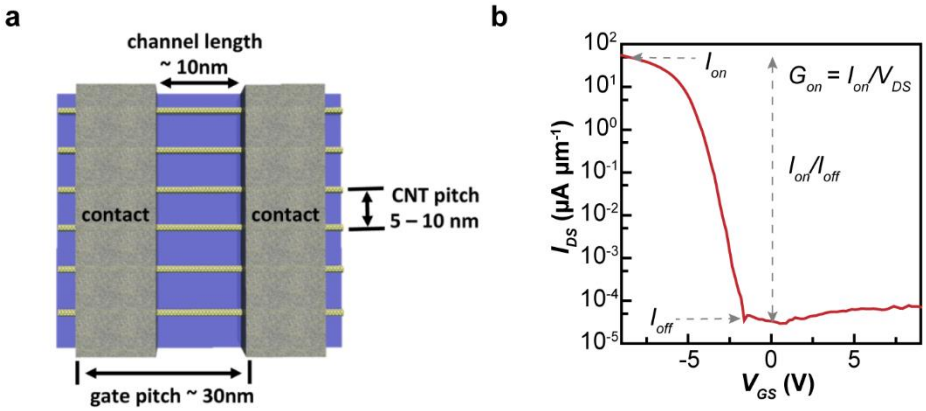


**Figure 1.2.** Carbon nanotube FET architecture and device characteristics. (a) Schematic of carbon nanotube FET with ideal nanotube spacing. Reprinted (adapted) with permission from Ref. [2]. Copyright (2014) American Chemical Society. (b) Carbon nanotube FET performance—characteristic source-drain current per channel width ($I_{DS}$) versus gate-source voltage ($V_{GS}$). Nanotube device metrics: $I_{on}$, $I_{off}$, $I_{on}/I_{off}$, and $G_{on}$ are indicated.

To evaluate carbon nanotube FET performance, two metrics are typically used: the on/off conductance ratio ($I_{on}/I_{off}$), which should be high to reduce current leakage, and the on-state conductance per width ($G_{on}$) which should also be high to enable faster switching (both indicated in **Fig. 1.2b**). The theoretical limit of $G_{on}$ per nanotube is $2G_0 = 4e^2/h = 155$ μS, which is the quantum conductance limit.[19]

Therefore, if nanotubes are packed at an ideal density of ~100 nanotubes $\mu m^{-1}$ and each nanotube exhibits the theoretically maximum conductance of 155 µS, the expected optimum performance of an ideal carbon nanotube FET would be 15.5 mS $\mu m^{-1}$.

FETs based on aligned carbon nanotubes exhibit a wide range of performance, depending on processing, packing density, and semiconducting purity. For example, semiconducting aligned arrays of nanotubes fabricated via chemical vapor deposition (CVD) and subsequently purified via Joule heating have exhibited a conductance of 0.12 mS $\mu m^{-1}$ (1.2 µS per nanotube).[20] Arrays of aligned semiconducting carbon nanotubes have been deposited onto substrates from solution (after sorting with anionic surfactants) via Langmuir-Schaefer assembly at a high density of 1100 $\mu m^{-1}$, exhibiting a conductance of 0.25 mS $\mu m^{-1}$ (0.23 µS per nanotube).[21] Carbon nanotubes aligned via floating evaporative self-assembly (FESA) initially demonstrated FETs with $G_{on}$ = 34 – 197 µS $\mu m^{-1}$ (0.94 – 5.7 µS per nanotube) for $L_{ch}$ ranging from 3 µm down to 160 nm, respectively.[3] These devices had on/off ratios ranging from $10^5$ – $10^6$. Further optimization of FESA aligned films demonstrated the fabrication of aligned carbon nanotube FETs with device conductance as high as 1.7 mS $\mu m^{-1}$ (35 µS per nanotube) and outperforming Si and GaAs devices in current density.[22]

These charge transport results demonstrate that FETs based on aligned carbon nanotubes are extremely exciting. However, there are a lack of scalable processes to align semiconducting carbon nanotubes in an ideal film morphology: singly dispersed, highly pure semiconducting carbon nanotubes, uniformly aligned over large areas. Once these challenges can be overcome, carbon nanotubes promise to be an ideal candidate for next-generation FETs.

**1.3 Overview of carbon nanotube material and organizational challenges.** The alignment of carbon nanotubes has been difficult, by itself, but concurrently demonstrating control over semiconducting purity, packing density, nanotube individualization, uniformity, and large-area scaling, which would allow this material to be integrated into industrial electronics has been especially challenging. Several approaches have been researched for fabricating arrays or films of semiconducting carbon nanotubes with improved

alignment. These approaches are generally broken into two categories: the direct growth of aligned arrays via chemical vapor deposition (CVD) and alignment of carbon nanotubes from solution.

While historically, CVD growth of aligned nanotubes have resulted in low semiconducting purities,[23,24] improved purities (~95%) can be achieved through the use of specifically chosen catalysts,[25,26] but these films in general suffer from low packing density and multiple transfers must be used to achieve higher packing densities. These purities are still not as high as that achievable via post-synthesis sorting in solution, and additionally, CVD growth requires high-temperatures which limits the surfaces on which carbon nanotubes can be grown.

Solution processing is often preferable to direct growth as metallic nanotubes can be removed prior to deposition using conjugated polymer wrappers[27] or similar methods[28] to produce inks of highly purified semiconducting carbon nanotubes. Alignment of solution processed nanotubes can also be performed at room temperature on arbitrary surfaces, enabling the direct deposition of semiconducting carbon nanotubes onto target substrates. Different polymer wrappers have been investigated for isolation of semiconducting carbon nanotubes, including polyfluorene,[27] polythiophene,[29] and polycarbazole[30,31] derivatives. The structure of these polymer wrappers can have dramatic differences in terms of resulting semiconducting purity and nanotube chirality selection.[32,33] A schematic of the general polymer wrapping and semiconducting sorting procedure is shown in **Fig. 1.3**.

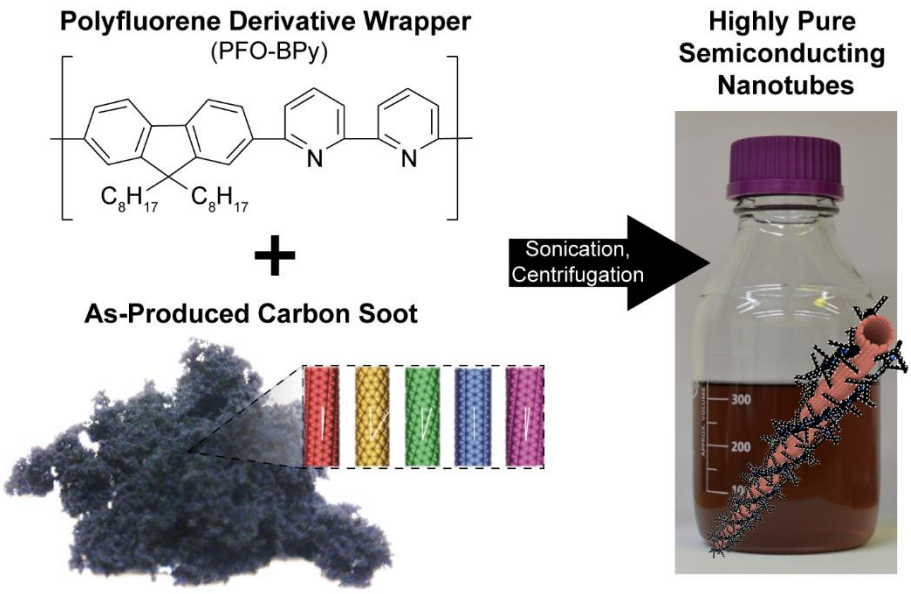


**Figure 1.3.** Isolation of semiconducting carbon nanotubes using PFO-BPy. Poly[(9,9-dioctylfluorenyl-2,7-diyl)-alt-co-(6,6′-{2,2′-bipyridine})] (PFO-BPy) is combined with as-produced nanotube soot in solution. The as-produced soot is comprised of metallic and semiconducting nanotubes of different chiralities (shown in different colors) as well as amorphous carbon and other undesirable carbon allotropes. Through a series of sonication and centrifugation steps, highly-pure PFO-BPy wrapped semiconducting carbon nanotubes are isolated. Nanotube schematic of different chiralities courtesy of Michael Arnold.

Many processes for the alignment of nanotubes from solution have been pursued, however, many of these approaches have been developed without transistors in mind. For example, the alignment of multiwalled carbon nanotubes has been demonstrated extensively; yet, multiwalled carbon nanotubes are semimetallic and thus are not suitable for transistors.[34,35] Additionally, techniques for aligning multiwalled carbon nanotubes are generally difficult to translate to aligning single-walled carbon nanotubes, which are considerably smaller than multiwalled carbon nanotubes. Similarly, recent work has shown that films of aligned nanotubes can be obtained via vacuum filtration under specific conditions.[36] However, these films consist of many stacked layers of carbon nanotubes. Moreover, alignment of nanotubes via liquid crystal phenomena has typically yielded multilayers.[37,38]

Toward the more specialized goal of assembling semiconducting carbon nanotubes specifically for thin film electronics there have been many techniques pursued. Some of these techniques include Langmuir-Blodgett,[39] and Langmuir-Schaefer[40] methods, blown-bubble assembly,[41] elastomeric release,[42] directed

evaporation,[43–45] floating evaporative self-assembly (FESA),[3,22,46] dimension-limited self-assembly (DLSA), and DNA directed alignment,[47] among others. Many of these approaches have demonstrated immense progress, for example, producing nanotube transistors with high conductance,[22] high mobility,[3] or transistors with aggressively downscaled channel lengths.[48,49] While these methods are promising, more work is needed to improve these techniques or develop new alignment methods that are scalable and achieve uniform alignment, individualization, and control over nanotube packing density.

**1.4 Scope of thesis.**

This work primarily focuses on development of solution-based processes to uniformly align individualized semiconducting carbon nanotubes with controlled packing density across the wafer-scale for next-generation semiconductor technologies.

In Chapter 2 and Appendix A, we elucidate the mechanism of the FESA process. In this technique, a substrate is lifted vertically out of a water subphase while nanotube ink is sequentially dosed or dropped at the air/water/substrate contact line. The ink droplets spread rapidly on the water subphase, with each droplet resulting in the deposition of a band of aligned nanotubes. In this chapter, we track the ink/air and ink/water interfaces during the FESA process and correlate deposition of aligned stripes of nanotubes with the interface motion. Consequently, we determine that the nanotube alignment occurs from the ink/water interface, as opposed to the ink/air interface as previously hypothesized. We also establish improved control over the FESA film morphology and demonstrate nanotube alignment over a $2.5 \times 2.5$ cm$^2$ substrate.

In Chapters 3 and 4 and Appendices B and C, we develop a novel technique, tangential flow interfacial self-assembly (TaFISA), to fabricate continuous, uniform films of highly aligned nanotubes from 2D nematic liquid crystal assemblies. In Chapter 3, we demonstrate that nanotubes trapped at a two-dimensional liquid/liquid interface self-organize due to liquid crystal phenomena, and the addition of flow induces global alignment of these assemblies. Because of the lyotropic liquid crystal phenomena governing the alignment, the order improves with increasing concentration and decreasing temperature and continuous

films of highly aligned nanotube arrays (within ±5.7°) are fabricated across 10 cm wide substrates. The high array uniformity translates to excellent FET characteristics and reproducibility, with high on-state current density averaging 520 μA $\mu m^{-1}$ at –0.6 V and FET to FET variation of only 19%. In Chapter 4, we extensively explore several additional parameters that affect the interfacial assembly, including the nanotube ink composition, the chemical functionalization and water contact angle of the substrate surface, and the water subphase composition.

In Chapter 5 and Appendix D, we use large amounts of shear to align carbon nanotubes directly from bulk solution, without the use of the ink/water interface as in the alignment techniques studied in Chapters 2, 3, and 4. In this work, nanotubes in organic ink are forced through a channel with sub-mm height, generating shear up to 10,000 $s^{-1}$ and aligning nanotubes across 10 × 10 $cm^2$ substrates. Without the use of the ink/water interface, the nanotubes are more misaligned. For example, the spread in nanotube alignment, or half-width at half-maximum (HWHM), decreases from 58 to 31° when the shear rate is increased from 19 to 9,600 $s^{-1}$, which is less aligned than the HWHMs of 11.5 and 5.7° reported by FESA and TaFISA processes in Chapters 2 and 3, respectively. However, these quasi-aligned nanotube films are ideally suited for long-channel nanotube FETs, in which the channel length exceeds the average length of the nanotubes and some degree of misalignment is required to ensure efficient charge percolation across the channel.

In Chapter 6 and Appendix E, we demonstrate that the same confined, shear-based alignment technique used in Chapter 5 can also be used to deposit ultrathin films of aligned cellulose nanocrystals (CNCs) from solution. We demonstrate improved control over film thickness and degree of alignment, which is promising for application of CNC films in coatings with high mechanical strength or piezoelectricity. Importantly, these results also prove that confined, shear-based alignment is a promising technique to align quasi-one-dimensional materials beyond carbon nanotubes.

# **Chapter 2.** Nanotube alignment mechanism in floating evaporative self-assembly

Chapter 2 was adapted with permission from Jinkins, K. R., Chan, J., Brady, G. J., Gronski, K. K., Gopalan, P., Evensen, H. T., Berson, A., & Arnold, M. S. Nanotube Alignment Mechanism in Floating Evaporative Self-Assembly. *Langmuir* **33**, 13407-13414 (2017).  K.R.J. fabricated the samples and performed the experiments and data processing for the Dose FESA experiments. J.C. and A.B. developed the MATLAB analysis code for tracking the contact lines. G.J.B., K.K.G., and H.T.E. performed the preliminary back-imaging experiments. G.J.B. and H.T.E. performed the stationary FESA (**Fig. 2.1**) and the deposition from a thick, stagnant layer of nanotube ink experiments (**Fig. A9**). M.S.A. and A.B. supervised the work. All authors contributed to data interpretation. K.R.J. drafted the manuscript, and all authors discussed and revised it.

**Abstract**: The challenge of assembling semiconducting single-wall carbon nanotubes into densely packed, aligned arrays has limited the scalability and practicality of high-performance nanotube-based electronics technologies. The aligned deposition of nanotubes via Floating Evaporative Self-Assembly (FESA) has promise for overcoming this challenge; however, the mechanisms behind FESA need to be elucidated before the technique can be improved and scaled. Here, we gain a deeper understanding of the FESA process by studying a stationary analog of FESA and optically tracking the dynamics of the organic ink/water/substrate and ink/air/substrate interfaces during the typical FESA process. We observe that the ink/water interface serves to collect and confine the nanotubes before alignment and that the deposition of aligned bands of nanotubes occurs at the ink/water/substrate contact line during a depinning of both the ink/air/substrate and ink/water/substrate contact lines. We also demonstrate improved control over the interband spacing, bandwidth, and packing density of FESA-aligned nanotube arrays. The substrate lift rate (5 – 15 mm $min^{-1}$) is used to tailor the interband spacing from 90 to 280 μm while maintaining a constant aligned nanotube bandwidth of 50 μm. Varying the nanotube ink concentration (0.75 – 10 μg $mL^{-1}$) allows

control of the bandwidth from 2.5 to 45 μm. A steep increase in packing density is observed from 11 $\mu m^{-1}$ at 0.75 μg $mL^{-1}$ to 20 $\mu m^{-1}$ at 2 μg $mL^{-1}$, with a saturated packing density of ~24 $\mu m^{-1}$. We also demonstrate scaling of FESA to align nanotubes on a 2.5 × 2.5 $cm^2$ scale while preserving high quality alignment on the nanometer scale. These findings promise to help realize the scalable fabrication of well-aligned nanotube arrays to serve as large-area platforms for next-generation semiconductor electronics.

**2.1 Introduction.**

Studies of individual semiconducting single-wall carbon nanotubes have shown that nanotubes exhibit exceptional electronic properties including high charge carrier mobility and current carrying capacity, making them attractive candidates for next-generation field effect transistors (FETs) for thin film, radio frequency, and semiconductor electronics technologies.[8,48,50,51] These FETs will need to be fabricated from aligned arrays of multiple nanotubes in order to maximize their performance – as opposed to single nanotubes or networks of randomly oriented nanotubes. However, the scalable assembly of nanotubes into densely packed, aligned arrays has been challenging.[52] One method that has generated a lot of promise is floating evaporative self-assembly (FESA). FESA yields highly aligned nanotube stripes at intermediate packing densities (50 $\mu m^{-1}$). The excellent alignment and array uniformity in FESA films has led to excellent FET performance, including outperforming gallium arsenide (GaAs) and silicon (Si) FETs with respect to on-state current density and conductance.[22] However, previously, the mechanism of this technique was unknown, making it difficult to envision routes to further improve the technique and resulting aligned nanotube arrays.

In FESA, a vertical substrate is lifted out of a water trough while nanotubes in organic solvent (nanotube ink) is sequentially dosed in μL droplets at the air/water/substrate contact line.[46] The ink droplets spread rapidly on the water surface with each droplet resulting in the deposition of a band of aligned nanotubes across the substrate.

FESA was initially termed “Floating Evaporative Self-Assembly” because it was believed the mechanism of FESA was similar to that of conventional evaporative self-assembly. However, as the results discussed in this chapter illustrate, the mechanisms controlling the deposition and alignment of nanotubes in each process are distinct. In evaporative self-assembly, a single solvent evaporates, with the substrate being translated out of the solvent in some variants of the method. The evaporation induces the convective transport of nanostructures to the substrate-solvent-air contact line, resulting in the deposition of dense ‘coffee rings’ of ordered nanostructures such as nanotubes.[53,54] However, unlike evaporative self-assembly, FESA utilizes two liquid phases (the organic solvent and the water subphase), and, practically, the time scale of FESA is much shorter than evaporative self-assembly (seconds and minutes compared to hours or even days). Moreover, even though there is evaporation of the organic solvent in FESA, it does not contribute to the alignment of the nanotubes (as shown below), and the small fraction of the organic solvent that does evaporate is rapidly replenished via subsequent dosing of the ink.

More similar to FESA in method than evaporative self-assembly, the Langmuir-Blodgett and -Schaefer approaches for aligning nanostructures both employ two liquid phases. In the Langmuir-Blodgett and -Schaefer methods, a nanostructure-containing organic ink is spread on a water trough. After the solvent completely evaporates, barriers are used to closely pack nanostructures, such as nanotubes, into well-ordered arrays.[21,39] However, there are three key differences between FESA and the Langmuir-Blodgett and -Schaefer methods: (i) during FESA, the organic solvent is never allowed to completely evaporate; (ii) during FESA, the organic solvent is still spreading as the nanostructures deposit onto the substrate; and (iii) barriers are not needed during FESA to induce alignment in the films (as used in the Langmuir-Blodgett and -Schaefer methods).

An additional approach for assembling nanostructures is to use a two-phase system, comprised of two immiscible liquids, in which neither liquid evaporates and nanostructures that assemble at the liquid/liquid interface are transferred to substrates. Unlike Langmuir-Blodgett and –Schaefer methods, this approach does not require a barrier. Two-phase assembly has been employed previously to obtain aligned

assemblies of nanowires and nanorods[55,56] and randomly aligned films of nanotubes and graphene.[57,58] Such studies suggest that the segregation of nanotubes at the liquid/liquid interface may also be important during FESA; although one important difference between FESA and these previous two-phase assembly methods is that FESA is a dynamic process during which the organic ink layer spreads and flows.

These significant distinctions between the FESA technique and other similar nanostructure alignment strategies motivate an in-depth study into the mechanisms underpinning FESA. A complete understanding of the FESA approach promises to guide future research in the control and manipulation of aligned arrays of nanotubes. In this chapter, we gain detailed insight into FESA by both studying a stationary analog of FESA (termed Stationary FESA) and optically tracking the ink/air/substrate and ink/water/substrate contact lines during the typical FESA process (termed Dose FESA) and then correlating the positions of these interfaces with the positions of the deposited nanotubes. We learn that, first, the ink/water interface serves to collect and confine nanotubes during FESA. Second, nanotubes deposit onto the substrate from the ink/water interface during the depinning of the ink/water/substrate and ink/air/substrate interfaces. The depinning of the interfaces and the outward spreading of ink likely aid in the alignment of the already-confined nanotubes as they deposit onto the substrate. We also show that the substrate lift rate can be used to dictate the spacing between the bands of aligned nanotubes and that the ink concentration controls both bandwidth and packing density. Finally, we demonstrate the scaling of FESA to a 2.5 × 2.5 $cm^2$ deposition area.

## 2.2 Results and discussion.

**2.2.1 Stationary FESA.** We first study a simplified table-top version of the FESA method, Stationary FESA. A water trough is not used; instead, a small 15 µL water droplet is placed on a stationary, horizontal substrate. A single 10 µL dose of ink is deposited on top of the water droplet, yielding a single aligned band of nanotubes at the ink/water/substrate contact line. Stationary FESA provides a simple way to measure the

position of ink/water contact line on the substrate and compare it with the position of the resulting deposited nanotubes.

When the nanotube ink is delivered during Stationary FESA, the ink spreads quickly around the water droplet, creates a 'skirt' at the base of the droplet (**Fig. 2.1a**), and then evaporates. The air/water/substrate contact line moves inwards during this process yielding a more hydrophobic contact angle (**Fig. 2.1b**). After the solvent has evaporated, the water droplet is manually removed using a syringe and scanning electron microscopy (SEM) (Zeiss Leo 1530) is used to characterize the nanotubes deposited on the substrate. The nanotubes that deposit at the ink/air/substrate contact line are randomly oriented (**Fig. 2.1c**). Dense stripes of randomly oriented nanotubes are observed and are attributed to a 'coffee-stain' effect caused by the dynamical pinning and zipping motion of the ink/air/substrate interface as the solvent evaporates.[53] In constrast, the nanotubes that deposit at the ink/water/substrate contact line are well aligned, similar to the alignment previously demonstrated by Dose FESA[22,46] (**Fig. 2.1d**). The aligned nanotubes that deposit at the edge of the water droplet are responsible for pinning the droplet at the more hydrophobic contact angle previously noted.

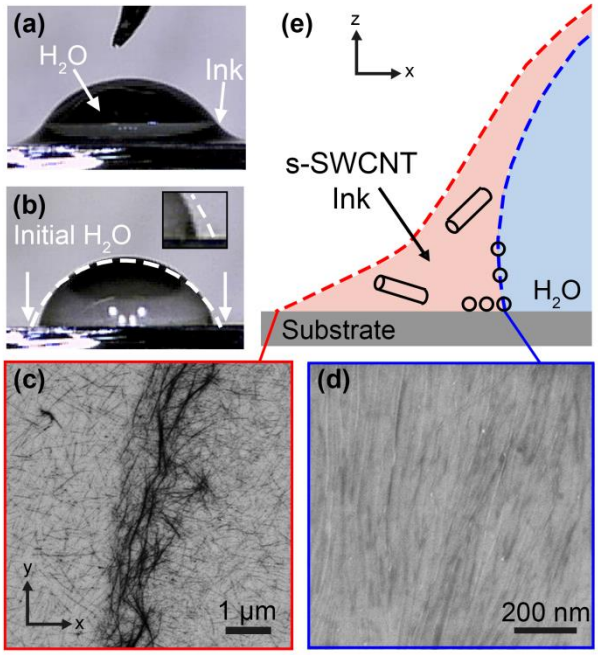

**Figure 2.1**. Stationary FESA experiments elucidate deposition and alignment mechanisms. (a-b) Optical images during and after the Stationary FESA process. (a) A droplet of nanotube ink is applied to a stationary water droplet on a $Si/SiO_2$ substrate. The ink spreads uniformly around the water droplet forming a 'skirt' around the base. (b) The ink evaporates in ~5 s, creating deposits of nanotubes which pin the final water contact line. The initial outline of the water droplet is indicated in white. Inset shows zoomed-in view of the right side of the droplet. (c) SEM micrograph of coffee-stain deposition occurring at the ink/air interface. (d) SEM micrograph of aligned nanotube deposition occurring at ink/water interface. (e) Schematic of the stationary deposition event indicating that aligned nanotube (also noted as s-SWCNT) deposition occurs at the ink/water/substrate contact line. Coordinate systems are shown in (c) and (e) to clarify the orientation of the deposited nanotubes with respect to the droplet geometry. The coordinates in (c) also apply to (d).

The results of these Stationary FESA experiments are surprising and indicate that the aligned deposition of nanotubes occurs at the ink/water/substrate contact line (**Fig. 2.1d**). In contrast, related studies have shown that surfactant encapsulated nanotubes dispersed in aqueous solution align and deposit at the air/water/substrate contact line as the water evaporates. One potential explanation for the deposition of nanotubes at the ink/water/substrate contact line during Stationary FESA is that nanotubes accumulate at this ink/water interface. Related studies have shown that nanostructures, such as graphene nanosheets, collect and assemble at organic solvent/water interfaces.[57] To examine if polyfluorene-wrapped nanotubes would similarly assemble at the chloroform/water interface, we create an emulsion of nanotube chloroform ink in water and let it settle (**Fig. A.1a**). The nanotubes are seen to collect at the chloroform/water interface (**Fig. A.1b**). This observation, in conjunction with results from Stationary FESA experiments, indicates that the collection and confinement of nanotubes at the ink/water interface are important aspects of the FESA process.

**2.2.2 Nanotube assembly using Dose FESA.** The Dose FESA process is more complex than Stationary FESA due to the periodic dosing of ink droplets at the aqueous subphase, the spreading of these droplets, and the translation of the substrate. In order to determine if the collection and confinement of nanotubes at the ink/water interface also plays an important role in Dose FESA, a separate experimental apparatus (**Fig. A2**) is constructed that enables optical imaging of the dynamics of the ink/air/substrate and ink/water/substrate contact lines through a transparent quartz substrate. A 100 fps camera (Basler acA2000-

165uc) is used to record the motion of the contact lines as a series of images. The recorded images are analyzed to track the separate positions of the contact lines.

In these experiments, doses of nanotube-containing organic ink are delivered to an aqueous subphase via a needle that is in direct contact with the surface of the subphase. The contact of the needle tip with the surface provides a more reproducible means for controlling the timing and volume of ink delivery compared with our previous work in which a needle was suspended above the surface releasing drops more sporadically.[46] A syringe pump (Chemyx Nexus 3000) is used to precisely control the volume of each dose of ink and the frequency of the doses. Each dose of ink yields an ordered band of deposited nanotubes that are aligned within a ±10° window, as determined by polarized Raman spectroscopy (see discussion in Appendix A and **Fig. A3**), consistent with our previous FESA studies.[46]

Traces of the contact lines are shown in **Fig. 2.2a** for an experiment in which 1 µL doses of ink are pulsed every 1.2 s. The traces are analyzed in the reference frame of the substrate by subtracting the substrate lift rate (7 mm $min^{-1}$). The traces indicate that immediately after ink is pulsed (denoted by green arrows), both the ink/air/substrate and ink/water/substrate contact lines quickly drop. These events are denoted by the symbols (&) and (%) for ink/air/substrate and ink/water/substrate contact lines, respectively. The distance between the ink/air/substrate and ink/water/substrate contact lines is ~250 µm and is invariant over the course of the experiment. This distance corresponds to the thickness of the chloroform ink layer near the substrate. For comparison, the evaporation rate is only 20.4 µm per 1.2 s (calculation in Appendix A and **Fig. A4**).

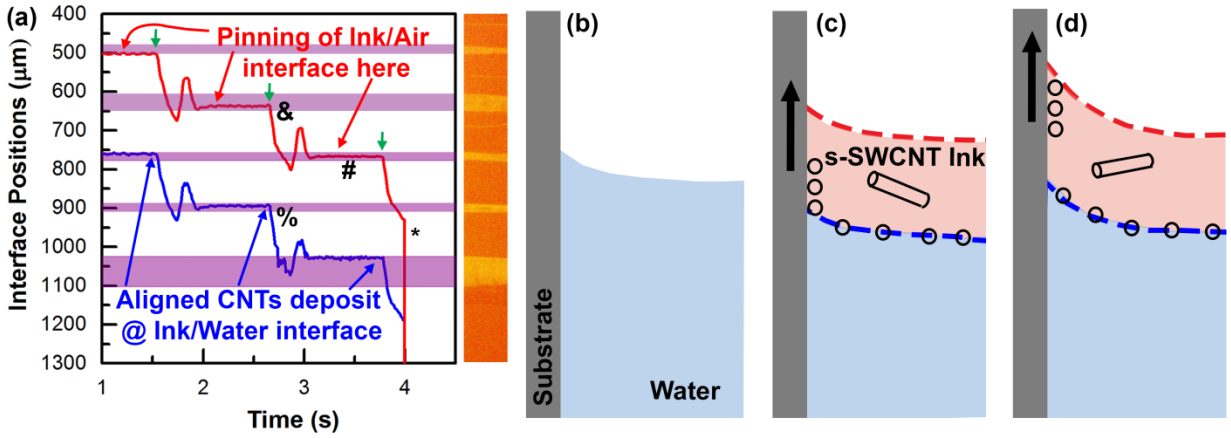


**Figure 2.2.** Dynamics of Dose FESA. (a) Traces of ink/water/substrate and ink/air/substrate contact lines as a function of time, in the frame of reference of the substrate. Cross-polarized optical microscopy image of aligned nanotube bands spatially registered with the traces. The symbols (&) and (%) denote the fall of the ink/air/substrate and ink/water/substrate contact lines, respectively. (#) denotes pinning of the ink/air/substrate contact line and (*) indicates where the substrate is lifted out of the water at a high lift rate to prevent the ink/air/substrate contact line from pinning and drying on the last band deposited. The green arrows indicate when new doses of ink are added. Small oscillations in the positions of the contact lines occur directly after each dose. These oscillations may be indicative of small oscillations in the volumetric flow rate of ink as the ink exits the needle and/or the reflection of surface waves off of the substrate or needle or a combination of the two. Panels (b-d) depict important aspects of FESA. (b) Initially, the substrate is partially submerged in a trough of water. (c) nanotube ink is delivered at the air/water interface. The ink/water interface (dashed blue line) and the ink/air interface (dashed red line) form. A fraction of the nanotubes accumulate at the ink/water interface (dashed blue line) and deposit onto the substrate from this interface. (d) As the substrate is lifted out of the water, the ink/air/substrate contact line is pinned on a previously-deposited band of aligned nanotubes until the next dose of ink is delivered. Variations in band spacing and width are due to insufficient vibration control for this particular experiment.

Using registration marks, we are able to register the positions of the contact lines to the positions of the aligned bands of nanotubes deposited on the substrate (see **Figs. A5, A6, A7** for more details regarding the registration protocol). A registered cross-polarized optical image of aligned nanotubes is shown on the right side of **Fig. 2.2a**. Comparing this image to the traces, it is apparent that the bands of aligned nanotubes deposit onto the substrate shortly after each pulse is delivered, just as the contact lines begin to drop. The dropping of the contact lines and the spreading of the newly delivered ink droplets must both contribute to tangential flows directed parallel to the contact lines. We hypothesize that these flows aid in aligning the nanotubes as they deposit onto the substrate from the ink/water interface. Both of the contact lines fall until the ink/air/substrate contact line is pinned by the previously deposited band of aligned

nanotubes, as denoted in **Fig. 2.2a** by the symbol (#). The pinning of the ink/air/substrate contact line also fixes the ink/water/substrate contact line.

The pinning of the ink/air/substrate contact line on previously deposited bands of aligned nanotubes raises a question. How can we be sure that aligned bands of nanotubes are not formed by the evaporation of ink and the deposition of nanotubes at the ink/air/substrate contact line since this contact line is repeatedly coincident with the aligned bands, as denoted by the symbol (#)? To answer this question, at the end of the experiment tracked in **Fig. 2.2a**, the substrate is rapidly withdrawn from the aqueous subphase at a rate of 50 mm $min^{-1}$, as denoted by symbol (*). This rapid withdrawal prevents the pinning of the ink/air/substrate contact line on the final band of nanotubes. The existence of this final band therefore additionally confirms that each band of aligned nanotubes is deposited not from the ink/air/substrate but rather the ink/water/substrate contact line.

These processes are summarized schematically in **Figs. 2.2b-d**. **Fig. 2.2b** depicts the substrate and water prior to starting the FESA deposition. When the ink is pulsed, nearly simultaneously the nanotubes become confined at the ink/water interface, the ink droplet spreads, and the water level falls near the substrate. The deposition of aligned nanotubes occurs from the ink/water/substrate contact line at the beginning of this fall, potentially aided by tangential flows (**Fig. 2.2c**). As the substrate is raised, the ink/air/substrate contact line becomes pinned by previously deposited nanotubes (**Fig. 2.2d**). Both air and water contact lines are raised along with the substrate until the next pulse of ink arrives and unpins the contact lines.

None of these aspects require the evaporation of the organic solvent from the ink. To confirm that the evaporation of the solvent is not a critical factor during FESA, we next conduct an experiment in which the air is nearly saturated with chloroform vapor to suppress evaporation of the ink as the ink spreads and the nanotubes deposit. Similar nanotube deposition and alignment are observed (**Fig. A8**). Moreover, to further explore if flow and spreading of the organic ink are important parameters during FESA, we conduct an additional experiment without flow (and without evaporation) by layering a relatively thick, uniform, and stagnant layer of nanotube ink on top of the aqueous subphase and withdrawing the substrate through

the solvent/water interface. The nanotubes that deposit onto the substrate are randomly aligned in some regions and partially aligned in other regions but without a direction of global alignment (**Fig. A9**). These results further indicate that the accumulation of nanotubes at the solvent/water interface is by itself insufficient to drive the broad alignment of nanotubes without the aid of tangential flows.

In addition to tangential flows, liquid crystal-like interactions and nanotube-nanotube crowding effects may also contribute to the ordering of nanotubes at the liquid/liquid interface. However, the fact that excellent alignment of nanotubes is observed even when the concentration of the ink and the resulting packing density of nanotubes are dramatically decreased (as shown, below, **Fig. 2.4a**) suggest that liquid crystal-like interactions and nanotube-nanotube crowding effects are not the primary factors leading to alignment.

Another factor that likely affects the FESA process is the substrate surface energy. The substrate surface energy will affect the adhesion of nanotubes to the substrate while at the same time dictating the contact angles and consequently the contact-line dynamics that follow each dose of ink. We expect that the necessary contact line dynamics and nanotube adhesion will occur only for a certain range of substrate surface energies; and, therefore, detailed studies of substrate surface energy dependencies should be the focus of future investigations.

The knowledge gained that (i) the collection and confinement of nanotubes at the ink/water interface and (ii) pinning and depinning dynamics are important factors during FESA guide the studies in the next section of this chapter, which analyzes nanotube ink concentration and substrate lift rate dependencies.

**2.2.3 Effect of substrate lift rate and nanotube ink concentration on FESA.** Accurate control over the positioning and bandwidth of FESA-deposited bands of aligned nanotubes and excellent band-to-band uniformity are needed for commercialization efforts. To improve the regularity of the bands and their

uniformity, the FESA apparatus is placed on a vibration isolation table and enclosed inside of an acrylic box to limit air drafts and acoustic vibrations from the laboratory environment. Without these steps, vibrations of the trough surface cause band-to-band variation in both spacing and bandwidth (**Fig. 2.2a**). After implementing these measures, these variations are dramatically reduced thereby improving regularity and uniformity (**Figs. 2.3, 2.4, 2.5, A7, and A10**).

A variable that can be used to control FESA arrays is the substrate lift rate. As shown in **Fig. 2.3a**, the lift rate controls the spacing between bands of aligned nanotubes without affecting bandwidth. SEM micrographs of substrates created using lift rates of 5, 11, and 15 mm $min^{-1}$ are shown in **Fig. 2.3b**, which result in an interband spacing measured at the center of each band of 91 ± 4, 170 ± 7, and 283 ± 7 μm, respectively, and bandwidth of 50 ± 2, 53 ± 3, and 53 ± 3 μm, respectively. The back-imaged contact line dynamics at 5 and 15 mm $min^{-1}$ lift rates (**Fig. A10**) show the same pinning/depinning behavior as seen in **Fig. 2.2a**.

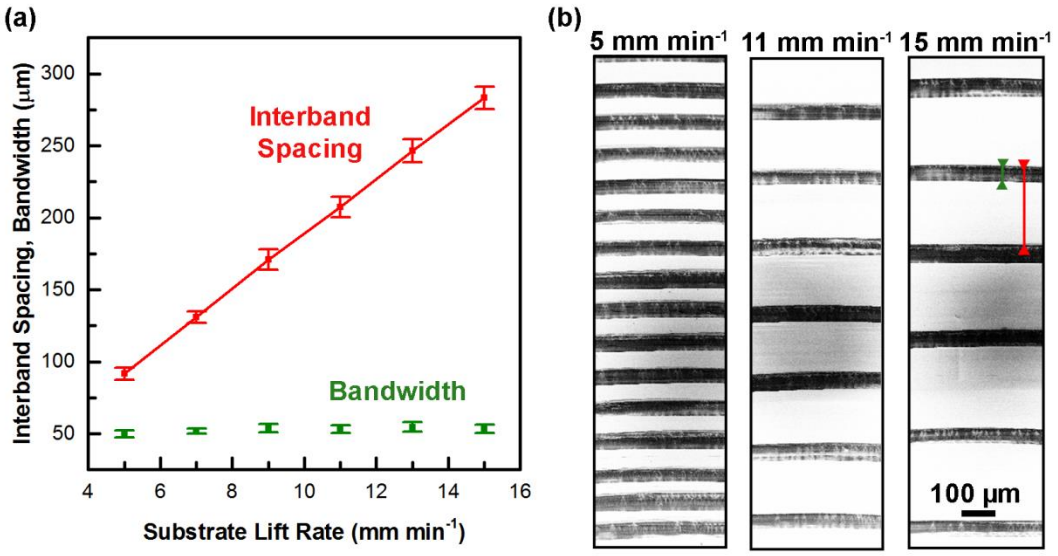


**Figure 2.3**. Dose FESA is a controllable process for nanotube alignment. (a) Interband spacing and bandwidth as a function of substrate lift rate. Bandwidth is invariant while interband spacing increases linearly with lift-rate. (b) SEM micrographs of substrates prepared using lift rates of 5, 11, and 15 mm $min^{-1}$. The aligned bands are black in these micrographs.

The packing density of the FESA aligned nanotube films can be controlled by varying the nanotube ink concentration, at fixed dose volume. We find that an increase in ink concentration from 0.75 to 2 μg $mL^{-1}$ causes an increase in nanotube packing density within each band from 11 to 20 nanotubes $\mu m^{-1}$, as measured by SEM in **Fig. 2.4a**. However, with further increases in ink concentration, we observe a nonlinear relationship between concentration and packing density with the packing density increasing only to ~24 nanotubes $\mu m^{-1}$. SEM micrographs of nanotube films deposited using 0.75 and 7 μg $mL^{-1}$ are compared in **Fig. 2.4b**. It is not clear from SEM or AFM measurements (**Fig. A11**) if some of the nanotubes counted for packing density measurements are fibers of multiple parallel tubes. However, the measured height of the nanotube films does not change in the saturated regime, indicating that the total number of nanotubes deposited in this regime is indeed invariant with nanotube ink concentration. We hypothesize that the initial increase in packing density with increasing ink concentration can be attributed to a concomitant increase in the concentration of nanotubes confined at the ink/water interface. To explain the packing density saturation, our hypothesis is that the concentration of nanotubes at the ink/water interface saturates. Once saturated, further increases in the bulk concentration of the ink do not affect the concentration of nanotubes at the interface, which, in turn, do not affect the packing density of the nanotubes deposited within the bands.

The density of nanotubes that deposit onto the substrate will not only be governed by the density of the nanotubes at the ink/water interface but also by the energetics of their adsorption to the substrate, the spreading of the ink droplet, and the contact line dynamics. These factors will be affected by the surface treatment of substrate, the substrate-needle geometry, and mode of ink delivery. While the surface treatment, the substrate-needle geometry, and ink delivery are all held constant in this study, yielding a saturated packing density of 24 nanotubes $\mu m^{-1}$, other configurations may yield different saturated packing densities. For example, a packing density of 50 nanotubes $\mu m^{-1}$ has been observed when delivering ink via gravity-released droplets.[46]

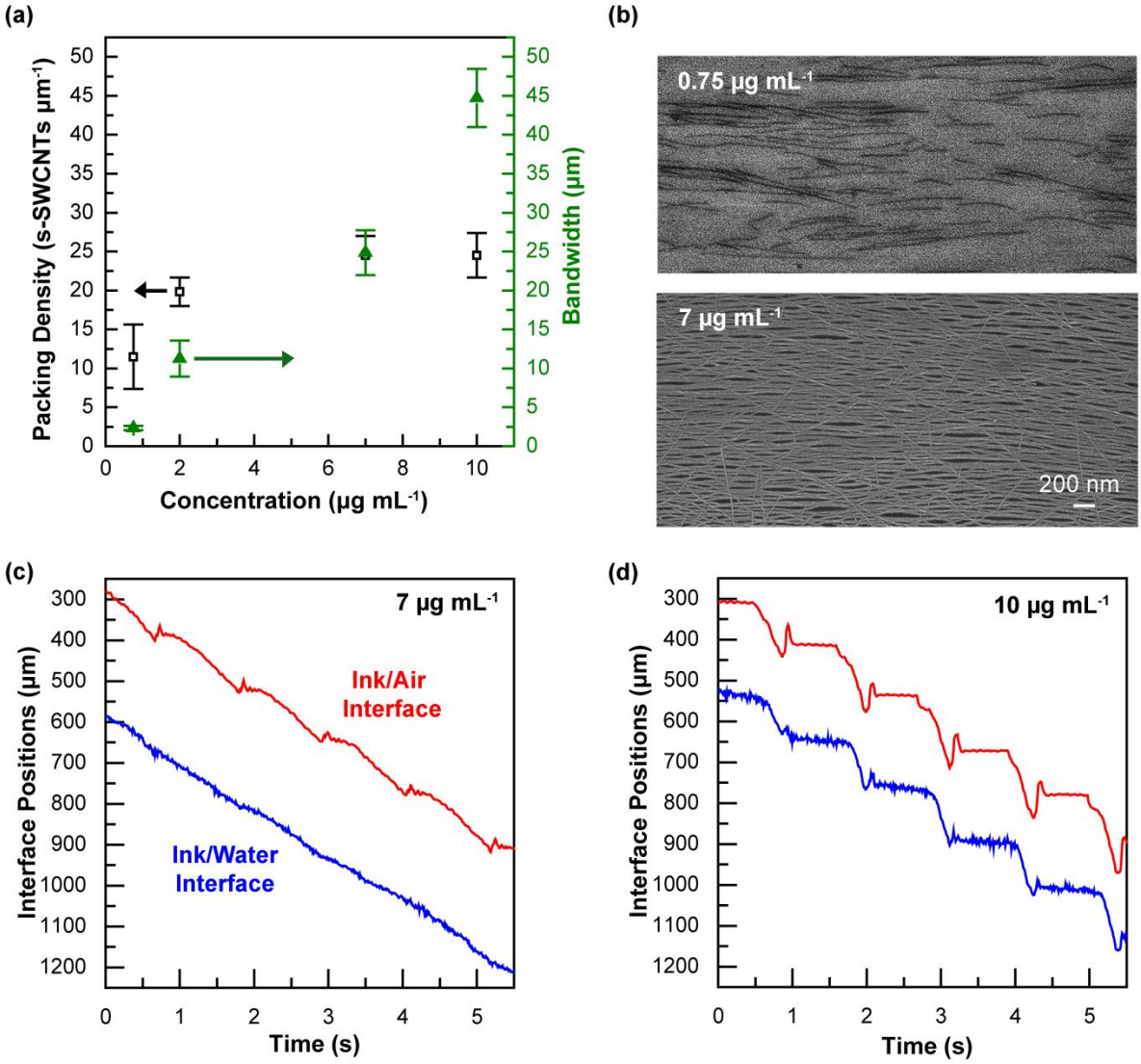


**Figure 2.4**. (a) Bandwidth and packing density of deposited aligned nanotubes (s-SWCNTs in figure) increase with increasing concentration. Packing density initially increases and then quickly saturates at ~24 nanotubes µm$^{-1}$. (b) SEM micrographs showing packing density and alignment at 0.75 and 7 µg mL$^{-1}$. (c-d) Traces of ink/air/substrate and ink/water/substrate contact lines in the frame of the substrate from concentrations (c) 0.25 µg mL$^{-1}$ and (d) 10 µg mL$^{-1}$. Larger concentrations show more pinning/depinning of the contact lines. In this figure, the substrate lift rate is held constant across experiments at 7 mm min$^{-1}$.

The bandwidth is also affected by the concentration of nanotubes in the ink. **Fig. 2.4c-d** are back-imaging traces of the contact lines for nanotube depositions using ink concentrations of 0.25 and 10 µg mL$^{-1}$, respectively. At 0.25 µg mL$^{-1}$, there is relatively minimal pinning and depinning behavior yielding a narrow bandwidth. Determining the smallest bandwidth that can be achieved with this method is difficult

because the packing density also simultaneously decreases as the nanotube concentration is decreased, eventually yielding ill-defined bands (**Fig. 2.4b**). At higher nanotube concentrations, there is more pinning, lasting for longer duration, yielding a larger deposited bandwidth upon depinning.

**2.2.4 Aligned nanotube arrays over 2.5 x 2.5 cm$^2$ via Dose FESA.** We demonstrate that FESA can be used to deposit well-aligned nanotubes over large areas of 2.5 × 2.5 cm$^2$ by optimizing the deposition parameters. For this demonstration, 1.5 µL doses of ink at a nanotube concentration of 10 µg mL$^{-1}$ are pulsed at a frequency of 50 min$^{-1}$ with a substrate lift rate of 9 mm min$^{-1}$. As a result, it takes less than 3 min to deposit aligned bands of nanotubes across the entire substrate. An optical image of the resulting sample is shown in **Fig. 2.5a**. In this image, obtained using a conventional digital camera (Nikon D3100), the aligned bands of nanotubes are visible and appear purple (**Fig. 2.5a,b**).

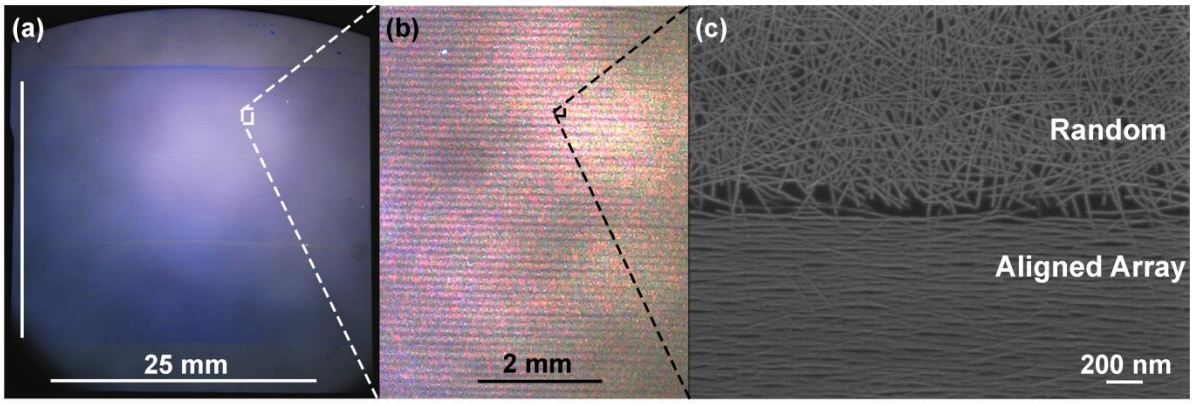


**Figure 2.5.** Dose FESA is a scalable process for creating aligned arrays of nanotubes. (a-c) Dose FESA substrate of aligned nanotubes on a centimeter, millimeter, and nanometer scale, respectively. (a) and (b) are optical photographs. In (a), the aligned nanotube bands appear purple. In (b) the aligned bands are dark. (c) shows an SEM micrograph of dense, well-aligned nanotubes at the top of a band.

The SEM micrograph in **Fig. 2.5c** characterizing the top of an aligned nanotube band shows that the areas between bands of aligned nanotubes contain randomly oriented nanotubes. It is not yet clear whether the random nanotubes deposit from the evaporating ink/air/substrate contact line, from the bulk of

the ink solution, or from the ink/water/substrate after the bands of aligned nanotubes are deposited. However, these randomly oriented nanotubes can be removed using conventional lithography procedures as a result of the highly regular band spacing. We also observe the bandwidth narrowing from the center of the substrate 122 ± 13 μm to 25 ± 6 μm near the edge of the substrate. Future work will focus on improving the uniformity of the aligned nanotubes across the width of the substrate. This demonstration shows that the build-up of nanotubes at the ink/water interface, the pinning and depinning of the contact lines, and the deposition of aligned bands of nanotubes can be iteratively repeated many times without loss of fidelity, enabling large-area scaling.

**2.3 Conclusion.**

In this chapter, we show that FESA can be scaled to deposit nanotubes over areas of 2.5 × 2.5 $cm^2$ while also retaining a high degree of nanoscale alignment, signifying an important step towards wafer-scale alignment of nanotubes. We also investigate the mechanism of the controlled alignment of nanotubes via FESA. While evaporation is part of the FESA acronym, we show that evaporation is not essential to the alignment of nanotubes in this technique. The alignment occurs at the buried ink/water interface where evaporation is not expected to have a significant effect. Therefore, the mechanism that drives nanotube alignment during FESA is entirely distinct from previously reported evaporative self-assembly methods.[53] During FESA, the deposition of the aligned nanotubes occurs at the ink/water/substrate contact line as this contact line falls and sweeps across the substrate after the depinning of the ink/water/substrate and ink/air/substrate contact lines following the delivery of a dose of ink. We also find that the concentration of the nanotube ink can be used to control the bandwidth and packing density of the aligned nanotubes. Our data additionally show that nanotubes collect and confine at the ink/water interface and that a small change in nanotube concentration results in a large change in packing density until the packing density saturates. The insight regarding FESA mechanisms provided here may create new opportunities for scaling and improving nanotube alignment and in particular implementing to realize continuous rather than banded

aligned arrays of nanotubes. New opportunities may also arise for exploiting confinement at liquid-liquid interfaces and the FESA process to align and deposit other types of anisotropic nanostructures beyond nanotubes.

## 2.4 Materials and methods.

**2.4.1 Preparation of PFO-BPy wrapped nanotubes.** Nanotubes are isolated using a 1:1 ratio by weight of arc-discharge nanotube soot (698695, Sigma-Aldrich) and a polyfluorene derivative, poly[(9,9-dioctylfluorenyl-2,7-diyl)-alt-co-(6,6′-{2,2′-bipyridine})] (PFO-BPy), (American Dye Source, Inc., Quebec, Canada; #ADS153-UV), which are each dispersed at a concentration of 2 mg $mL^{-1}$ in toluene. 60 mL of this mixture is sonicated with a horn tip sonicator (Fisher Scientific, Waltham, MA; Sonic dismembrator 500) for 30 min. The solution is centrifuged in a swing bucket rotor at $3 \times 10^5$ $g$ for 10 min to remove undispersed material. The top 90% of the supernatant is collected, centrifuged for 18-24 h, and dispersed in toluene with sonication via the horn tip sonicator. This latter process is repeated three times to rinse off as much excess PFO-BPy as possible. The final solution is prepared by horn-tip sonication of the rinsed nanotube pellet in chloroform (stabilized with ethanol from Fisher Scientific, #C606SK-1). The concentration of the nanotubes is determined using optical cross sections from the $S_{22}$ transition.[27]

**2.4.2 Preparation of substrates for FESA processes.** $Si/SiO_2$ and quartz substrates are employed. The substrates are cleaned with a piranha solution of 2:1 ratio by volume of $H_2SO_4$ (91 – 92.5%):$H_2O_2$ (30%) in a 340 mL crystallizing dish on a hotplate set to 110 °C for 60 min, rinsed with deionized water, and dried with $N_2$. After piranha treatment, the substrates are exposed to hexamethyldisilizane (HMDS) vapor (Solitec VBS200 HMDS Prime Oven) for 10 s to create a hydrophobic self-assembling monolayer (vapor deposition). Prior to HMDS deposition, the substrates are baked in an ambient environment on a hotplate set to 205 °C for 325 s to drive off water from the substrate surface. The water contact-angle on the HMDS treated substrates is ~45°.

**2.4.3 Back-imaging of contact line dynamics.** Transparent quartz substrates are used to enable optical imaging of the FESA process in transmission. As shown in **Fig. A2**, the back of each quartz substrate is coated with polytetrafluoroethylene (PTFE) to subdue the water contact line on the back of the substrate. This allows clear imaging of the buried ink/water interface through the substrate during deposition. The PTFE films are fabricated from 2% by mass PTFE (Sigma-Aldrich 469629) in perfluorodecalin 95% (Sigma-Aldrich P9900). This solution is spun-cast on the quartz substrates at 2500 rpm. The films are then baked in $N_2$ on a 200 °C hot plate for 1 h. Images are recorded at 100 frames per second (fps) using a Basler acA2000-165uc camera mounted with a Navitar 12*x* objective lens. The images are backlit using a Fiber-Lite PL-800 light mounted with fiber optics.

**2.4.4 MATLAB processing on images.** Tracking of the contact lines is performed using MATLAB. First, original red, green, blue (RGB)-colored images are converted to grayscale-level arrays, and contrast and brightness are adjusted to emphasize the interfaces. A median filter is subsequently applied to smooth out pixel noise. The exposure time and lighting are constant during the experiment so the same adjustments (contrast, brightness, and filter) are applied to every image in the set. After converting to grayscale, the ink/air/substrate contact line is located by finding the local maximum of the gradient of grayscale values in each column of pixels. The contrast at the ink-water-substrate contact line is much weaker and requires a different approach. First, the area of interest is limited to the region below the previously detected ink-air-substrate contact line. The reduced image is binarized using Otsu's algorithm (*imbinarize* function in MATLAB) in order to show the ink film as bright pixels (see **Fig. A5**). Spurious bright pixels are filtered out using an in-house algorithm. The ink/water/substrate contact line is determined as the bottom boundary of the bright region corresponding to the ink film. Both detected contact lines are finally smoothed using a moving average.

### 2.4.5 Deposition parameters for figures.

**Figure 2.1.** The ink concentration is 10 μg $mL^{-1}$. 15 μL of water and 10 μL of ink are used. **Figure 2.2.** The ink concentration is 10 μg $mL^{-1}$. The ink doses are 1 μL. The needle/substrate distance is 1.27 mm. The dose frequency is 50 $min^{-1}$. The substrate lift rate is 7 mm $min^{-1}$. **Figure 2.3.** The ink concentration is 10 μg $mL^{-1}$. The ink doses are 1 μL. The needle/substrate distance is 1.27 mm. The dose frequency is 50 $min^{-1}$. The substrate lift rate is 7 mm $min^{-1}$. **Figure 2.4.** The ink doses are 1 μL. The needle/substrate distance is 1.27 mm. The dose frequency is 50 $min^{-1}$. The substrate lift rate is 7 mm $min^{-1}$. **Figure 2.5.** The ink concentration is 10 μg $mL^{-1}$. The ink doses are 2.5 μL. The dose frequency is 50 $min^{-1}$. The substrate lift rate is 9 mm $min^{-1}$. The needle/substrate distance is 3.8 mm. A larger needle/substrate distance is used compared to the depositions in **Figs. 2.2, 2.3 and 2.4** because the ink volume is larger and more time (i.e. distance for the ink to travel before hitting the substrate) is needed to form a uniform ink front.

# **Chapter 3.** 2D nematic carbon nanotube assemblies aligned by flow

Chapter 3 was adapted from Jinkins, K. R., Saraswat, V., Jacobberger, R. M., Berson, A., Gopalan, P., & Arnold, M. S. 2D Nematic Carbon Nanotube Assemblies Aligned by Flow. *In preparation.* (2020). K.R.J. and M.S.A. performed all experiments, data collection, and analysis. V.S. fabricated graphene control samples for normalization of Raman measurements (**Fig. 3.1g-i**). R.M.J. performed all 400 °C vacuum anneals on nanotube films measured using Raman spectroscopy (**Fig. 3.1g-i**) and films used for devices (**Fig. 3.5**) M.S.A., P.G., and A.B. supervised the work. All authors contributed to data interpretation. K.R.J. drafted the manuscript.

**Abstract:** Semiconducting carbon nanotubes promise to enable faster performance and lower energy consumption in field-effect transistors (FETs); however, to fully exploit their electronic properties, nanotubes must be aligned in densely packed arrays. In this work, we demonstrate that nanotubes trapped at a two-dimensional liquid/liquid interface self-organize due to liquid crystal phenomena and the addition of flow induces global alignment in the resulting nanotube nematic liquid crystal assemblies. We use this understanding to fabricate highly aligned nanotube arrays (within ±5.7°) across 10 cm substrates. Due to the liquid crystal phenomena governing assembly, nanotube ordering improves with increasing concentration and decreasing temperature. The high array uniformity translates to excellent FET characteristics and reproducibility with high on-state current density averaging 520 μA $\mu m^{-1}$ at –0.6 V and FET to FET variation of only 19%. The ordering of two-dimensional nematic carbon nanotube assemblies using flow provides a promising route towards fabricating uniform films of aligned nanotubes for semiconductor electronics.

**3.1 Introduction.**

Self-assembly of nanoparticles at liquid interfaces offers an attractive route to fabricate supramolecular arrangements of nanostructures.[59–61] For example, this assembly is highly dynamic, enabling defects to be corrected quickly, as opposed to assembly and deposition directly on substrates. Nanoparticle adsorption at liquid/liquid interfaces occurs to minimize liquid/liquid interfacial energy, and the size of the nanoparticles, interfacial tension, and particle surface wettability all affect interface adsorption. When anisotropic particles, such as rods, collect at liquid/liquid interfaces, liquid crystal nematic assemblies can form due to the high concentration of rods and additional two-dimensional confinement at the interface.[62,63]

In this chapter, we demonstrate carbon nanotubes that collect at a liquid/liquid interface can also form two-dimensional nematic liquid crystal assemblies. These assemblies are comprised of individual domains of highly aligned nanotubes; but, without flow, there is no global alignment. Tangential flow aligns these domains – enabling the continuous wafer-scale deposition of aligned and densely packed nanotubes (onto target substrates) from the highly ordered liquid/liquid interface.

Previously, it has been shown that carbon nanotubes can collect at the interface between two immiscible liquids; however, these studies have focused on multi-walled carbon nanotubes (less useful for semiconductor electronics) that form only locally aligned nanotube rafts[58,64] or have resulted in relatively thick bundles or mats of random nanotubes.[65–68] Separately, the bulk liquid crystal assembly of nanotubes (i.e., not at a liquid/liquid interface) has also been studied;[69] however, these works demonstrate thick multilayer nanotube films with[37,70,71] or without[72,73] global alignment and rarely demonstrate sub-monolayer aligned films.[74]

As discussed in Chapter 2, a liquid/liquid interface has been previously used to deposit aligned, semiconducting, single-walled carbon nanotubes on substrates from nanotube ink droplets spread on a water subphase in the FESA technique. Nanotubes dispersed in the ink accumulate at the liquid/liquid interface during the spreading and deposit onto substrates creating stripes of aligned nanotubes across limited regions of wafers.[75] While we hypothesized the alignment must be occurring due to shear, the exact roles of flow

and liquid crystal assembly are unknown. The excellent alignment, individualization, and packing of nanotubes in FESA films have enabled FETs with on-state current densities exceeding that of Si and GaAs devices[22,76] and also high-speed radio-frequency devices.[77] However, the drop-by-drop nature is irreproducible, inherently difficult to scale (the best alignment has been demonstrated to occur across only 15 mm of a 100 mm wafer[78]), and problematically yields stripes of aligned nanotubes that are either separated by randomly oriented nanotubes[75] or overlap.[78]

In this chapter, we demonstrate that nanotubes that collect and confine at a two-dimensional liquid/liquid interface self-organize due to liquid crystal phenomena and flow induces global alignment of the nanotube liquid crystal assemblies. The ink layer is well-defined with constant thickness and tangential flow velocity, and therefore this assembly can be exploited in a process that is continuous and capable of uniformly depositing aligned nanotubes across target substrates (in contrast with the drop-by-drop nature of FESA). We call this process two-dimensional nematic tangential flow interfacial self-assembly (TaFISA). Unlike bulk liquid crystals of carbon nanotubes, assembly at a two-dimensional interface is ideal for achieving the deposition of sub-monolayers of highly aligned carbon nanotubes at intermediate packing densities needed for semiconductor electronics. We exploit TaFISA to fabricate highly aligned nanotube arrays (within ±5.7°) continuously across 10 cm wide substrates. Due to liquid crystal phenomena governing the assembly, ordering improves with increasing concentration and decreasing temperature. The excellent alignment in TaFISA nanotube arrays and the continuous nature of the technique are significant steps toward the uniformity and scalability that will be needed to exploit carbon nanotubes in industrial electronics.

### 3.2 Results and discussion.

The apparatus for studying the interfacial self-assembly of carbon nanotubes and subsequent deposition onto target substrates is shown in **Fig. 3.1a-c**. An ink of polymer-wrapped semiconducting carbon nanotubes (**Fig. 3.1a**), with concentration on the order of 100 μg $mL^{-1}$, flows through a channel

formed by a target substrate and a sacrificial barrier suspended in a water subphase (**Fig. 3.1b**). Typical ink layer thicknesses are around 0.3 mm and the channel width (i.e., separation between substrate and sacrificial wall) is roughly 3 mm. Uniform films of highly aligned nanotubes are deposited by translating the channel through this flowing ink/water interface.

Evidence of two-dimensional nematic assembly phenomena is shown in **Fig. 3.1d** (without added flow) and **Fig. 3.1e** (with flow). Even without flow, locally ordered domains of densely aligned nanotubes form (observed underneath spurious random nanotubes), distinct from the disordered films of randomly oriented nanotubes that are created by dip-coating substrates into bulk solutions of nanotube ink without the two-dimensional liquid/liquid interface.[79,80] The approximate domain boundaries are outlined in black, and the characteristic orientation within each domain (termed the director) is marked by red arrows in **Fig. 3.1d**. Without flow, the orientation of each domain is different, and the nanotubes lack global order.

With flow, the domains globally align parallel to the direction of flow (**Fig. 3.1e**). On a 1.5 × 1.5 $\mu m^2$ scale, the alignment is excellent with a half-width at half-maximum (HWHM) in angular spread of 5.7° (calculated order parameter = 0.90). This narrow spread is comparable to the aligned regions of FESA (**Fig. 3.1f**), however, the TaFISA arrays are continuously deposited across the substrate, in contrast to the striped morphology of FESA films. The continuous, uniform nature of TaFISA, both without and with flow, is evidenced by Raman spectroscopy maps of relative nanotube density in **Fig. 3.1g,h**, respectively, in comparison to striped FESA films in **Fig. 3.1i**.

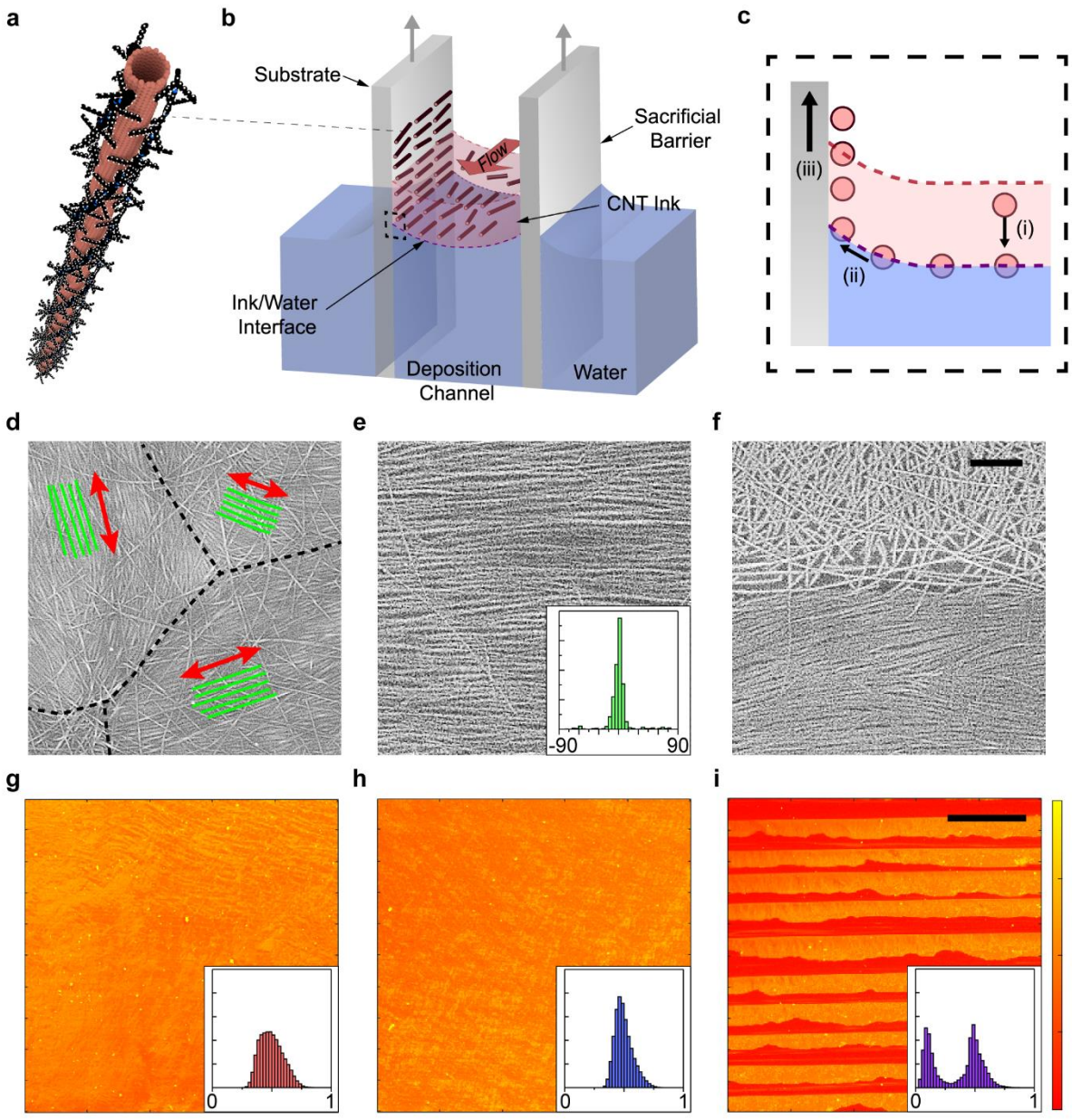


**Figure 3.1.** Experimental apparatus for studying interfacial assembly in TaFISA and effect of flow on alignment. (a) Polymer wrapped arc-discharge carbon nanotube used in this work. (b) Experimental apparatus for TaFISA. (c) Magnified view of ink/water interface and alignment process shown in (b). (d,e) SEM of TaFISA films obtained without flow and with flow. The inset in (e) is a histogram (manually extracted) of orientation angle, weighted by nanotube length. The horizontal-axis varies from –90 to 90°. (f) SEM from FESA film. The scalebar in (f) is 250 nm and applies to (d-f). (g-i) Raman spectroscopy maps of relative carbon nanotube density from each respective film in (d-f). Color scalebar at right of panel (i) is linear and applies to (g-i). The scalebar in (i) is 250 µm and applies to (g-i). Histograms of relative nanotube density from the Raman maps are included as insets in each panel.

With increasing flow velocity, local directors become more aligned with one-another – even over large areas – as characterized and quantified in detail in **Fig 3.2**. Large (greater than $6 \times 6$ μm$^2$) SEM images of assemblies deposited using a volumetric flow rate of 0, 1, and 4 mL min$^{-1}$ are compared in **Fig. 3.2a-c**, respectively. Two-dimensional fast Fourier transforms are used to quantify and map local director orientation as shown in red. This mapping is conducted on six different areas of each sample (see Appendix B **Figs. B1 and B2**), and cumulative distributions of director orientations are shown in **Fig. 3.2d-f**.

Without flow, the directors are oriented at all angles, showing a lack of global ordering but with local ordering in domains 3 to 30 μm in extent (**Fig. 3.2a,d**). With increasing flow (1 mL min$^{-1}$), a clear preferential orientation appears in the director distribution with a HWHM of 37.3° (**Fig. 2b,e**); and, at high flow (4 mL min$^{-1}$), the distribution narrows, with a HWHM of 16.1°, centered around 0° -- the direction of flow (**Fig. 3.2c,f**). Director orientation spread in TaFISA films (**Fig. 3.2f**, blue distribution) reduces at high flow rates, nearing that of the local nanotube orientation histogram (**Fig. 3.1e** inset and **Fig. 3.2f** dashed black line).

These trends are moreover qualitatively observed over an even larger scale ($1.4 \times 1.4$ mm$^2$) in the polarized optical microscopy (POM) images in **Fig. 3.2g-i**, where bright yellow corresponds to nanotubes aligned with the flow direction (horizontal) and darker regions correspond to misaligned nanotubes. The nanotube density can also be smaller in these darker regions (**Fig. B3**). Without flow, the POM images are composed of roughly equal amounts of bright and dark regions indicating a lack of global alignment (**Fig. 3.2g**). At intermediate flow (1 mL min$^{-1}$), the POM images become more homogeneous, and at a high flow (4 mL min$^{-1}$), the POM images are nearly uniform in intensity, with all nanotube domains oriented roughly with the flow direction, and deviation limited to highly localized regions.

An SEM image of one of these highly localized regions is shown in **Fig. 3.2h** insert. These nanotube arrangements correspond to liquid crystal defects or disclination lines, i.e., locations where the director cannot be determined. Liquid crystal defects are characterized with a charge related to the direction and number of times the director rotates $2\pi$ after traversing a circle around the defect. The liquid crystal defects in **Fig. 3.2h** insert have charges of -1/2 (blue) and +1/2 (red). The uniformity at a flow rate of 8 mL min$^{-1}$

is similar to that at 4 mL min$^{-1}$, with marginal increase in defects; however, increasing the flow rate to 16 mL min$^{-1}$ significantly deteriorates ordering, introduces more substantial defects, and results in incomplete coverage (**Fig. B4**). Thus, there is a trade-off between shear-inducing alignment and assembly degradation. Possible factors that degrade the film are flow instability and director turbulence.[81]

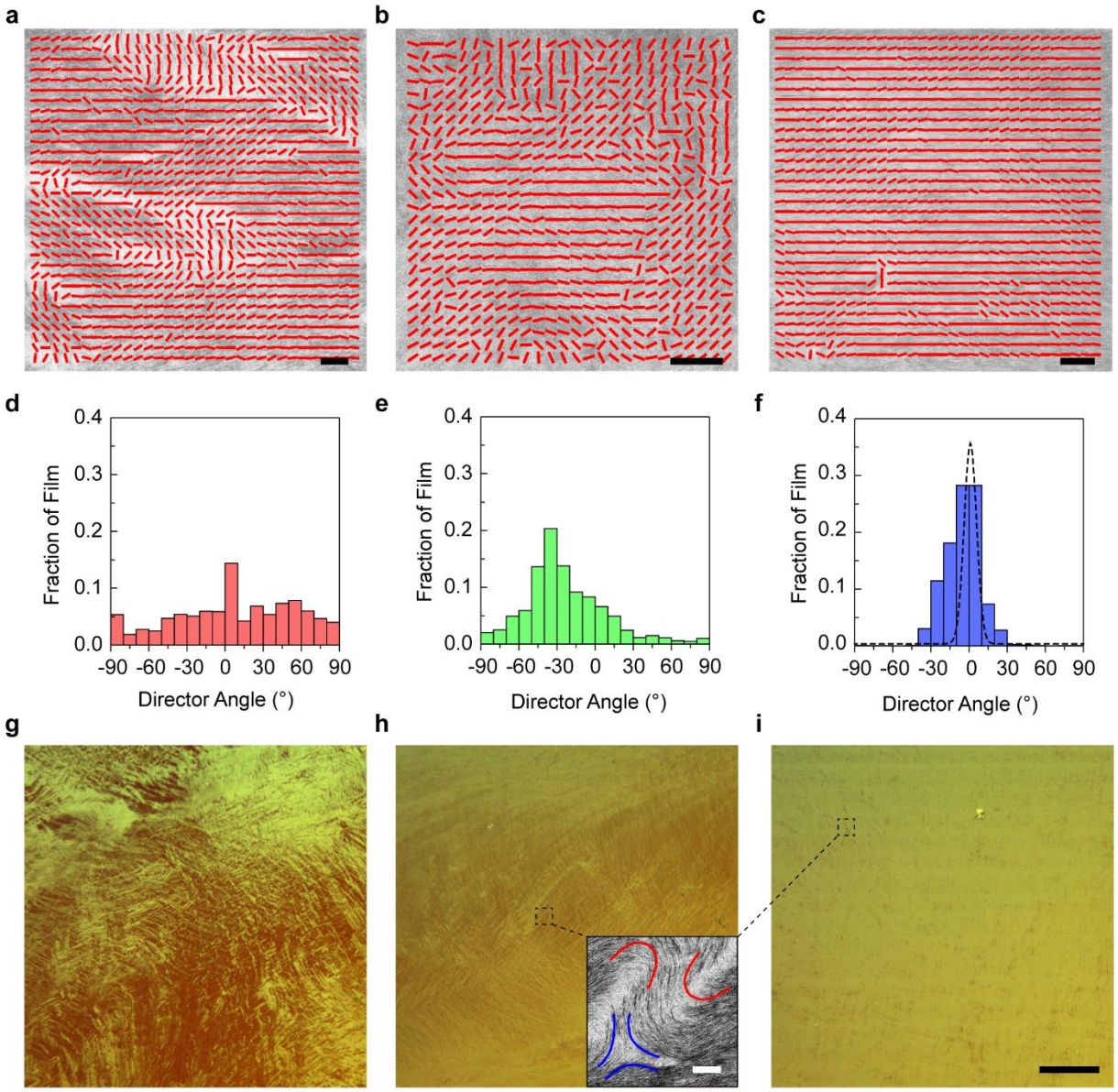


**Figure 3.2.** Quantifying effect of flow rate on ordering in TaFISA films. (a-c) SEM images from TaFISA films fabricated with volumetric flow rates of 0, 1, and 4 mL min$^{-1}$, respectively, overlaid with local director orientations obtained from two-dimensional fast Fourier transform analysis. The scalebars in (a-c) are 1 µm, and images without overlays are shown in **Fig. B5**. (d-f) Director orientation distributions at flow rates of 0, 1, and 4 mL min$^{-1}$. The dashed line in (f) is the Gaussian fit of the local orientation histogram from

**Fig. 3.1i**. (g-i) POM images from TaFISA films fabricated with volumetric flow rates of 0, 1, and 4 mL $min^{-1}$, respectively. Scalebar in (i) is 250 µm and applies to (g-i). SEM image inset in (h) shows -1/2 (blue) and +1/2 (red) liquid crystal defects in TaFISA films. Scalebar in inset is 2 µm.

Ordering in TaFISA films dramatically improves with increasing concentration (**Fig. 3.3a-e**), indicating the importance of collective interactions among nanotubes and further evidencing underlying lyotropic liquid crystal phenomena. At low ink concentrations of 0.1 and 1 µg $mL^{-1}$ (**Fig. 3.3a,b**), few poorly aligned nanotubes are deposited, despite the high flow rate (4 mL $min^{-1}$). Collective interactions begin to create local order as the concentration increases to 5 or 25 µg $mL^{-1}$ (**Fig. 3.3c,d**) and then reach a high degree of order at a concentration of 100 µg $mL^{-1}$ (**Fig. 3.3e**). The linear nanotube packing density increases with concentration, reaching 50 ± 4 $\mu m^{-1}$, near the intermediate density needed for carbon nanotube based FETs, at an ink concentration of 100 µg $mL^{-1}$ (**Fig. 3.3e,f**). At higher ink concentrations, such as 200 µg $mL^{-1}$, the size of defect regions increases (**Fig. B6**)—possibly because of increased heterogeneity within the ink caused by nanotube bundles and aggregates that form at elevated concentrations.[72,82–84]

The concentration dependence data inform us about the mechanism and dimensionality of the underlying liquid crystal phenomena. In bulk solution, Onsager's rigid rod theory predicts the onset of liquid crystal assembly at a concentration of 13.3 mg $mL^{-1}$ (for the dimensions of nanotubes used here, see calculation in Appendix B).[85,86] Experimental work has observed liquid crystal behavior in bulk nanotube solutions at concentrations as much as an order of magnitude below the prediction of Onsager's theory.[71] In contrast, here, liquid crystal behavior emerges at dramatically lower concentration, with optimal ordering obtained at 100 µg $mL^{-1}$ and nanotube ordering and liquid crystal defects (-1/2 defect seen in **Fig. 3.3c**) observed at concentrations as low as 5 µg $mL^{-1}$. The onset of nematic assembly at orders of magnitude lower concentration than theory and past experiments is likely a result of the two-dimensional confinement and concentration of nanotubes at the liquid/liquid interface.

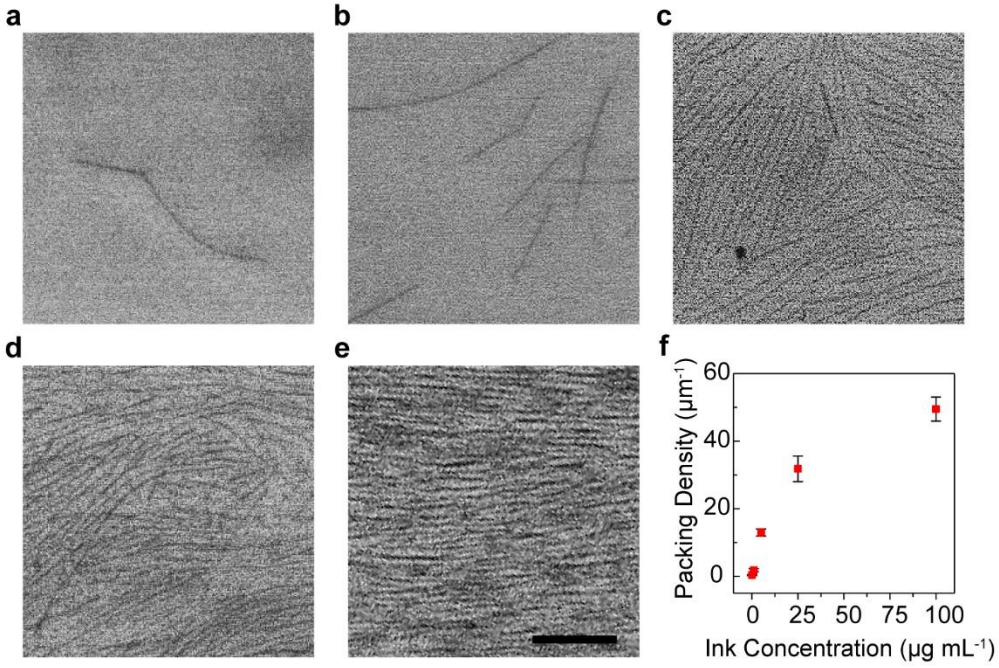


**Figure 3.3.** Effect of concentration on TaFISA films. (a-d) SEM images of TaFISA films fabricated using nanotube ink concentrations of 0.1, 1, 5, 25, and 100 μg $mL^{-1}$, respectively. The scalebar in (e) is 500 nm and applies to (a-e). (f) Carbon nanotube packing density as a function of ink concentration.

The continuous arrays of well-aligned nanotubes assembled by TaFISA (at optimized flow rate and ink concentration) are punctuated only by small regions of disorder, such as liquid crystal defects. Decreasing temperature provides a route to suppress this disorder,[87] for example, by suppressing thermal motion and increasing the relative importance of anisotropic van der Waals interactions among mesogens.[81] The significant effect of temperature on TaFISA is clearly observed in the POM images presented **Fig. 3.4**, which become dramatically more uniform by decreasing temperature from 35 °C (**Fig. 3.4a**) to 23 °C (**Fig. 3.4b**) to 10 °C (**Fig. 3.4c**). The figure inserts quantify the distribution of POM pixel intensities, which converge to a uniform, tight distribution at 10 °C, evidencing a substantial reduction in disorder and defects. The nanotube assemblies obtained at 10 °C are highly ordered both on a large scale (0.7 × 0.7 $mm^2$ area) as shown in **Fig. 3.4c** and on a local scale as shown in a corresponding SEM image in **Fig. 3.4d**.

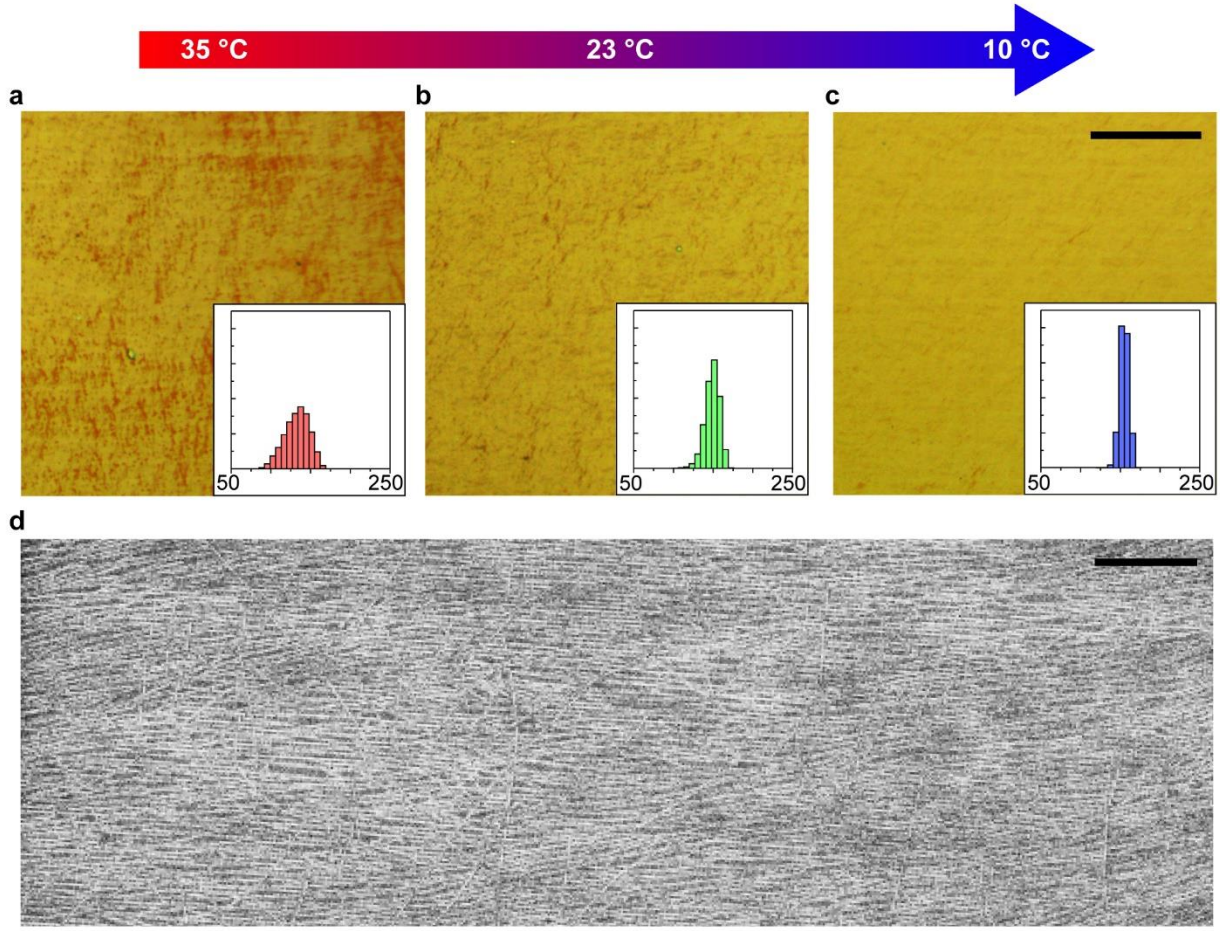


**Figure 3.4.** Effect of temperature on TaFISA films. (a-c) POM images from TaFISA films deposited at 35, 23, and 10 °C, respectively. The scalebar in (c) is 200 µm and applies to (a-c). In (c), faint horizontal lines are observed spaced with a regular period of 29.6 µm. The substrate motor lift-rate of 2666.7 µm $s^{-1}$ divided by the line period corresponds to a frequency of 90 Hz, matching a frequency of 90 Hz inherent to the substrate lift motor control; therefore, these faint lines are artifacts. Histograms of POM image pixel intensity are shown in the insets to (a-c). (d) SEM image from the sample in (c). The scalebar in (d) is 500 nm.

FET measurements demonstrate that TaFISA arrays have excellent electrical characteristics with substantially reduced variation compared to FESA films (**Fig. 3.5**). To quantify uniformity, FETs with 100 nm channel lengths are fabricated linearly across large-area TaFISA and FESA assemblies. Representative source-drain current ($I_{DS}$) versus gate-source bias ($V_{GS}$) characteristics are shown in **Fig. 3.5b**, for FETs fabricated from TaFISA arrays (black) and aligned (red) and unaligned (blue) FESA film regions at source-drain bias ($V_{DS}$) of –1 V. The FETs turn on at negative $V_{GS}$, typical of p-type nanotube FETs with Pd source and drain contacts. The **Fig. 3.5b** insert shows representative $I_{DS}$ versus $V_{DS}$ characteristics for TaFISA

FETs, as $V_{GS}$ is varied from –8 to –2 V. Typical on-state current densities reaches 520 μA μm$^{-1}$ (corresponding to 11 μA per nanotube) at a $V_{DS}$ of –0.6 V and then saturate at more negative $V_{DS}$. In the linear regime at small $V_{DS}$ of –0.1 V, the typical on-state conductance is 1100 μS μm$^{-1}$ (corresponding to 0.29 $G_0$ per nanotube, where $G_0 = 2e^2/h = 77$ μS is the quantum conductance) demonstrating that charge transport in TaFISA arrays is approaching the quantum conductance limit. The performance matches state-of-the-art FESA FETs;[22] except, TaFISA characteristics are uniformly obtained continuously across the substrate as opposed to selectively fabricated on well-ordered stripe regions.

The uniformity in on-current at $V_{DS}$ = –1 V is quantified in **Fig. 3.5c-e**. Comparing all 58 TaFISA and 117 FESA devices measured (**Fig. 3.5c**), the TaFISA FETs demonstrate a mean normalized standard deviation of only 19% (540 ± 100 μA μm$^{-1}$) as compared to 52% for FESA FETs (210 ± 110 μA μm$^{-1}$). The large variation in FESA FETs is a direct result of the stripe morphology—the devices fabricated on aligned regions (red), on average, exhibit 2.4× on-current than FETs fabricated on random regions (blue). Even in implementations of FESA that have minimized the random regions, the variation in FET performance can be large. For example, a mean normalized standard deviation of 25% is obtained in ref. [78] only after excluding many lower performing devices.

The correlation between array morphology and FET performance is visualized in **Fig. 3.5d,e**, in which the nanotube morphology in the channel and on-current at $V_{DS}$ = –1 V for those same FETs are directly compared. Disordered regions cause suppression of the on-current in FESA FETs, resulting in non-uniform electrical characteristics (**Fig. 3.5d**). In contrast, on-current is more consistent in TaFISA FETs because the channels are uniformly comprised of aligned nanotubes, yielding more homogeneous FET performance (**Fig. 3.5e**).

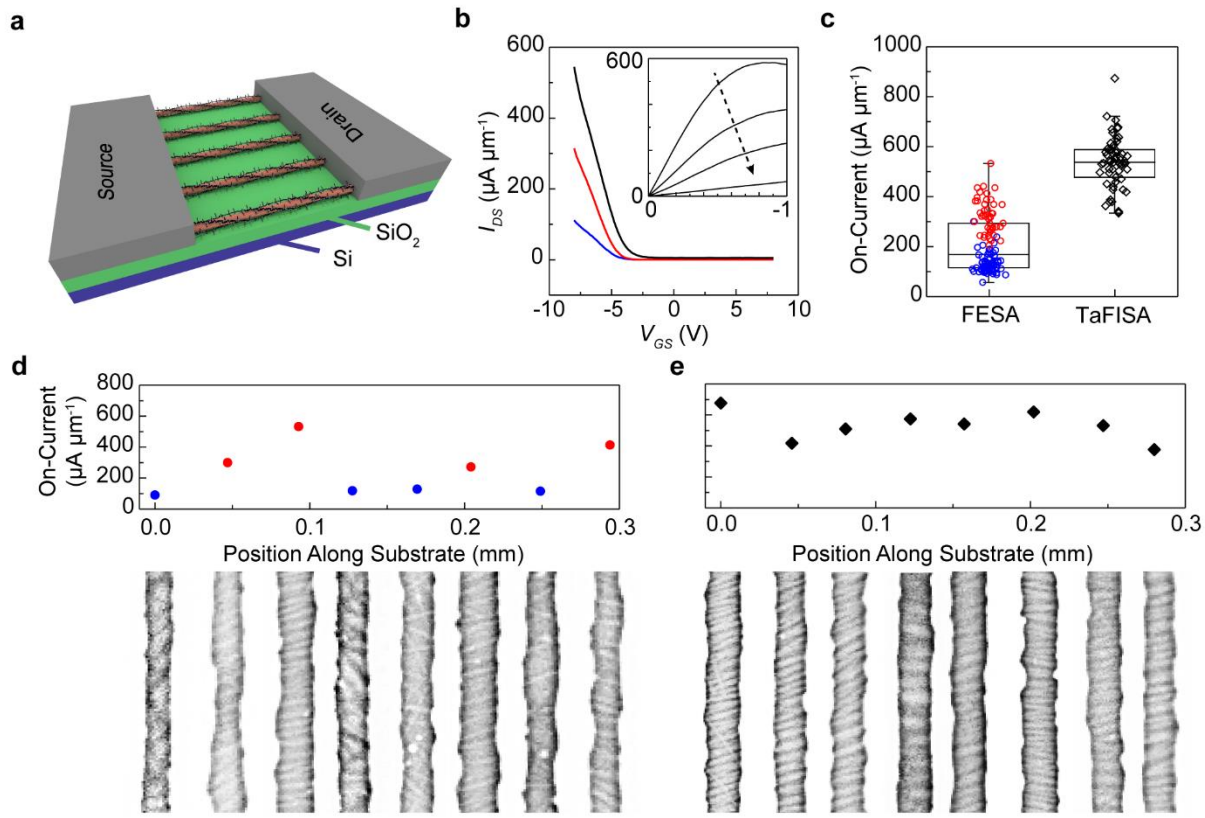


**Figure 3.5.** Charge transport measurements of FETs fabricated on FESA and TaFISA carbon nanotube arrays. (a) Schematic of a nanotube array aligned on a $SiO_2$/Si back gate with top source and drain contacts. (b) $I_{DS}$ versus $V_{GS}$ curves for representative TaFISA (black) and FESA (aligned – red, unaligned – blue) FETs. On average, the on/off ratio from all FETs is greater than $10^2$ at $V_{DS}$ of –1 V. Inset: $I_{DS}$ versus $V_{DS}$ curves as $V_{GS}$ is varied from –8 to –2 V (top to bottom) in 2 V steps. (c) On-current of all FESA and TaFISA FETs measured at $V_{DS}$ of –1 V. The lower on-current of the aligned FESA stripes compared to TaFISA arrays is attributed to lower nanotube packing density, 38 ± 2 versus 50 ± 4 $\mu m^{-1}$ (data in terms of on-current per nanotube is shown in **Fig. B7**). (d) On-current versus position across the substrate for selected individual FESA FETs. The channels of the FETs in each data point are shown directly below in the SEM images. From left to right, the channel lengths are: 93, 100, 118, 115, 113, 124, 111, and 95 nm. (e) On-current versus position along the substrate for individual TaFISA FETs. The effects of charging vary, causing the nanotubes to appear different in each image. From left to right, the channel lengths are: 114, 121, 126, 120, 101, 127, 129, and 134 nm.

The scalability of TaFISA is demonstrated by aligning nanotubes uniformly across the majority of a 10 cm wide wafer piece (**Fig. 3.6**). The ink is injected in the channel at position (i). The flow develops between positions (i) and (ii) where few nanotubes are deposited. Between positions (ii) and (iii), the flow is developed, and aligned nanotubes are uniformly deposited onto the substrate as it is withdrawn from the water subphase. After position (iii), the flow is perturbed by end-effects encountered at the edge of the

wafer, related to the curvature of the water meniscus and divergence of the flow as it exits the channel. Raman spectroscopy maps of nanotube density are measured across the 10 cm wide wafer and overlaid on a photograph of the wafer in **Fig. 3.6a**. The Raman maps demonstrate that the deposition is uniform across the region where the flow is fully developed (~60% of the wafer), confirming the scalability of TaFISA. A histogram of the density analyzed between positions (ii) and (iii) is shown in **Fig. 3.6b** and shows density varies with a HWHM of only 19%. SEM images (**Fig. 3.6c**) obtained across the substrate also confirm the continuous deposition of highly aligned, densely packed nanotubes.

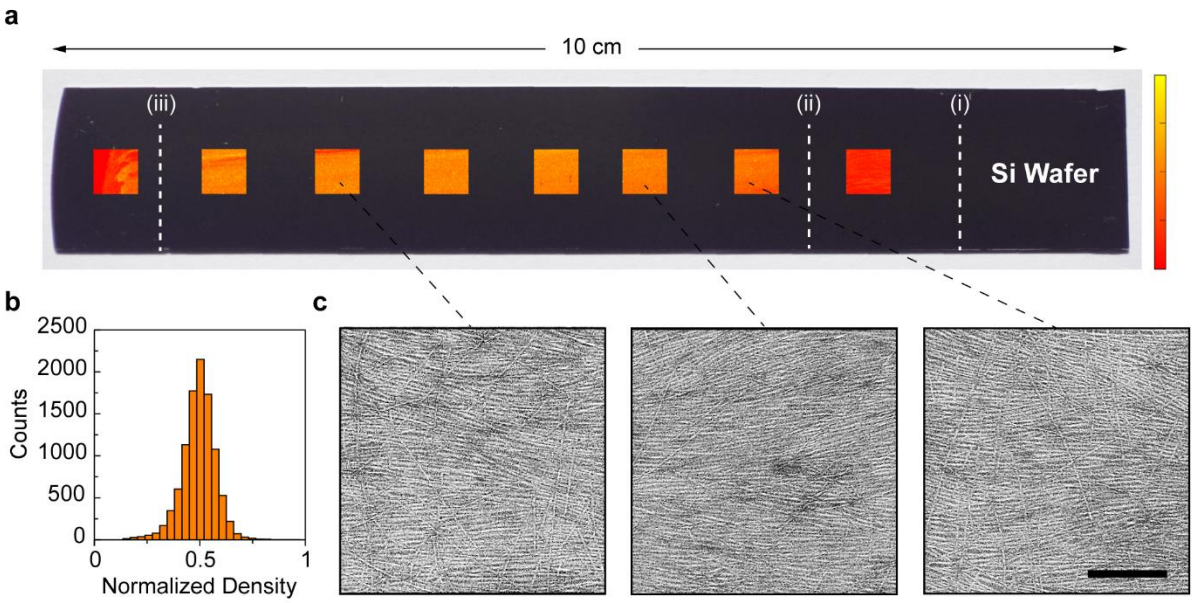


**Figure 3.6.** TaFISA aligned nanotubes deposited uniformly across a 10 cm wide $SiO_2$/Si wafer piece. (a) Raman spectroscopy maps of the relative nanotube density overlaid on an optical image of the sample. The ink in injected at position (i), and the flow is fully developed between regions (ii) and (iii). (b) Histogram of the relative density from the maps between positions (ii) and (iii) on the substrate. (c) SEM images of the aligned carbon nanotube film from approximate areas indicated across the sample. The scalebar in the right SEM image is 500 nm and applies to all SEM images in panel c.

### 3.3 Conclusion.

These results demonstrate that carbon nanotubes can collect and confine at a two-dimensional liquid/liquid interface, self-organize via liquid crystal phenomena, and globally align with flow. The nanotube assemblies can be deposited onto substrates to create wafer-scale arrays with exceptional local

alignment (±5.7°). The high degree of local order (**Fig. 3.1d**) and birefringence (**Fig. 3.2g**) obtained without flow and without an external driving force to induce alignment; the strong dependence of ordering on concentration and temperature; and the observation of liquid crystal defects – all confirm the underlying role of liquid crystal phenomena in TaFISA. Moreover, the importance of the two-dimensional liquid/liquid interface is evidenced by the excellent ordering obtained at nanotube ink concentrations much lower than bulk liquid crystal phase concentrations. Practically, the global alignment and uniformity improve with increasing flow rate up to 4 mL $min^{-1}$, increasing nanotube ink concentration up to 100 µg $mL^{-1}$, and decreasing temperature. The high degree of alignment and array uniformity lead to high on-state current densities averaging 520 µA $µm^{-1}$ at –0.6 V and FET to FET variation of only 19%.

The exploitation of TaFISA in future industrial processes will be facilitated by its continuous nature; although, full wafer coverage and more defect-free assembly will be needed. Full wafer coverage (as opposed to majority wafer coverage in **Fig. 3.6**) should be viable by using wafer holders that allow the ink flow to fully develop prior to crossing the substrate and that control water meniscus curvature to avoid end-effects. At the same time, implementing the process in a cleanroom environment; taking measures to eliminate spurious particles and contaminants from the nanotube ink and aqueous subphase; and, creating nanotube inks with more homogenous nanotube populations that are free of short nanotube fragments and large nanotube aggregates (that can seed and stabilize liquid crystal defects[72,82,83]) – are all expected to yield more uniform, defect-free assemblies. Engineering the polymer wrapper to suppress the formation of problematic nanotube aggregates, even at concentrations greater than 100 µg $mL^{-1}$, also has the potential to increase ordering while providing a route to higher nanotube packing densities. Further *in situ* studies of nanotube collection and ordering at the ink/water interface using interface sensitive and polarization dependent spectroscopies could shed light on the thermodynamics and kinetics of nanotube assembly at the two-dimensional liquid/liquid interface and enable a deeper understanding of this powerful alignment phenomenon.

### 3.4 Materials and methods.

**3.4.1 Preparation of PFO-BPy wrapped semiconducting carbon nanotubes.** Semiconducting carbon nanotubes are isolated from arc-discharge nanotube soot (Sigma-Aldrich, #698695) using a mass ratio (1:1) of the raw soot to polyfluorene derivative polymer wrapper, poly[(9,9-dioctylfluorenyl-2,7-diyl)-*alt*-*co*-(6,6'-{2,2'-bipyridine})] (PFO-BPy) (American Dye Source, Inc., Quebec, Canada; #ADS153-UV). The PFO-BPy is first dispersed in toluene at a concentration of 2 mg $mL^{-1}$ and is then combined with the nanotube soot and sonicated at 40% amplitude for 10 – 30 min using a horn-tip sonicator (Fisher Scientific, Waltham, MA; Sonic Dismembrator 500). This solution is centrifuged (Sorvall WX, TH-641, Thermo-Scientific) at $3 \times 10^5$ g for 10 min to remove undispersed nanotubes and other amorphous carbon allotropes. The top 90% of the supernatant of each centrifuge tube is collected and filtered. The filtered supernatants are concentrated to a total volume of 60 mL using a rotary evaporator. This concentrated solution is centrifuged for 12 – 24 h. The pellets are collected and then redispersed with fresh toluene. This centrifugation/redispersion process is repeated until the PFO-BPy:nanotube ratio is near 0.5:1 (4 – 10 repetitions). For the TaFISA alignment process, the pellets are then dispersed in chloroform (stabilized with ethanol from Fisher Scientific, #C606SK-1), and the concentration is measured optically. The nanotube concentration in solution is determined using known optical cross-sections from the $S_{22}$ transition.[22,88]

**3.4.2 Preparation of substrates.** Highly p-type doped Si wafers with 90 nm or 15 nm of dry, thermal oxide are used. The substrates are cleaned with a piranha solution with a volume ratio (2:1) of $H_2SO_4$ (91 – 92.5%):$H_2O_2$ (30%) in a crystallizing dish on a 110 °C hot plate for 15 min (for 15 nm oxide) or 60 min (for 90 nm oxide), rinsed with deionized water, and dried with $N_2$. These piranha cleaned wafers are baked for 335 s at 205 °C and exposed to hexamethyldisilizane (HMDS) vapor (Solitec VBS200 HMDS prime oven) for 2-10s to achieve a water contact angle of 30-45°.

**3.4.3 Fabrication of carbon nanotube FETs.** After deposition of nanotubes on 15 nm $SiO_2$/Si substrates, 2 wt% polymethyl methacrylate (PMMA) is spuncoat at 3k rpm for 90 s and then baked on a hot plate set at 185 °C for 90 s. Electron-beam lithography is used to define the active channel areas (channel width = 4

μm), and the substrates are developed in 2:1 ratio of methyl isobutyl ketone to isopropyl alcohol (MIBK:IPA) by volume. Following a reactive ion etch (RIE) to remove the nanotubes surrounding the active channel areas, the films are boiled in toluene to remove excess PFO-BPy and vacuum annealed to decompose the PFO-BPy and remove the alkyl side-chains of the PFO-BPy. Next, source and drain electrodes with channel length of 100 nm are fabricated within the isolated regions of nanotubes via electron-beam lithography, development, and thermal deposition of 17.5 nm of Pd and 17.5 nm of Au. A back-gate architecture is used to electrostatically control the FETs, with the 15 nm $SiO_2$ and Si substrate serving as the gate dielectric and gate electrode, respectively. One advantage of this back-gate architecture is that it facilitates correlation between array morphology (via SEM) and electrical characteristics. While the relatively low capacitance of the 15 nm $SiO_2$ back-gate challenges optimization of transconductance and subthreshold swing, these parameters can be largely improved by using thinner, top-gate dielectrics that increase the gate-channel capacitance[89] as opposed to improving nanotube alignment and ordering. The FETs exhibit hysteresis (**Fig. B8**) as expected for FETs measured in air, which has been previously attributed to adsorbed water and oxygen and/or charge traps in the oxide. **Fig. 3.5** presents forward sweeps; both forward and backward sweeps are shown in **Fig. B8**.

**3.4.4 Raman spectroscopy.** Raman spectroscopy (Thermo-Fisher Scientific, DXR-XI, 532 nm excitation laser wavelength) is used to map carbon nanotube density. The intensity of the G-band Raman mode is directly related to the density of carbon nanotubes on the substrate (assuming a spatially uniform chirality distribution).[30] Prior to Raman measurement, the carbon nanotube films are soaked in toluene at 110 °C for 1 h and then vacuum annealed at 400 °C for 1 h . A full Raman spectrum is collected at each pixel of the map, and the nanotube density is quantified by spectrally integrating over the G-band mode.

**3.4.5 Experimental conditions for each figure.** The TaFISA process is conducted using a channel, comprised of a target substrate and a sacrificial barrier, that is attached to a substrate lift motor (Thorlabs MTS50-Z8) and suspended in a trough filled with deionized (resistivity ~18 MΩ) water. The ink is injected into the channel using a needle, and the ink volumetric flow rate is controlled using a syringe pump

(Chemyx Nexus 3000). In addition to the ink flow rate, ink concentration, and temperature (discussed more in the main text), other experimental parameters that can be varied include: type of needle used to inject the ink, substrate channel lift rate, substrate channel angle, needle angle, and the position of the needle within the channel. In this work, the channel is oriented 45° from the horizontal surface of the water—we found positioning the channel at this angle resulted in more uniform deposition across the length of the substrate. In this angled channel, the upper half of the channel is the target substrate and has aligned nanotube films deposited on it, while the lower half is the sacrificial barrier, which has thicker films of primarily poorly aligned nanotubes deposited onto it. The needle is angled 15° from the horizontal, just slightly touching the surface of the water, and roughly centered between the target substrate and sacrificial barrier.

**Figure 3.1**: The ink volumetric flow rates for the TaFISA aligned films are 0 and 4 mL $min^{-1}$. The ink needle used is polyether ether ketone (PEEK), with outer diameter 1.59 mm and inner diameter 0.76 mm. The lift rate is 26 mm $min^{-1}$. The substrate is vertical for the 0 mL $min^{-1}$ sample, and the substrate channel is oriented at 45° for the 4 mL $min^{-1}$ sample. The ink concentration is 100 µg $mL^{-1}$. For the FESA sample, the substrate lift rate is 5 mm $min^{-1}$. The ink volumetric flow rate is 0.175 mL $min^{-1}$. The ink concentration is 30 µg $mL^{-1}$. All substrates used in this figure are 90 nm $SiO_2$ on highly p-type doped Si.

**Figure 3.2**: The ink volumetric flow rate is 0, 1, and 4 mL $min^{-1}$. The ink needle is PEEK. The lift rate is 26 mm $min^{-1}$. The substrate channel is oriented at 45°. The ink concentration is 100 µg $mL^{-1}$. All substrates used in this figure are 90 nm $SiO_2$ on highly p-type doped Si.

**Figure 3.3**: The ink needle used is a polytetrafluoroethylene (PTFE) coated steel needle (23 ga). The ink volumetric flow rate is 4 mL $min^{-1}$. The lift rate is 160 mm $min^{-1}$. The substrate channel is oriented at 45°. All substrates used in this figure are 90 nm $SiO_2$ on highly p-type doped Si.

**Figure 3.4**: The ink needle used is a PTFE coated steel needle (23 ga). The ink volumetric flow rate is 4 mL $min^{-1}$. The lift rate is 160 mm $min^{-1}$. The ink concentration is 100 µg $mL^{-1}$. The substrate channel is oriented at 45°. The 35 °C sample was obtained by heating the water trough on a hotplate and the 10 °C

data point was obtained by placing the water trough in an ice bath. All substrates used in this figure are 90 nm $SiO_2$ on highly p-type doped Si.

**Figure 3.5**: For the TaFISA sample, the volumetric flow rate is 4 mL $min^{-1}$. The ink needle used is a PTFE coated steel needle (23 ga). The substrate lift rate is 40 mm $min^{-1}$. The substrate channel is oriented at 45°. The ink concentration is 150 µg $mL^{-1}$. For the FESA sample, the substrate lift rate is 5 mm $min^{-1}$. The ink volumetric flow rate is 0.175 mL $min^{-1}$. The ink concentration is 30 µg $mL^{-1}$. All substrates used in this figure are 15 nm $SiO_2$ on highly p-type doped Si.

**Figure 3.6**: The ink needle used is a PTFE coated steel needle (23 ga). The substrate is a 10 cm wide 90 nm $SiO_2$/Si wafer and the volumetric flow rate is 8 mL $min^{-1}$. The substrate lift rate is 160 mm $min^{-1}$. The ink concentration used is 100 µg $mL^{-1}$. The substrate channel is oriented at 45°.

# **Chapter 4.** Parameters affecting interfacial assembly and alignment of nanotubes

Chapter 4 was adapted from Jinkins, K. R., Dwyer, J. H., Suresh, A., Gopalan, P., & Arnold, M. S. Parameters Affecting Interfacial Assembly and Alignment of Nanotubes. *In preparation*. (2020). K.R.J. and M.S.A. performed all experiments, data collection, and analysis. J.H.D., A.S., and P.G. prepared self-assembled monolayer and polymer surfaces and measured water contact angles in **Fig. 4.3c,e-h**. J.H.D. and P.G. suggested the addition of glycerol to the water subphase (**Fig. 4.4**). M.S.A. and P.G. supervised all experiments. K.R.J. drafted the manuscript.

**Abstract:** Tangential flow interfacial self-assembly (TaFISA) is a promising scalable technique for uniformly aligning carbon nanotubes for high-performance semiconductor electronics. In this process, flow is utilized to induce global alignment in two-dimensional nematic carbon nanotube assemblies trapped at a liquid/liquid interface, and these assemblies are subsequently deposited on target substrates. Here, we present a detailed study of experimental parameters that affect the interfacial assembly as well as the subsequent aligned nanotube deposition. We study the effect of the nanotube ink composition, water contact angle of the substrate, and water subphase. We find that the best alignment occurs when the nanotubes are dispersed in chloroform at a low (0.6:1) wrapper polymer to nanotube ratio. By varying the substrate chemical functionalization, we determine that highly aligned, densely packed nanotubes deposit only at relatively small water contact angles between 35° and 65°. We also demonstrate that modifying the water subphase through the addition of glycerol improves overall alignment and reduces defects, but also increases local nanotube aggregation. These results provide key insight into the TaFISA mechanism and enable a promising path towards technologies based on semiconducting carbon nanotubes.

## 4.1 Introduction.

As discussed in detail in Chapter 3, recently, we developed a particularly promising approach—tangential flow interfacial self-assembly (TaFISA)—which results in deposition of highly aligned nanotube arrays (within ±5.7°) across 10 cm substrates.[90] In this process, an ink of polymer-wrapped nanotubes in organic solvent is flowed through an open channel comprised of a target substrate and sacrificial barrier suspended in a water subphase. By translating the substrate and sacrificial barrier together through the flowing ink/water interface, uniform films of highly aligned nanotubes are fabricated. The high array uniformity translates to excellent FET characteristics and reproducibility with high on-state current density averaging 520 μA $\mu m^{-1}$ at –0.6 V and FET to FET variation of only 19%.

In this initial work,[90] we determined that the nanotubes collect at the two-dimensional ink/water interface and the additional confinement at this interface leads to liquid crystal assembly. Due to the underlying liquid crystal phenomena guiding the alignment, increasing ink flow rate, increasing concentration, and decreasing temperature were demonstrated to improve the nanotube alignment. These initial results were exciting; however, this work primarily focused on elucidating the TaFISA mechanism and demonstrating that the aligned nanotube arrays are promising for industrial semiconductor electronics. In this chapter, we present a more in-depth study on the effect of deposition parameters, including the nanotube ink, the substrate, and the water subphase, on the interfacial assembly and alignment of the nanotubes from the liquid/liquid interfaces.

## 4.2 Results and discussion.

**4.2.1 Effect of solvent and wrapping polymer on TaFISA alignment.** First, we study the effect of nanotube ink solvent on TaFISA alignment (**Fig. 4.1**). Scanning electron microscopy (SEM) images of nanotube arrays aligned via TaFISA using chloroform, toluene, and 1,2-orthodichlorobenzene (ODCB) are shown in **Fig. 4.1a-c**, respectively. The chloroform and toluene inks are comprised of arc-discharge

semiconducting carbon nanotubes isolated with poly[(9,9-dioctylfluorenyl-2,7-diyl)-*alt*-*co*-(6,6'-{2,2'-bipyridine})] (PFO-BPy), while the ODCB ink is comprised of (7,5)-enriched nanotubes isolated with poly[(9,9-dioctylfluorenyl-2,7-diyl) (PFO) from as-produced cobalt molybdenum catalysis of carbon monoxide disproportionation (CoMoCAT) powder. Regardless of the solvent (chloroform, toluene, and ODCB), polymer wrapper (PFO and PFO-BPy), and nanotube production method (arc-discharge and CoMoCAT), all ink solvents result in highly aligned nanotube arrays, characteristic of the two-dimensional interfacial assembly of TaFISA. This indicates that the interfacial assembly is not restricted to the PFO-BPy wrapped arc-discharge nanotubes in chloroform used in our previous work, and can be adapted to different combinations of solvents and polymer wrappers, and to nanotubes produced via different methods. However, as observed, the toluene and ODCB inks result in more waviness and nanotube aggregation within the aligned films as compared to the chloroform ink. Videos of the depositions show that both the toluene and ODCB ink layers are thicker and less well defined than the chloroform ink layer at the same ink flow rate and channel width (**Fig. C1**); thus, this lower degree of alignment is likely partly caused by lower effective shear rates in the channel. Additionally, within the ODCB ink, the smaller diameter (7,5) nanotubes (diameter of 0.82 nm) are less stiff and will be more difficult to align than arc-discharge nanotubes (diameter ~1.5 nm). The low solubility of nanotubes within the toluene ink is also an additional cause of bundling and aggregation within that film. For the remainder of this chapter, we use PFO-BPy wrapped arc-discharge nanotubes dispersed in chloroform ink.

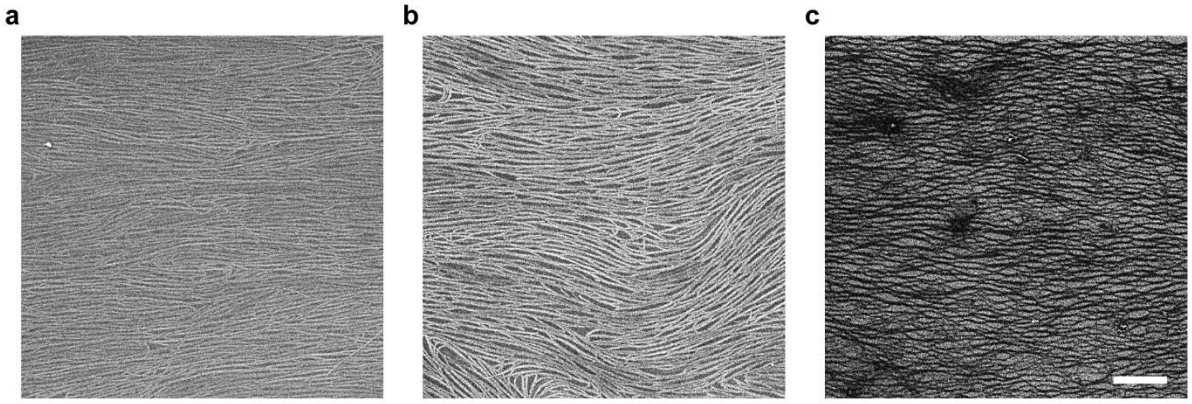


**Figure 4.1.** Effect of nanotube ink solvent on TaFISA aligned nanotube arrays. (a-c) SEM images from TaFISA films obtained using nanotube inks with (a) chloroform, (b) toluene, and (c) ODCB as the organic solvent. The scalebar in (c) is 500 nm and applies to (a-c).

**4.2.2 Effect of PFO-BPy wrapping polymer to nanotube ratio.** Because the TaFISA process relies on interfacial adsorption of nanotubes at the ink/water interface, we expect that the amount of free polymer in solution will affect the alignment and morphology of the resulting nanotube films. Here, we show that decreasing the PFO-BPY:nanotube ratio results in more uniform nanotube films (**Fig. 4.2**). This trend is qualitatively observed from polarized optical microscopy (POM) images at three different PFO-BPy:nanotube ratios, where brighter yellow indicates the nanotubes are aligned with the flow direction (horizontal), and darker regions correspond to nanotubes misaligned from the direction of flow. At a high PFO-BPy:nanotube ratio of 3.7:1, the POM image exhibits some bright yellow regions, however, a large portion of the image shows dark regions, where the nanotube alignment is changing direction. At a ratio of 1:1, the darker defective regions where the alignment is changing direction become smaller and at an even lower ratio of 0.6:1, the film is almost uniformly yellow, indicating the majority of the nanotubes are aligned with the direction of flow. The small dark regions observed in (c) are small deviations in alignment and have been correlated primarily to liquid crystal defects due to the underlying role of liquid crystal assembly on alignment. The effect of the PFO-BPy:nanotube ratio is also seen on a more local scale in SEM images (d-f). With decreasing PFO-BPy:nanotube ratio, the nanotube alignment becomes more oriented with the direction of flow, consistent with the POM data. Additionally, at high polymer ratios, more black ‘spots’

are seen on the film, which correspond to free PFO-BPy (i.e., polymer that is not wrapping a nanotube, but instead is free in solution) that deposits from solution along with the nanotubes and can be removed via boiling in toluene (shown in **Fig. C2**). The amount of free polymer deposited on the nanotube films decreases with decreasing PFO-BPy:nanotube ratio. These results indicate that to achieve uniform films of highly aligned nanotubes from the TaFISA technique, a low polymer to nanotube ratio must be used. However, if the PFO-BPy:nanotube ratio is too low, the nanotubes come out of solution and form aggregates, so likely there is an intermediate range of ideal PFO-BPy:nanotube concentrations.

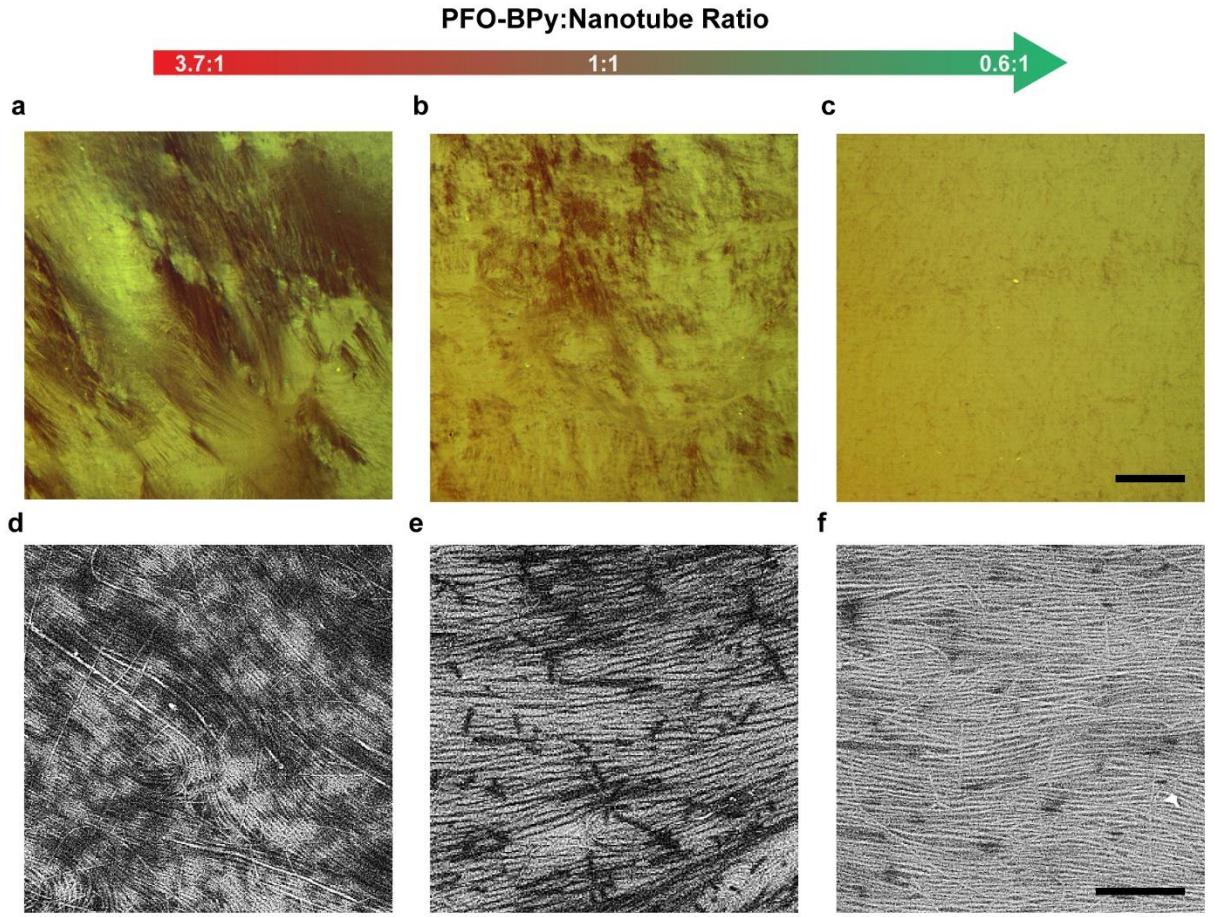


**Figure 4.2.** Effect of PFO-BPy to nanotube ratio on nanotube arrays aligned via TaFISA. (a-c) POM images from TaFISA films fabricated using nanotube ink with PFO-BPy:nanotube ratios of 3.71:1, 1:1, and 0.6:1, respectively. Scalebar in (c) is 250 μm and applies to (a-c). (d-f) SEM images of TaFISA films shown in (a-c), respectively. Scalebar in (f) is 500 nm and applies to (d-f).

**4.2.3 Effect of surface chemical functionalization and water contact angle.** Next, we study the effect of chemical functionalization of the substrate surface on the nanotube deposition. Chemical functionalization of the surface leads to variation in water contact angle (WCA), which can affect the assembly of nanotube films aligned via TaFISA in multiple ways. For example, the nanotubes must be able to deposit and adhere to the substrate. Previous work has demonstrated that deposited nanotube density is dependent upon solvent structuring at the substrate, affected by both the chemical functionalization of the target substrate and the nanotube ink solvent.[91] Additionally, because the TaFISA process relies on a well-formed and controllable ink/water interface at the substrate, we expect that the WCA itself will also have a role in deposition. For example, if the WCA is too small (i.e., hydrophilic), the ink will not be able to dewet the water from the substrate and the ink/water interface will not form at the substrate—this would prevent highly ordered nanotubes from depositing from the 2D nematic assembly at the liquid/liquid interface.

To study the effect of WCA on nanotube deposition, surfaces coated with eight different self-assembled monolayers and polymers are investigated, in which the WCA ranges from less than 10° to 112° (**Fig. 4.3**). The optimal nanotube alignment is observed on substrates with partial coverage of hexamethyldisilazane (HMDS) (to be confirmed with AFM) and corresponding WCA of 35° (**Fig. 4.3b**) and with 3-aminopropyltriethoxysilane (APTES) and corresponding WCA of 40° (**Fig. 4.3c**). These two substrates exhibit very similar nanotube alignment and nanotube packing densities, despite the difference in functional head group termination (methyl versus amine).

When the WCA is below (WCA < 10°) or above (WCA > 65°) this optimal range of 30 – 40°, the nanotube alignment and/or uniformity are worse. For example, when the substrate surface is too hydrophilic (WCA < 10°), which is achieved by functionalizing the surface with hydroxyl groups via piranha treatment, the nanotubes deposit as thick ropes. Deposition of thick ropes likely occurs because the water subphase does not dewet from the substrate, inhibiting formation of an ink/water interface at the substrate and subsequent nanotube deposition from this interface. In contrast, when the WCA is too hydrophobic, several different phenomena are observed. When the WCA is 65°, the deposition results in intermittent regions of

highly aligned nanotubes (**Fig. 4.3d**), due to the ink/water interface stick-slipping across the substrate and not pinning for enough time to deposit a uniform nanotube film. At higher WCAs between 72° and 90° (**Fig. 4.3e-g**), only random nanotubes of various densities are deposited on the substrate, in which case deposition likely occurs from the bulk of the nanotube ink. At an even higher WCA of 112° on a surface terminated with octadecyltrichlorosilane (OTS), nanotubes are not deposited. We hypothesize that the lack of aligned nanotube deposition at WCAs greater than 65° is due to the ink/water contact line not being able to controllably form and pin at the substrate for enough time to allow nanotube deposition from the interface. This hypothesis could be investigated with back-imaging experiments. The density dependence observed in **Fig. 4.3e-h** can possible be attributed to varying nanotube adhesion to the substrate as a result of different solvent structuring, as demonstrated by Dwyer et al.[91]

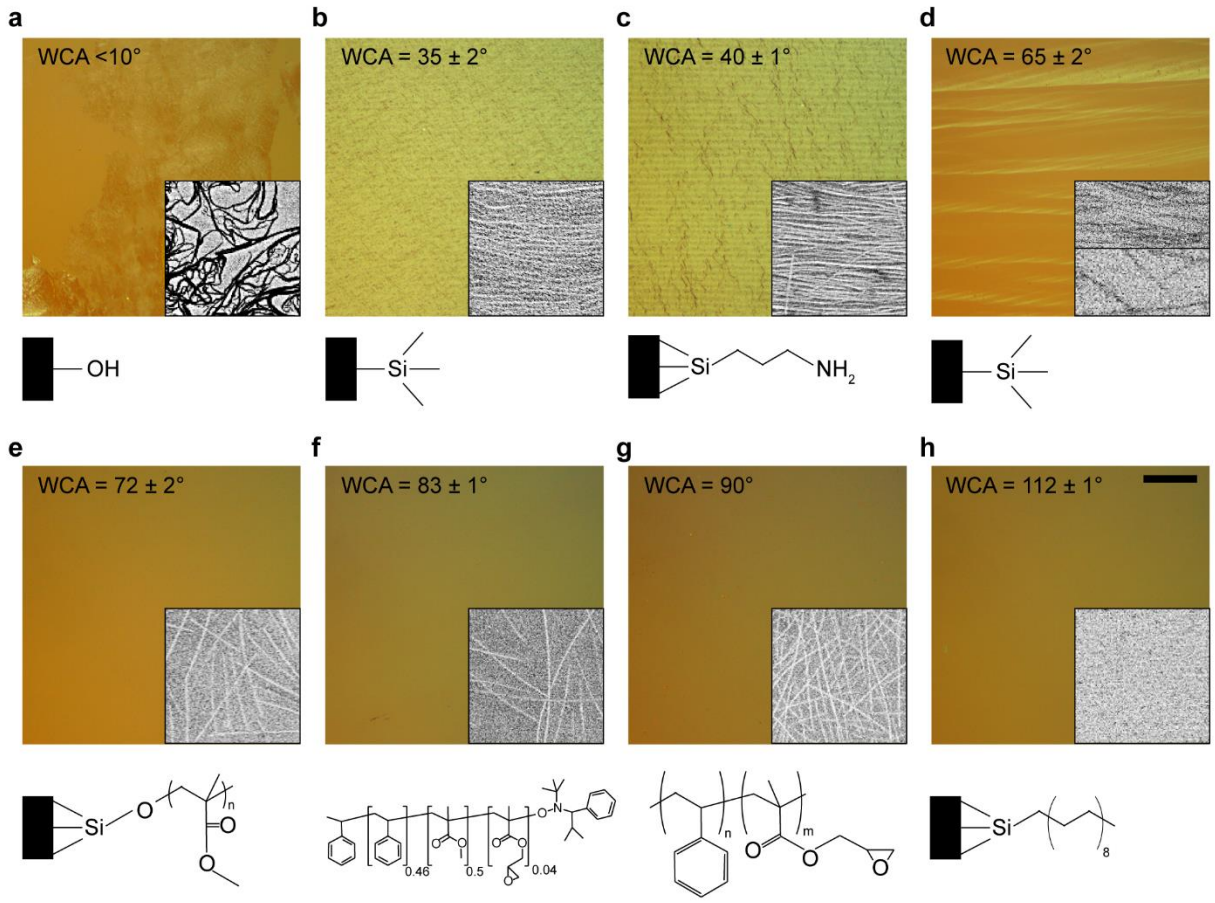

**Figure 4.3.** Effect of chemical functionalization of the substrate surface and WCA on nanotube arrays aligned via TaFISA. (a-h) POM and SEM images (inserts) of nanotube arrays on surfaces coated with hydroxyl groups (from piranha treatment) (a), partial HMDS coverage (b), APTES (c), full HMDS coverage (d), surface grafted poly(styrene-*rand*-methyl methacrylate) (PS-PMMA) (e), poly(styrene-*rand*-methyl methacrylate-*rand*-glycidyl methacrylate) (PG4-46) (f), poly(styrene-*rand*-glycidyl methacrylate) (PS-GMA) (g), and OTS (h). Chemical structures of each surface are shown below each respective POM image. The SEM insets are $1 \times 1$ μm$^2$ in (b-h) and $10 \times 10$ μm$^2$ in (a).

**4.2.4 Effect of water subphase modification.** Formation of a stable, well-defined ink/water interface is paramount for collecting and confining the nanotubes into nematic assemblies and aligning the nanotubes with flow. With the goal of obtaining a more controllable ink/water interface, we studied the effect of an additive, glycerol, with high viscosity to the water subphase (**Fig. 4.4**). POM images from TaFISA depositions using subphases consisting of 100% water (**Fig. 4.4a**), 20% glycerol / 80% water (by volume) (**Fig. 4.4b**), and 40% glycerol / 60% water (by volume) (**Fig. 4.4c**) are shown at a volumetric flow rate of 1 mL min$^{-1}$. With the addition of 20% glycerol to the water subphase, the nanotube film is exceptionally uniform and almost defect-free (**Fig. 4.4b**), however with the addition of 40% glycerol, the overall alignment (and possibly density) of nanotubes deposited decreases as evidenced by the darker color POM (**Fig. 4.4c**). This high degree of alignment and uniformity with an intermediate amount of glycerol added to the water subphase is promising; however, comparison of the SEM insets from depositions (**Fig. 4.4a-c**) shows that the addition of glycerol increases the nanotube bundling and aggregation. So, while there are fewer defects in the film, these bundled nanotubes are not suitable for high-performance devices. Future work will focus on taking advantage of subphase modification to increase nanotube alignment and uniformity, while also preventing nanotube aggregation.

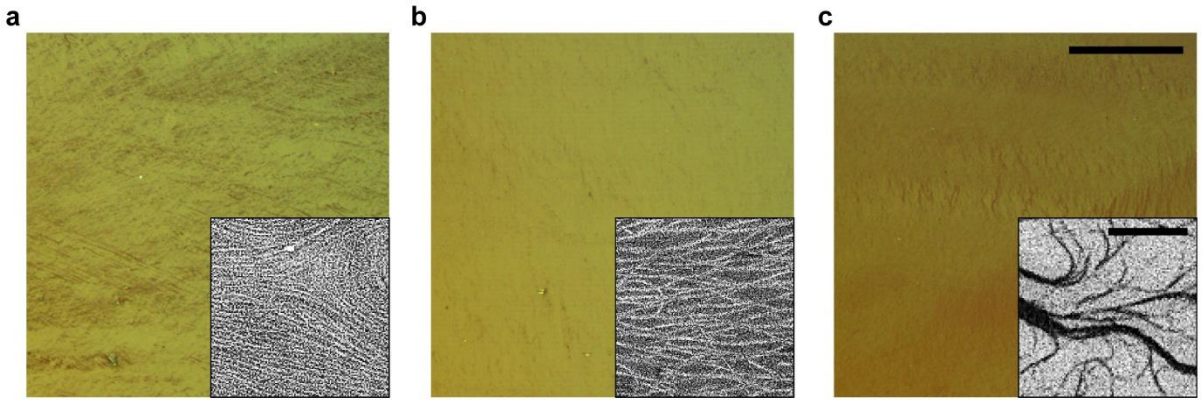


**Figure 4.4.** Effect of glycerol in the water subphase on nanotube films aligned via TaFISA. POM and SEM (inset) images of nanotube films obtained using all water subphase (a), a subphase of 20 vol% glycerol and 80 vol% water (b), and a subphase of 40 vol% glycerol and 60 vol% water at a flow rate of 1 mL $min^{-1}$. Scalebars in (c) are 250 µm (POM image) and 500 nm (SEM image) and applies to (a-c).

We also investigate the effect of ethanol in the water subphase to study how decreasing the subphase surface tension affects TaFISA alignment. Additionally, through previous work, we have determined that the ethanol stabilizer (as opposed to the amylene stabilizer) in chloroform is vital to achieve alignment in FESA films. With 1 vol% ethanol in the water subphase (**Fig. 4.5b**), the nanotube films are very similar to films obtained with a 100% water subphase (**Fig. 4.5a**). However, with 4.7 vol% ethanol in the water subphase, nanotubes are not deposited onto the substrate (**Fig. 4.5c**). While the videos of these depositions with different ethanol concentrations look similar, at 4.7% ethanol, we hypothesize that the surface tension of the water is sufficiently decreased so that the ink/water interface does not form and the nanotube ink diffuses more quickly into the ethanol/water mixture.

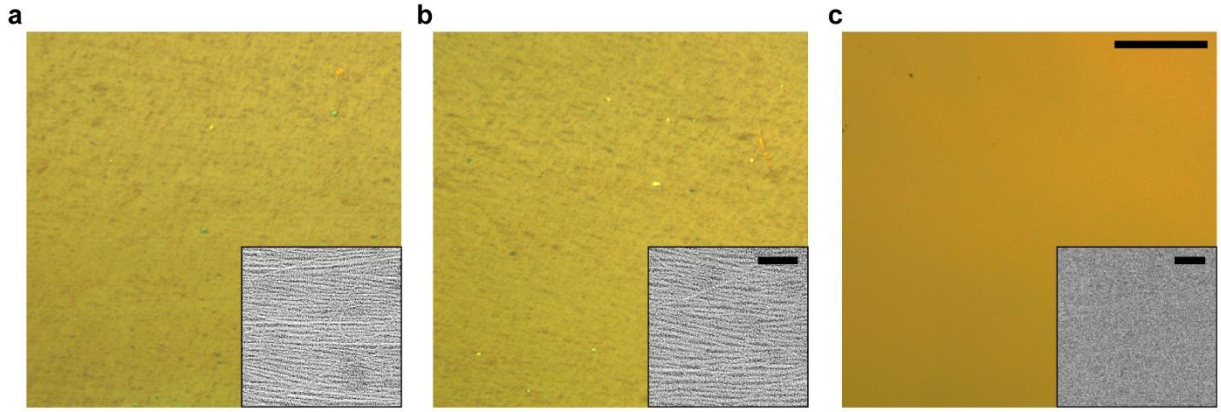


**Figure 4.5.** Effect of ethanol in the water subphase. (a-c) POM and SEM (inset) images obtained from TaFISA depositions with 0, 1, and 4.7 vol% ethanol in the water subphase, respectively. The large scalebar in (c) is 200 µm and applies to POM images in (a-c). The scalebar in the SEM inset in (b) is 250 nm and applies to (a) and (b). The scalebar in the SEM inset in (c) is 1 µm.

### 4.3 Conclusion.

In this work, we perform more detailed studies into experimental parameters that directly affect the interfacial assembly and alignment of carbon nanotubes in the TaFISA process. We find that the interfacial assembly of carbon nanotubes occurs for at least two types of carbon nanotubes and polymer wrappers—arc-discharge and (7,5)-enriched nanotubes from CoMoCAT process, wrapped with PFO-BPy and PFO, respectively. We optimize the PFO-BPy:nanotube ratio to obtain highly aligned nanotube films at a 0.6:1 ratio. Furthermore, we identify the window of substrate WCA over which optimum carbon nanotube alignment occurs. Modification of the water subphase is studied through the addition of glycerol and ethanol. The alignment on a glycerol/water subphase is promising for future investigations due to the high film uniformity and alignment, especially if used in conjunction with a polymer wrapper that more strongly prevents bundling of nanotubes. Additionally, future work would also need to be performed to determine if glycerol residues remain on the nanotubes and how the residues affect device performance. This work demonstrates important progress toward understanding the parameter space that affects the liquid/liquid interfacial assembly of nanotubes.

## 4.4 Materials and methods.

**4.4.1 Isolation of semiconducting carbon nanotubes using PFO-BPy.** Semiconducting carbon nanotubes are isolated according to our previously published procedures[90] from arc-discharge nanotube soot (Sigma-Aldrich, #698695) using a (1:1) of raw soot to polyfluorene derivative polymer wrapper, poly[(9,9-dioctylfluorenyl-2,7-diyl)-*alt*-*co*-(6,6'-{2,2'-bipyridine})] (PFO-BPy) (American Dye Source, Inc., Quebec, Canada; #ADS153-UV). Briefly, the PFO-BPy is dispersed in toluene and this mixture is combined with the nanotube powder at a concentration of 2 mg $mL^{-1}$ and sonicated at 40% amplitude for 30 min using a horn-tip sonicator. The solution is then centrifuged to remove unselected nanotubes and other amorphous carbon species. The supernatant is collected and the excess PFO-BPy is removed through subsequent centrifugation and sonication steps until the desired PFO-BPy:nanotube ratio is achieved (3-10 repetitions). The nanotube concentration in the final ink solutions is determined using known optical cross-sections from the $S_{22}$ transition.[22,88]

**4.4.2 Preparation of PFO-wrapped (7,5)-enriched semiconducting carbon nanotubes.** (7,5)-enriched semiconducting carbon nanotubes are extracted from a CoMoCAT produced small diameter (0.7-1.2 nm) nanotube powder (Southwest Nanotechnologies) using poly(9,9-dioctylfluorene-2,7-diyl) (PFO) following our previously published procedure.[92,93] Briefly, PFO in toluene is combined with CoMoCAT nanotubes (1:0.5 mass ratio) through horn-tip sonication and centrifuged to remove nanotubes not wrapped with the PFO. The excess PFO in the highly pure semiconducting nanotube solution is then removed through subsequent centrifugation and sonication steps to achieve a PFO:nanotube ratio near 1:1.

**4.4.3 Preparation of substrates.** Si wafers with 90 nm of dry, thermal oxide or native oxide are used in this chapter. The substrates are cleaned with a piranha solution of $H_2SO_4$ (91 – 92.5%):$H_2O_2$ (30%) at a ratio of 2:1 by volume at 110 °C for 1 h, rinsed with deionized water (resistivity ~18 MΩ), and dried with $N_2$. All substrates except those in **Fig. 4.3** were then baked for 335 s at 205 °C and exposed to 2 s of HMDS vapor.

### 4.4.4 Experimental parameters for each figure.

**Figure 4.1**: The ink needle used is a steel needle (23 ga). The ink volumetric flow rate is 0.35 mL $min^{-1}$. The lift rate is 7 mm $min^{-1}$. The ink concentration is 30 µg $mL^{-1}$. The substrate channel is oriented at 90°. All substrates used in this figure are 90 nm $SiO_2$ on highly p-type doped Si.

**Figure 4.2**: The ink needle used is a polytetrafluoroethylene (PTFE) coated steel needle (23 ga). The ink volumetric flow rate is 4 mL $min^{-1}$. The lift rate is 40 mm $min^{-1}$. The ink concentration is 100 µg $mL^{-1}$. The substrate channel is oriented at 45°. All substrates used in this figure are 90 nm $SiO_2$ on highly p-type doped Si.

**Figure 4.3**: The ink needle used is a PTFE coated steel needle (23 ga). The ink volumetric flow rate is 4 mL $min^{-1}$. The lift rate is 20 mm $min^{-1}$. The ink concentration is 100 µg $mL^{-1}$. The substrate channel is oriented at 45°.

Specific surface treatments (to be confirmed and added) in addition to piranha treatment discussed earlier:

(b) Baked at 205 °C for 335 s and then exposed to HMDS vapor for 2 s.

(c) APTES-functionalized surfaces were fabricated following previously published procedure.[91]

(d) Baked at 205 °C for 335 s and then exposed to HMDS vapor for 15 s.

(e) PS-PMMA functionalized surface prepared according to previously published procedure.

(f) PG4-46 copolymer mat surface was prepared according to previously published procedure.[94]

(g) PS-GMA surface prepared according to previously published procedure.

(h) OTS-functionalized surfaces were fabricated following previously published procedure.[91]

**Figure 4.4**: The ink needle used is a PTFE coated steel needle (23 ga). The ink volumetric flow rate is 1 mL $min^{-1}$. The lift rate is 80 mm $min^{-1}$. The ink concentration is 100 µg $mL^{-1}$. The substrate channel is oriented at 45°. All substrates used in this figure are 90 nm $SiO_2$ on highly p-type doped Si.

**Figure 4.5**: The ink needle used is a PTFE coated steel needle (23 ga). The ink volumetric flow rate is 4 mL $min^{-1}$. The lift rate is 100 mm $min^{-1}$. The ink concentration is 100 µg $mL^{-1}$. The substrate channel is oriented at 45°. All substrates used in this figure are 90 nm $SiO_2$ on highly p-type doped Si.

# **Chapter 5.** Substrate-wide confined shear alignment of carbon nanotubes for thin film transistors

Chapter 5 was adapted with permission from Jinkins, K. R., Chan, J., Jacobberger, R. M., Berson, A., & Arnold, M. S. Substrate-Wide Confined Shear Alignment of Carbon Nanotubes for Thin Film Transistors. *Adv. Electron. Mater.* **5**, 1800593 (2019). Copyright (2018) WILEY-VCH. K.R.J. and M.S.A. performed all experiments, data collection, and analysis. K.R.J. designed and fabricated the standard confined shear-based alignment apparatus. J.C. fabricated the larger experimental apparatus for depositing aligned nanotubes across 10 cm substrates (used in **Fig. 5.5**) and R.M.J. measured the interior roughness of these shear alignment setups with interferometry. M.S.A. and A.B. supervised the work. All authors contributed to data interpretation. K.R.J. drafted the manuscript, and all authors discussed and revised it.

**Abstract**: To exploit their exceptional charge transport properties in transistors, semiconducting carbon nanotubes must be assembled onto substrates in aligned arrays comprised of individualized nanotubes at optimal packing densities. However, achieving this control on the wafer-scale is challenging. Here, we investigate solution-based shear in substrate-wide, confined channels to deposit continuous films of well-aligned, individualized, semiconducting nanotubes. Polymer-wrapped nanotubes in organic ink are forced through sub-mm tall channels, generating shear up to 10,000 $s^{-1}$ uniformly aligning nanotubes across substrates. The ink volume and concentration, channel height, and shear rate dependencies are elucidated. Optimized conditions enable alignment within a ±27° window, at 50 nanotubes $\mu m^{-1}$, on 10×10 $cm^2$ substrates. Transistors (channel length of 1 – 5 μm) are fabricated parallel and perpendicular to the alignment. The parallel transistors perform with 7× faster charge carrier mobility (101 and 49 $cm^2V^{-1}s^{-1}$ assuming array and parallel-plate capacitance, respectively) with high on/off ratio of $10^5$. The spatial uniformity varies ±10% in density, ±2° in alignment, and ±7% in mobility. Deposition occurs within seconds per wafer, and further substrate scaling is viable. Compared to random networks, aligned nanotube

films promise to be a superior platform for applications including sensors, flexible/stretchable electronics, and light emitting and harvesting devices.

**5.1 Introduction**.

Semiconducting single-walled carbon nanotubes are widely regarded as a promising candidate for next-generation thin film transistors because of their exceptional charge transport properties,[6,7,50,51] solution-processability, mechanical resilience,[95] and air-stability. The applications of these thin film transistors include sensors, flexible electronics, and displays, to name a few. In order to fully exploit nanotubes' fast and directional charge transport properties in these applications, films of aligned, individualized, electronics-grade semiconducting nanotubes are needed. These nanotubes must be uniformly deposited over large-area substrates at an intermediate linear packing density of 50 – 200 nanotubes $\mu m^{-1}$.[2,18] Alignment is important, as it decreases the number of resistive nanotube-nanotube junctions in the charge percolation pathway, thereby enabling high transistor drive current and mobility.[16,17] However, many applications of thin film transistors utilize device architectures with the channel length is longer than the length of an average nanotube. In this case, not only is alignment important to reduce channel resistance, but also if the degree of alignment is too high, the nanotubes will cease to overlap, reducing the percolation pathways, in turn reducing the on-current. Therefore, for long channel thin film transistors quasi-aligned nanotubes are required.

In Chapters 2-4, we discussed nanotube alignment techniques that result in highly aligned, however, in this chapter, we investigate solution-based shear as a means for depositing continuous films of quasi-aligned, individualized, electronics-grade semiconducting nanotubes onto substrates at the intermediate packing density needed for thin film transistors.

Whereas microfluidic channels have been previously utilized to shear-align nanowires[96,97] and nanotubes[98,99] in solution over small areas, here, a substrate-wide deposition strategy is explored for depositing nanotubes to form a uniform, continuous film. For example, we demonstrate uniform deposition

on a 10 × 10 $cm^2$ substrate. Elements of shear have been utilized in other nanotube and nanowire alignment approaches in the past, including blown-bubble assembly,[41] spinning Langmuir method,[100] air-driven directional evaporation,[43,45,101] and bulk polymer flow.[102] However, additional effort is still required to realize large-area and uniform nanotube films with the attributes (e.g., alignment, individualization, controlled packing density, semiconducting-purity) that are needed to fully exploit nanotubes in electronics.

In general, flow-induced shear is a promising approach for aligning elongated nanostructures. Velocity gradients in a flow field induce a shear force that acts to rotate elongated nanostructures so that their long-axis points in the direction of flow – provided that the magnitude of the velocity gradient exceeds the rotational diffusion coefficient, $D_r$, of the nanostructure.[103] Smaller nanostructures have larger $D_r$, and thus, in comparison to larger nanostructures such as nanowires and multi-walled nanotubes, single-walled carbon nanotubes are particularly difficult to align via shear. For example, the $D_r$ of a typical single-walled nanotube (diameter, $d$, = 1.4 nm; length, $L$, = 0.5 μm) is ~ 310 $s^{-1}$, which is 100× larger than the $D_r$ of ~ 3 $s^{-1}$ for a conventional inorganic nanowire (diameter, $d$, = 25 nm; length, $L$, = 2 μm).[96]

Besides their larger $D_r$, another complication with depositing aligned single-walled nanotubes is maintaining their individualization. Surfactants and polymer wrappers non-covalently bind to nanotubes and are commonly used to individually disperse nanotubes into solvents. These wrappers, however, can inhibit the deposition and "sticking" of nanotubes to target substrates. Furthermore, if these species are only weakly bound to the nanotubes, the nanotubes can problematically coalesce into bundles during deposition. Residues of these surfactants and polymer wrappers can also contaminate the nanotube/electrode and nanotube/nanotube interfaces of thin film transistors, decreasing performance.[22]

**5.2 Results and discussion.**

In this work, conjugated polymer wrapped nanotubes dispersed in chloroform are used as a nanotube ink. To create the ink, semiconducting nanotubes are extracted from heterogeneous as-produced powder of nanotubes grown by the arc discharge method using the selective polymer wrapper, poly[(9,9-

dioctylfluorenyl-2,7-diyl)-*alt*-*co*-(6,6'-{2,2'-bipyridine})] (PFO-BPy).[88,104] After wrapping, unselected and/or undispersed metallic and semiconducting nanotubes are precipitated from solution via centrifugation. Excess, unbound polymer is then removed from the ink. This procedure yields inks that are well-suited for shear alignment and for thin film transistors. For example, the polymer wrapping layer is significantly more robust than small molecule surfactant wrappers, enabling more stable, individualized nanotube dispersions even when the excess polymer wrappers have been removed from solution, which is not typically the case with surfactants. In addition, the excess surfactant needed to stabilize carbon nanotubes in solution can interfere with deposition so the removal of this excess polymer from the ink is crucial for controlling adsorption of the nanotubes to the substrate and minimizing residues after deposition. Finally, conjugated polymers such as PFO-BPy are capable of reducing the relative abundance of metallic nanotubes to < 0.01%, thereby enabling the fabrication of ultrahigh purity semiconducting nanotube films largely free of problematically metallic nanotube species.[3,22] This extraction process and the preparation of substrates are discussed in more detail in the Experimental section.

The experimental apparatus used for the substrate-wide shear alignment is shown in **Fig. 5.1**. The setup consists of two stainless steel plates (each 6.35 mm thick), a bottom plate on which the substrate is placed, and a top plate with a tube fitting as an input for the semiconducting nanotube ink. The inside of the top plate is polished to a roughness of 23 ± 4 nm (measured via a Zygo interferometer). A channel mask is created to confine the flow of ink and direct it uniformly across the surface of the substrate. The mask is cut from 25.4 to 127 μm thick perfluoroalkoxy (PFA) sheet. Stainless steel spacers are placed outside the channel to act as "hard-stops" that coarsely define the channel height when the PFA is compressed to the spacers. After tightening, bolts along the outside of the plates fasten the top plate to the bottom plate and create a sealed channel. After assembly of the apparatus, the channel height is measured.

The ink is injected and forced through the substrate-wide channel using a syringe pump (Chemyx Nexus 3000), immediately followed by chloroform to "wash" any remaining nanotubes out of the channel. The channel is subsequently rinsed with isopropyl alcohol (IPA) and dried with $N_2$.

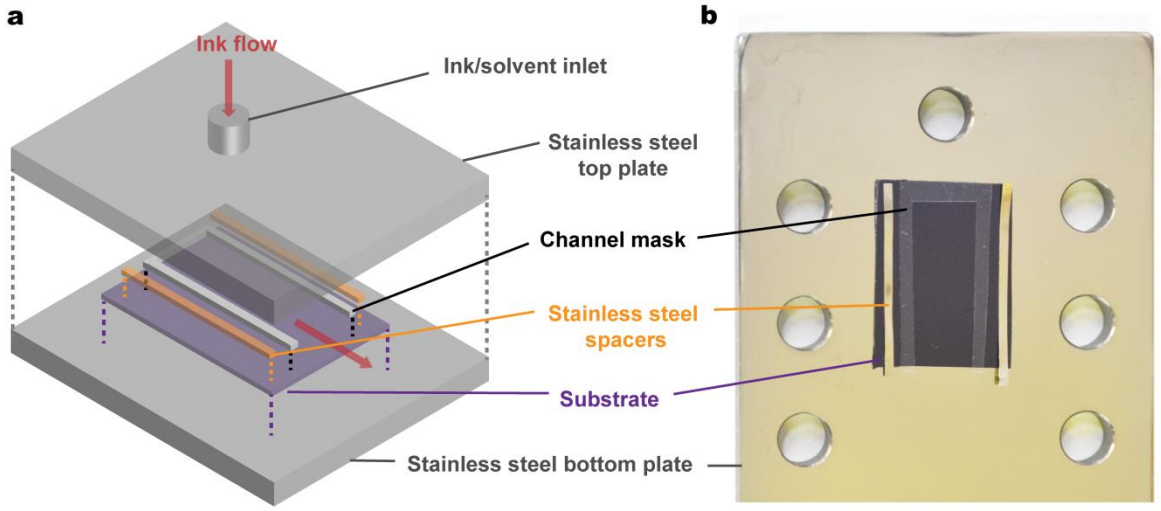


**Figure 5.1.** (a) Expanded view schematic and (b) top-view photograph of the experimental wafer-wide confined shear alignment setup with the top plate removed. The setup in the photograph accommodates 2.5 cm wide substrates. The substrate is placed on the stainless steel bottom plate. A channel mask made out of perfluoroalkoxy (PFA) is situated on the substrate to define the area for the ink to flow. The top plate has a tubing inlet to allow ink and solvent to flow across the substrate. Four bolts (M6 × 0.75) with 1.7 N-m of torque are used directly around the substrate to attach the top plate to the bottom plate and seal the channel. The remaining three bolts are hand-tightened. After tightening, the PFA mask compresses until the top plate hits the stainless steel spacers outside the channel mask.

**5.2.1 Effect of shear rate on nanotube alignment.** First, we study the effect of the shear rate on the alignment of the nanotubes. The shear rate during deposition is controlled using two methods: 1) the volumetric flow rate of the ink is varied while all physical dimensions of the channel are constant and 2) the channel height is varied while the volumetric flow rate of ink is constant. The shear rates are calculated assuming a planar Poiseuille flow with a symmetric parabolic velocity profile (see Appendix D for discussion of the calculation) using the derived formula for shear rate evaluated at the wall of the channel,

$$\frac{dV}{dy} = \frac{6Q}{d^2 w} \tag{5.1}$$

where $Q$ is the volumetric flow rate, $w$ is the width of the channel, and $d$ is the characteristic length of the rectangular channel cross-section. Equation 5.1 shows that the shear rate increases with $Q$ and $1/d^2$.

After deposition of nanotubes via confined shear alignment with varying shear rates, the degree of alignment is quantified via polarized Raman spectroscopy. The ratio of the nanotube G-band intensity with laser and analyzer polarizations parallel to the direction of alignment ($I_{VV}$) and perpendicular to the direction of alignment ($I_{HH}$) is measured at five different locations across the 1 × 1 cm$^2$ sample areas and then averaged. We approximate that the orientation of the nanotubes within the films follows a wrapped normal distribution. In this case, the half-width at half-maximum (HWHM) of the distribution can be related to the $I_{VV}/I_{HH}$ ratio. A larger $I_{VV}/I_{HH}$ ratio corresponds to a smaller HWHM, indicating less angular spread and a greater degree of alignment within the nanotube film. An HWHM of 0 and 90° corresponds to absolute unidirectional and random alignment, respectively. The entire process for measuring and calculating the HWHM is outlined in Appendix D.

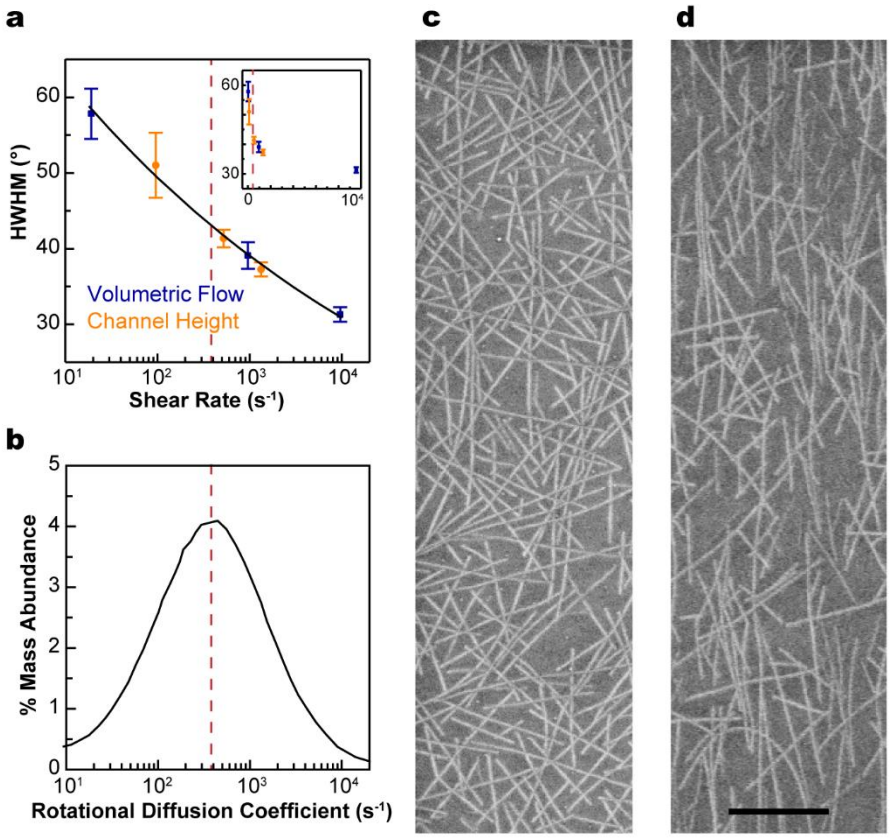


**Figure 5.2.** Effect of shear rate on nanotube alignment. (a) Half-width at half-maximum (HWHM) of alignment within a confined shear aligned nanotube film measured via polarized Raman spectroscopy as a function of shear rate plotted on a linear-log scale. Alignment increases with increasing shear rate, following a power-law with an exponent of -0.10, regardless of the method used to adjust shear (blue squares—

volumetric flow rate is varied, orange circles—channel height is varied). The inset is the same data plotted on a linear-linear scale. (b) The percent mass abundance of nanotubes with a given rotational diffusion coefficient as calculated from the nanotube length distribution fit from Brady et al.[3] The red dashed line at 386 $s^{-1}$ in both graphs in (a) and in (b) is the rotational diffusion coefficient with the greatest percent abundance in our nanotube inks. (c-d) SEM micrographs of nanotubes deposited on 90 nm of $SiO_2$ on Si using a shear rate of 19 and 9600 $s^{-1}$, respectively, from the volumetric flow rate series. The fluid flow direction is top to bottom of the page. Scale bar is 500 nm.

**Fig. 5.2a** plots the HWHM of the alignment for films fabricated via confined shear alignment at different shear rates (the inset shows the same data plotted on a linear-linear scale). Regardless of whether the volumetric flow rate or channel height is varied, the alignment of the nanotubes increases with increasing shear rate. For example, the HWHM decreases from 58 to 31° when the shear rate is increased from 19 to 9,600 $s^{-1}$ by increasing the volumetric flow rate from 100 µL $min^{-1}$ to 50 mL $min^{-1}$ at a fixed channel height of 120 µm and channel width of 9.4 mm. The HWHM also decreases from 51 to 37° when the shear rate is increased from 96 to 1330 $s^{-1}$ by decreasing the channel height from 235 µm to 31 µm at a fixed flow rate of 500 µL $min^{-1}$ and channel width of 9.4 mm. The concentration of nanotubes in the ink is 60 µg $mL^{-1}$ for both series, and the ink volume that is flowed through the channel is 285 µL and 170 µL for the volumetric flow and channel height series, respectively.

Alignment is expected when the shear rate is much greater than the rotational diffusion coefficient, $D_r$.[103] We therefore calculate the distribution of $D_r$ in our nanotube inks ($d$ = 1.5 nm) using the length distribution of our nanotubes and Equation 5 from Tirado et al.,[105]

$$D_r = \frac{3k_BT}{\pi\eta_0 {L_r}^3}\left(\ln\left(\frac{L_r}{d_r}\right) + \delta_\perp\right) \tag{5.2}$$

where $k_B$ is the Boltzmann constant, $T$ is the temperature, $\eta_0$ is the viscosity, and $L_r$ and $d_r$ are the rod length and diameter, respectively. $\delta_\perp$ is related to the rod length/diameter ratio ($L_r/d_r$) and encompasses so-called end-effect corrections, discussed in more detail by Tirado et al. This equation assumes that the nanotubes are in an infinitely diluted state (i.e., no interactions with other nanotubes or objects in solution).[105] From this equation, the percent mass abundance of nanotubes with a given $D_r$ is plotted in **Fig.**

**5.2b**, where the red dashed vertical line in **Fig. 5.2a,b** corresponds to the rotational diffusion coefficient with the greatest abundance, ~386 $s^{-1}$. However, this $D_r$ is likely an overestimate, as the presence and interaction of nanotubes with other nanotubes or free PFO-BPy in solution will, to some extent, reduce the $D_r$ (see Supporting Information for discussion of the calculation).

In bulk solution, the degree of alignment attainable via shear is expected to follow a power-law dependence with an exponent of -0.33.[106,107] In contrast, we observe an exponent of -0.10. This discrepancy is likely in part due to the $D_r$ polydispersity within our nanotube inks (**Fig. 5.2b**) and also that the polarized Raman measurement itself is nonlinear. This difference in exponent may also indicate that some of the alignment obtained in the bulk of the solution is lost as the nanotubes interact with the substrate as they are deposited. For example, if the front end of a nanotube that is well-aligned in bulk solution adheres to the substrate before the rest of the nanotube can adhere, then this nanotube will rotate about its front end, pushed by the flow, until the trailing end adheres to the substrate. This scenario may give rise to the misaligned 'U' shaped nanotubes that we commonly observe (see, for example, the bottom of **Fig. 5.2d** to the left and above the scale bar or **Fig. D3**).

**5.2.2 Effect of nanotube ink concentration and volume on confined shear alignment.** Control over nanotube packing density within aligned nanotube films is vital to optimize the performance of nanotubes for specific applications. We expect that by increasing the number of nanotubes that flow over the substrate, more nanotubes will deposit on the substrate, and it may be possible to control the packing density. We therefore study the effect of ink concentration and ink volume on the packing density. After deposition of nanotube films via confined shear alignment, the packing density is determined from maps of the G-band Raman intensity, as discussed in the Methods section (5.4).

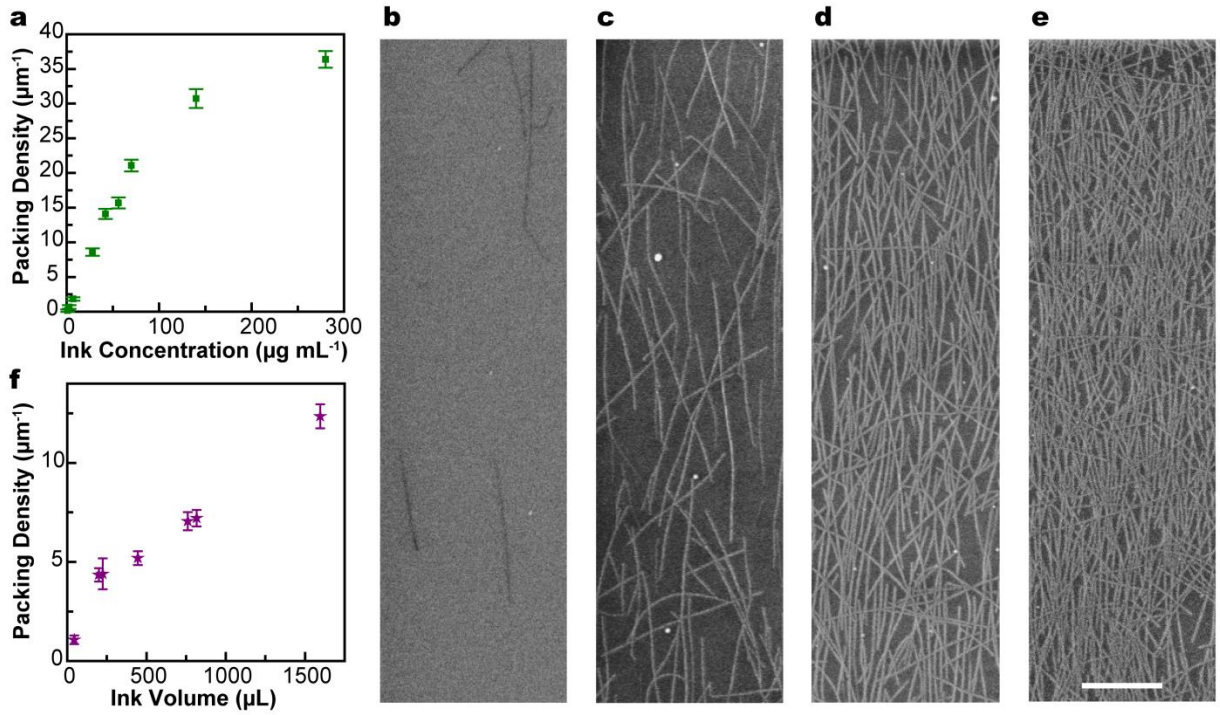


**Figure 5.3.** Effect of nanotube ink concentration and ink volume on packing density. (a) Plot of packing density versus ink concentration (at constant ink volume of 250 µL). (b-e) SEM images of four films from part (a) prepared at ink concentrations of 2.8, 42, 140, and 280 µg $mL^{-1}$, respectively, with resulting packing densities of 0.7, 14, 31, and 36 $\mu m^{-1}$, respectively. Scale bar is 500 nm. The fluid flow direction is from top to bottom of the page. In part (a), the packing density increases steeply with increasing ink concentration until a density of ~30 $\mu m^{-1}$ is reached, and then increases more slowly. Our hypothesis is that the packing density begins to saturate at 30 $\mu m^{-1}$ because at this density, newly deposited nanotubes must adhere to the substrate by sticking to previously deposited nanotubes as opposed to sticking to the bare substrate. (f) Plot of packing density as a function of nanotube ink volume (at constant ink concentration of 14 µg $mL^{-1}$). For these data, the channel height is 120 µm, the volumetric flow rate is 100 mL $min^{-1}$, and the channel width is 9.4 mm.

As shown in **Fig. 5.3**, both the nanotube ink concentration and ink volume can be used to control nanotube packing density in films fabricated via confined shear alignment. The data in **Fig. 5.3a** and SEM micrographs in **Fig. 5.3c-e** illustrate the effect of ink concentration on nanotube packing density at a fixed volume of 250 µL. At low concentrations, the packing density increases steeply with ink concentration until a packing density of ~30 $\mu m^{-1}$ is reached. At this point, the rate at which nanotubes deposit decreases, and the packing density increases more slowly with ink concentration. An SEM micrograph of a film deposited at the condition at which the slope transitions from steep to shallow is shown in **Fig. 5.3d**. At this density

of 30 nanotubes $\mu m^{-1}$, nanotubes flowing across the substrate cannot adsorb to the bare substrate without overlapping previously deposited nanotubes, slowing the rate at which nanotubes adsorb.

The effect of ink volume on nanotube packing density at constant ink concentration of 14 $\mu g\ mL^{-1}$ is also shown in **Fig. 5.3f**. The packing density increases as the volume of ink that is flowed over the substrate increases. An initial steep increase in packing density is observed when the ink volume is increased from 45 to 250 µL. It is unclear what causes the sharp increase in packing density from ~50 to 250 µL, but we hypothesize that it could be due to a secondary effect from the leading ink/air interface or a concentration gradient within the ink that becomes more prevalent at lower ink volumes.

**5.2.3 FETs fabricated from confined shear aligned carbon nanotube arrays.** Charge transport measurements are conducted using a field-effect transistor (FET) architecture to elucidate the effect of alignment and packing density on the mobility of highly pure semiconducting nanotube films deposited via confined shear alignment. These measurements are conducted on aligned films of nanotubes with an HWHM of 34°. After deposition of the nanotubes on 15 nm $SiO_2$ on Si substrates, isolated regions of nanotubes with width $W_{ch}$ = 10 µm are defined using electron-beam lithography and reactive ion etching. The films are then immersed in boiling toluene to remove excess PFO-BPy and vacuum annealed to decompose the PFO-BPy and remove chlorine impurities introduced on the nanotube from dispersing in chloroform.[22] This vacuum anneal treatment has been shown to only partially remove the PFO-BPy wrapper, however, complete removal of the polymer has not been shown to improve aligned nanotube FET performance.[108,109]

Next, source and drain electrodes with a channel length $L_{ch}$ of 0.5–5 µm are patterned within the isolated regions of nanotubes via electron-beam lithography, development, and thermal deposition of 17.5 nm of Pd and 17.5 nm of Au.

The effect of nanotube alignment on charge transport is studied by aligning the mobility direction of the channels of the FETs to be parallel to the direction of alignment in the nanotube films (termed "parallel FETs", **Fig. 5.4a**) and perpendicular to the direction of alignment in the nanotube films (termed "perpendicular FETs", **Fig. 5.4b**). Roughly four parallel and perpendicular FETs, with nanotube packing density of 59 $\mu m^{-1}$, are measured at $L_{ch}$ of 0.5, 1, 2, 3, and 5 μm using a source-drain bias $V_{DS}$ of -1 V.

Representative source-drain current $I_{DS}$ versus gate-source bias $V_{GS}$ curves of parallel and perpendicular FETs with $L_{ch}$ of 1 μm are shown in **Fig. 5.4c** for the forward $V_{GS}$ sweep (negative to positive voltage). Hysteresis is observed in the full sweeps, as shown in **Fig. D4**, which is expected for nanotube FETs on $SiO_2$ substrates and measured in ambient conditions. The mobility of the parallel FETs is 7× higher than that of the perpendicular FETs. For the 59 $\mu m^{-1}$ packing density devices, the on/off ratio of the parallel FETs is always greater than $2 \times 10^5$ and is, on average, $6 \times 10^5$, while the on/off ratio of the perpendicular FETs is always higher than $6 \times 10^3$ and is, on average, $2.5 \times 10^5$. Measurement of the intrinsic off-current of both parallel and perpendicular FETs is prevented by capacitive current from the $SiO_2$ ($I_{GS}$ versus $V_{GS}$ curves are shown in **Fig. D4**), and therefore the intrinsic on/off ratios are expected to be higher than what is measured here. Regardless, these data indicate that the high degree of alignment of the nanotube films deposited by confined shear alignment directly results in improvements in both the on-current and on/off ratio of the FETs.

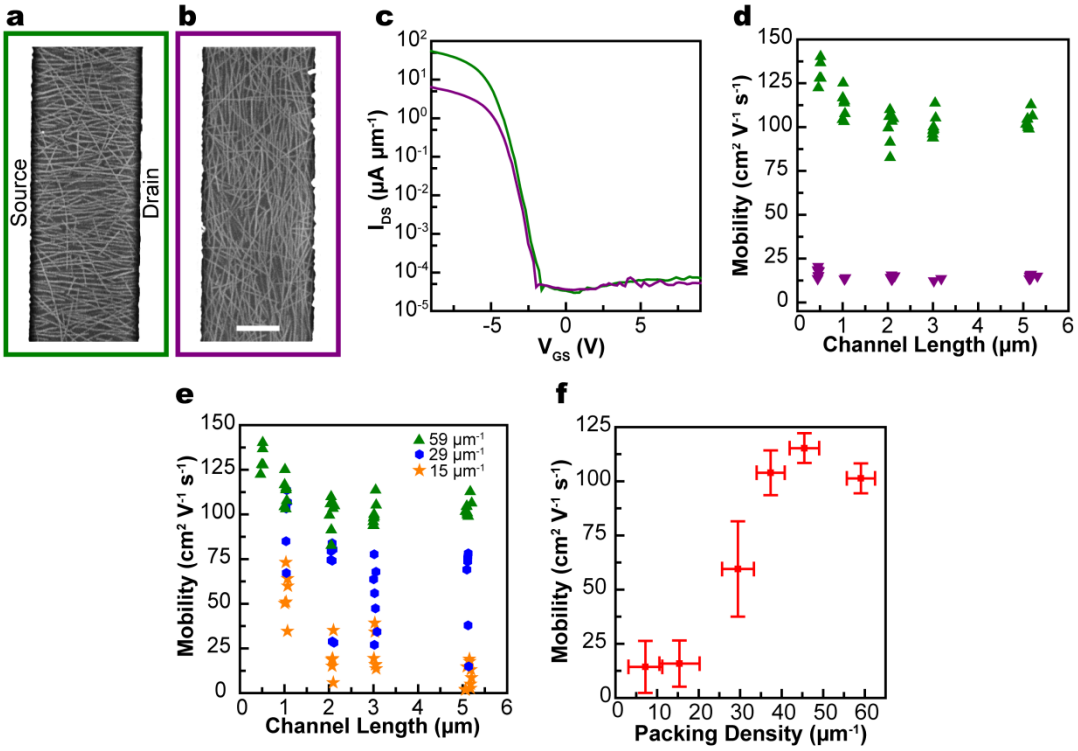


**Figure 5.4.** FETs fabricated from confined shear aligned nanotube films. (a-b) SEM micrographs of FETs in which the direction of nanotube alignment is oriented parallel (a) and perpendicular (b) to the channel that is defined by the source and drain electrodes. Scale bar is 500 nm. (c) Representative $I_{DS}$ versus $V_{GS}$ curves measured at $V_{DS}$ of -1 V of the parallel (green) and perpendicular (purple) nanotube FETs with $L_{ch}$ = 1 μm and packing density of 59 μm$^{-1}$. (d) Extracted hole mobility of parallel (green) and perpendicular (purple) nanotube FETs as a function of $L_{ch}$ using a packing density of 59 μm$^{-1}$. (e) Extracted hole mobility of parallel FETs as a function of $L_{ch}$ using a packing density of 15 (orange stars), 29 (blue hexagons), and 59 (green triangles) μm$^{-1}$. (f) Average hole mobility of parallel FETs with $L_{ch}$ = 2 – 5 μm as a function of nanotube packing density. For this data, the PFA mask and channel height are 127 μm and 120 μm, respectively. The ink volume is 250 μL. The volumetric flow rate is 100 mL min$^{-1}$. The width of nanotube deposition for each film is 10.5 mm. The mobility plotted in parts d-f is calculated using the array capacitance (see main text).

The hole mobility of the nanotube FETs with packing density of 59 μm$^{-1}$ is plotted against $L_{ch}$ for parallel and perpendicular FETs in **Fig. 5.4d**, where the mobility is calculated as

$$\mu = \frac{L_{ch} g_{ch}}{C_{array} W_{ch} V_{DS}} \tag{5.3}$$

where $g_{ch}$ is the maximum magnitude of the slope of the $I_{DS}$ versus $V_{GS}$ curve (i.e., the transconductance), and $C_{array}$ is the capacitance of the nanotube array and is a function of nanotube packing density. At each

$L_{ch}$, a greater than 7× increase in mobility is observed for parallel FETs compared to perpendicular FETs, indicating that the mobility of these FETs is improved due to the alignment of the confined shear aligned nanotube films. The average mobility of the parallel and perpendicular FETs with $L_{ch}$ of 2 – 5 μm (where the mobility is fairly constant, seen in **Fig. 5.4d**) is 101 and 14 $cm^2V^{-1}s^{-1}$, respectively, assuming an array capacitance, and 49 and 7 $cm^2V^{-1}s^{-1}$, respectively, assuming a parallel plate capacitance. The array capacitance is calculated from Eq. 3 of Brady et al.[3] and more accurately quantifies the channel-gate capacitance since the separation between nanotubes exceeds the gate dielectric thickness. There is a slight increase in mobility for parallel FETs at $L_{ch}$ less than 1 μm, which is likely due to a larger proportion of the nanotubes directly spanning the source and drain electrodes. In the case where the $L_{ch}$ is greater than 1 μm, nanotubes infrequently directly span the source and drain electrodes and therefore charge must be transferred from tube to tube via a percolating network. It has previously been shown that these tube/tube junctions increase the resistance of the FETs. Consequently, in long channel devices in which $L_{ch}$ is much greater than the average nanotube length, it is important to increase alignment so as to reduce the number of nanotube/nanotube junctions that charges need to traverse in order to cross the channel, thereby reducing the channel resistance and increasing the on-current. If the degree of alignment is too high, however, the nanotubes will cease to overlap, reducing the number of percolation pathways over which charge can be transported, decreasing the on-current.

In addition to alignment, the packing density of the nanotubes can also affect the performance of nanotube FETs by varying the density of charge percolation pathways. We therefore study the effect of packing density on the mobility of parallel FETs (which show better charge transport than perpendicular FETs) as a function of $L_{ch}$ from 0.5 to 5 μm. **Fig. 5.4e** shows that the mobility increases for all $L_{ch}$ with increasing packing density from 15 to 29 to 59 $\mu m^{-1}$. Similar to the parallel FETs in **Fig. 5.4d**, the mobility slightly increases as the $L_{ch}$ decreases below 1 μm.

The average mobility of parallel FETs with $L_{ch}$ of 2 – 5 μm (the range of $L_{ch}$ over which the mobility is relatively constant in **Fig. 5.4d,e)** is plotted as a function of packing density in **Fig. 5.4f**. We observe a

steep increase in mobility at approximately 30 $\mu m^{-1}$. We attribute this increase in mobility to an increase in the number of charge percolation pathways as the packing density is increased. The mobility saturates at a packing density of 45 $\mu m^{-1}$, indicating that this is the optimal packing density for confined shear aligned films with an HWHM of 34°. Our FET performance is consistent with other mobility values in literature (0.4 – 287 $cm^2V^{-1}s^{-1}$) reported for carbon nanotube FETs ($L_{ch}$ > 500nm) fabricated via post-synthetic assembly with on/off ratios greater than $10^3$.[3,21,37,110] We expect that FETs with even higher mobility can be achieved with nanotube films deposited via confined shear alignment by further increasing both the degree of alignment, so as to reduce the number of nanotube crossings that charges must traverse from the source to the drain, and the packing density, so as to increase the number of percolation pathways in the channel.

**5.2.4 Aligned nanotube arrays over 8 × 8 $cm^2$ via confined shear alignment**. It is clear from these data that films of nanotubes with high degree of alignment, controlled packing density, and promising charge transport properties for TFTs can be deposited onto substrates from solution using confined shear alignment. We next explore the ability of confined shear alignment to scale to large areas to deposit uniform films of aligned nanotubes over the wafer scale.

In order to increase the deposition area, we simply increase the size of the confined shear alignment apparatus to accommodate a larger 10 × 10 $cm^2$ wafer. We also utilize 19.0 mm thick steel sheets for the top and bottom plates to reduce the bowing across the channel. A small trough spanning across the top of the channel is milled around the tube fitting adapter on the inside of the top plate as shown in **Fig. D5**. This inset allows the ink to collect first before flowing across the substrate to ensure uniform flow across the relatively large substrate. The inside of the top plate is polished to a roughness of 92 ± 22 nm (measured via Zygo interferometry) to minimize the deviation in channel height, and therefore the shear rate, over the substrate and increase deposition uniformity. In order to deposit nanotubes over a 8 × 8 $cm^2$ area of the substrate, 2 mL of ink at a concentration of 80 $\mu g\ mL^{-1}$ is flowed at a shear rate of 10,700 $s^{-1}$, which is achieved using a volumetric flow rate of 100 mL $min^{-1}$ and channel height of 30.4 μm. After deposition,

the sample is dried using a critical point dryer (Tousimis Automegasamdri 915b) to prevent surface tension during drying to tear or delaminate the nanotube film.

An optical image, obtained using a conventional digital camera (Nikon D3100), of the resulting sample deposited over 8 × 8 $cm^2$ onto 90 nm of $SiO_2$ on Si is shown in **Fig. 5.5a**.

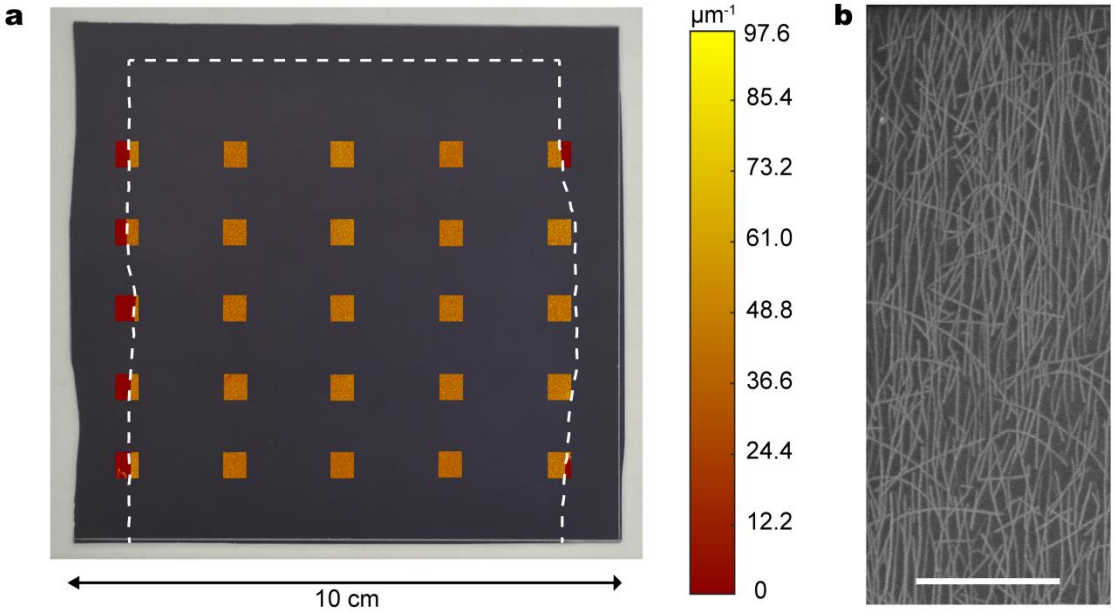


**Figure 5.5.** Confined shear aligned nanotube film deposited across an 8 × 8 $cm^2$ area on 90 nm of $SiO_2$ on Si. (a) Raman spectroscopy map of the nanotube packing density overlaid on an optical image of the sample. The white dashed line indicates the approximate edges of the mask used to define the deposition channel. (b) SEM micrograph of the aligned nanotubes (light contrast) within the confined shear aligned film shown in (a). Scale bar is 1 μm.

To evaluate film uniformity, smaller Raman spectroscopy maps (each with area of 0.5 × 0.5 $cm^2$) of the nanotube packing density are measured in a grid across an 8 × 8 $cm^2$ area. This grid of maps is measured instead of the full area of the sample due to instrument limitations. These smaller Raman maps are shown in **Fig. 5.5a** overlaid on the photograph. The average packing density across the channel area measured by comparing the average packing density in each map is 48.8 ± 4.8 $\mu m^{-1}$. A second grid of 25, smaller Raman

maps (250 × 250 μm$^2$ area) over a similar area (6.8 × 6.0 cm$^2$) are measured and the packing density is 47.2 ± 5.0 μm$^{-1}$, indicating high uniformity within the film across multiple length scales. An example Raman map from this grid of 250 × 250 μm$^2$ maps is shown in **Fig. D6**. The HWHM alignment within the film measured using polarized Raman spectroscopy across a ~6 × 6 cm$^2$ area of the nanotube film is 27.4 ± 1.9°. These results demonstrate that the area of deposition in the confined shear alignment method can be easily and simply scaled to achieve aligned nanotube films of nanotubes with relatively uniform packing density over large areas.

**5.3 Conclusion.**

The alignment of individualized, electronics-grade semiconducting carbon nanotubes in uniform, continuous films at packing densities relevant for electronics has been a challenge for many years. While significant progress has been made toward this goal, no single technique has accomplished all of these objectives. Here, we demonstrate that confined shear alignment is an attractive candidate for achieving these objectives.

We show that the nanotube ink concentration and volume can both be used to control the nanotube packing density, and we vary the shear rate by changing both the channel height and the ink flow rate. We fabricate FETs (channel length 1 – 5 μm) with alignment of ±34°, both parallel and perpendicular to the direction of alignment. The parallel transistors perform with 7× faster mobility (101 and 49 cm$^2$V$^{-1}$s$^{-1}$ assuming array and parallel plate capacitances, respectively) with high on/off ratio of $10^5$. The mobilities of our FETs exceeds or compares favorably to that of other carbon nanotube FETs fabricated via post-synthetic assembly with on/off ratios greater than $10^3$. In addition, however, we also demonstrate uniform deposition of aligned carbon nanotubes across an 8 × 8 cm$^2$ region. The degree of misalignment present in these films makes this confined shear alignment ideal for long-channel thin film transistors where some misalignment is needed to ensure percolation. Furthermore, the reduction of resistive nanotube/nanotube junctions in these films indicates confined shear aligned carbon nanotube films will be electrically superior to random nanotube networks currently produced via spin-, dip-, or blade-coating. One way to further

improve the alignment within the carbon nanotube films is by increasing the length of the carbon nanotubes within the carbon nanotube ink. Increasing the mode of the tube length distribution decreases the rotational diffusion coefficient distribution. This shifts the percent mass abundance curve shown in **Fig. 5.2b** to the left, allowing for better alignment at any given shear rate. Finally, optimized conditions enable alignment within a ±27° window, at an intermediate packing density of 50 nanotubes $\mu m^{-1}$, on a 10 × 10 $cm^2$ substrate.

The simplicity of the confined shear alignment apparatus and technique demonstrates that further scaling to even larger areas should be possible and easily implemented. As the technique is further scaled, maintaining uniformity over increasingly larger areas will be aided by the relative insensitivity of both the packing density and the degree of alignment to the deposition conditions (i.e., the packing density is only weakly affected by the number of nanotubes that flow over the substrate once a density of 30 nanotubes $\mu m^{-1}$ is reached and the degree of alignment is relatively invariant once the shear rate exceeds 1000 $s^{-1}$). This work is important because, compared to random networks, films of aligned nanotubes promise to be a superior platform for applications including environmental and biological sensors, flexible/stretchable electronics for hybrid, soft, and integrated electronics, and novel light emitting and harvesting devices.

## 5.4 Materials and methods.

**5.4.1 Preparation of PFO-BPy-wrapped nanotubes.** Semiconducting carbon nanotubes are extracted from arc-discharge nanotube soot (Sigma-Aldrich, #698695) using a 1:1 ratio by weight of the raw soot and a polyfluorene derivative polymer wrapper, poly[(9,9-dioctylfluorenyl-2,7-diyl)-*alt*-*co*-(6,6'-{2,2'-bipyridine})] (PFO-BPy) (American Dye Source, Inc., Quebec, Canada; #ADS153-UV). This soot/PFO-BPy mixture is dispersed at 2 mg $mL^{-1}$ in 60 mL of toluene and sonicated at 40% amplitude with a horn tip sonicator (Fisher Scientific, Waltham, MA; Sonic Dismembrator 500) for 10 min. This solution is centrifuged in a swing bucket rotor (Sorvall WX, TH-641, Thermo-Scientific) at 3 × $10^5$ g for 10 min to remove soot and undispersed nanotubes. The upper 90% of the supernatant is collected and concentrated to a volume of 60 mL. This concentrated supernatant is centrifuged for 18 – 24 h and dispersed in toluene via

sonication utilizing the horn tip sonicator. This process of centrifugation and sonication in toluene is repeated three times to remove most of the excess PFO-BPy. The final solution is prepared by horn tip sonication of the rinsed carbon nanotube pellet in chloroform (stabilized with ethanol from Fisher Scientific, #C606SK-1). The concentration of the nanotubes in solution is determined using known optical cross sections from the $S_{22}$ transition.[88]

**5.4.2 Preparation of substrates.** $Si/SiO_2$ substrates with 90 nm or 15 nm of dry, thermal oxide are used in this work. The substrates are cleaned with a piranha solution 2:1 ratio by volume of $H_2SO_4$ (91 – 92.5%):$H_2O_2$ (30%) in a crystallizing dish on a 110 °C hot plate for 60 min (for 90 nm oxide) or 15 min (for 15 nm oxide), rinsed with deionized water, and dried with $N_2$.

**5.4.3 Fabrication of semiconducting carbon nanotube FETs.** Isolated regions of nanotubes are first defined using electron-beam lithography with polymethylmethacrylate (PMMA) as the resist followed by development in 2:1 methyl isobutyl ketone (MIBK):IPA for 1 min. Next, an oxygen reactive ion etch is used to remove the exposed nanotubes, and the remaining PMMA is removed with acetone. These patterned nanotube films are boiled in toluene at 120 °C for 1 h and vacuum annealed at 400 °C for 1 h at ~ $10^{-5}$ torr. Source and drain contacts are then patterned to define the nanotube FET channels via electron-beam lithography using PMMA and the same development described above. Thermal evaporation is used to deposit the contacts, 17.5 nm Pd/17.5 nm Au, the Si substrate is used as a back gate, and 15 nm of $SiO_2$ is used as the gate dielectric. All devices are measured at room temperature in ambient conditions using a Keithley 2636A SourceMeter.

**5.4.4 Spectroscopy characterization.** Raman Spectroscopy (Thermo-Fisher Scientific DXRxi Raman Imaging Microscope) with laser excitation wavelength of 532 nm is used to measure the ratio of the area of the nanotube G-band (~1590 $cm^{-1}$) to the area of the Si peak (~520 $cm^{-1}$) to quantify the amount of nanotubes deposited.[111] This G/Si ratio is converted to a linear packing density using a relationship empirically measured from SEM at lower packing densities (shown in **Fig. B7**). Prior to Raman measurement, each nanotube film is boiled in toluene at 120 °C for 1 h to remove excess PFO-BPy and

then vacuum annealed at 400°C for 1 h at ~ $10^{-5}$ torr. To ensure there is no effect from any remaining conjugated polymer wrapper on the G-band and G/Si measurement, a control sample is fabricated by performing the confined shear alignment process with a solution of PFO-BPy in chloroform (10 μg $mL^{-1}$). This control substrate undergoes the post-treatment toluene boil and vacuum anneal as previously stated for the nanotube films. The Raman spectrum from this PFO-BPy control is shown in **Fig. D8** and shows no G-band signal. This Raman spectrometer is also employed for the large-area mapping of a confined shear aligned film (**Fig. 5.5**). Because of the size of the substrate, the sample in **Fig. 5.5** cannot be vacuum annealed. Polarized Raman spectroscopy (Aramis Horiba Jobin Yvon Confocal Raman Microscope) is performed with a laser excitation wavelength of 532 nm by placing linear polarizing filters on both the analyzer and laser.

# **Chapter 6.** Confined shear alignment of ultrathin films of cellulose nanocrystals

Chapter 6 was adapted from Jinkins, K. R. & Arnold, M. S. Confined Shear Alignment of Ultrathin Films of Cellulose Nanocrystals. *In preparation*. (2020). K.R.J. and M.S.A. performed all experiments, data collection, and analysis. K.R.J. drafted the manuscript. The cellulose nanocrystals were supplied by Richard S. Reiner at the USDA Forest Products Laboratory.

**Abstract:** Cellulose nanocrystals (CNCs) are a naturally abundant nanomaterial derived from cellulose which exhibit many exciting mechanical, chemical, and rheological properties making CNCs an attractive material for use in coatings and to study in model films. Toward this goal, in this work, aligned films of ultrathin CNCs are fabricated using solution-based shear alignment. CNC solution is forced through a sub-mm tall channel at high volumetric flow rates generating large amounts of aligning shear. By increasing the shear rate from 19 $s^{-1}$ to 19000 $s^{-1}$, the half-width at half-maximum (HWHM) of the spread in CNC alignment is significantly improved from 130° to 33°. We demonstrate that the film thickness is increased by increasing the CNC solution volume and/or increasing the CNC solution concentration, with a degradation in film uniformity at higher (7 wt%) concentrations, likely due to CNC aggregates in solution. Deposition of ultrathin aligned CNC films occurs within seconds and the technique is inherently scalable, demonstrating the promise of solution-based shear for fabrication of ultrathin aligned CNC films to study their inherent material properties or for use in high-performance coatings and applications.

## 6.1 Introduction.

Cellulose nanocrystals (CNCs) are the basic building blocks of cellulose, and occur abundantly in nature, such as in wood pulp or the cell walls of green vegetation.[112,113] In addition to their renewable nature leading to sustainable and biodegradable products with low environmental footprint, CNCs also exhibit

useful material properties including comparatively high intrinsic strength,[114] enabling their integration in applications like composites and textiles to provide passive strength. CNCs additionally have large permanent dipoles,[115] making their use in energy harvesting or flexoelectric applications particularly appealing.[116] Moreover, the fabrication of specifically ultrathin CNC films also has many exciting applications. For example, ultrathin cellulose films have been investigated as biosensors,[117,118] environmentally friendly photoresist,[119] dielectric material in thin-film transistors,[119] and as photonic crystals for relative humidity and gas sensors[120] among others. The fabrication of ultrathin films of CNCs is useful to not only exploit the material properties of CNCs in applications,[121] but also to study their inherent material properties in so-called model surfaces.[122] Model surfaces of ultrathin CNC films enable fundamental studies on basic cellulose and CNC interactions, such as cellulose friction forces or the effect of different environmental conditions on cellulose swelling, which both have direct application in papermaking and the intended usage of paper products.[122]

Multiple techniques have been developed to fabricate ultrathin films of CNCs from solution, including Langmuir-Blodgett and -Schaefer[123] methods, spin-coating,[124,125] and drop-casting,[125] which produce films of CNCs with primarily random alignment. However, the organization of CNCs into aligned films is attractive because of the improved mechanical characteristics[126] and opportunity to align their inherent dipoles and utilize their piezoelectric properties.[127] Above certain concentrations, CNCs in solution exhibit chiral nematic (cholesteric) assemblies,[128] which researchers have tried to exploit to achieve CNC films with higher global alignment. Typical processes for aligning CNCs are time consuming, requiring hours or days for films to assemble, including Dr. Blading[129], or are also expensive, requiring large magnetic[130,131] or electric fields[132,133]. Additionally, the majority of these techniques result in thick films and do not provide control over the film thickness—not ideal for ultrathin coatings and studies based on CNC model films.[122] Alignment of CNCs in ultrathin films in a more time-efficient process has been demonstrated via evaporation-induced alignment.[134]

In this chapter, we demonstrate confined, shear-based alignment (discussed in more detail in the previous chapter for aligning carbon nanotubes) as a quick and simple process to fabricate ultrathin films of aligned CNCs with improved control over the degree of alignment attained. The experimental apparatus used for the shear alignment of CNCs is shown in **Fig. 6.1**. By forcing the CNC solution through a sub-mm channel across the target substrate, large amounts of shear are generated, which align the CNCs with the direction of flow (**Fig. 6.1a,b**). In this work, we use a channel height of 120 μm and a channel width of 9.6 mm, however, solution-based shear has also been previously used to align carbon nanotubes uniformly across 10 cm wide substrates, demonstrating the inherent scalability of this technique.[135] Here, we achieve control over the degree of alignment and thickness of ultrathin CNC films by varying the shear rate and solution concentration or volume, respectively, enabling exploration of the effect of these film characteristics on applications and model films.

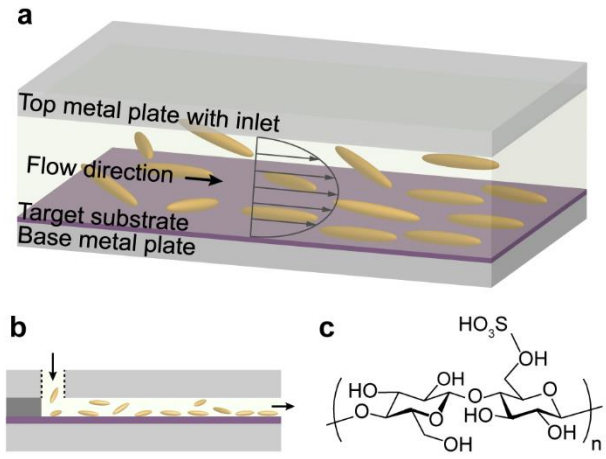


**Figure 6.1.** Apparatus for shear-alignment of CNCs. (a,b) 3D (a) and side-view (b) of shear-alignment apparatus. (c) Chemical structure of CNCs used in this work. The content of sulfur on dry CNCs is 1.06 by wt%.

## 6.2 Results and discussion.

**6.2.1 Quantification of CNC alignment with polarized Raman spectroscopy.** In this chapter, the degree of alignment in ultrathin films of aligned CNCs is quantified using polarized Raman spectroscopy, which

is a powerful technique for quantifying alignment of anisotropic structures in films and in bulk and has been previously utilized on aligned CNC films.[136–138] CNCs exhibit different bands with angle-dependent Raman signal,[139] however, the 1098 and 2890 $cm^{-1}$ bands are attractive for analysis due to their relatively high intensities.[138] In experiment, the ratio of the 1098 to 2890 $cm^{-1}$ bands is used to quantify the degree of alignment because it eliminates the need for external normalization of the Raman signal. Specifically, the dependence of the ratio on the deviation of the film alignment with respect to the polarization axis is used to quantify the degree of alignment. Consequently, either the sample or polarizer needs to be rotated during the measurement. However, this rotation is both time-consuming and can introduce errors in the extracted degree of alignment, as many Raman spectrometers do not have polarizer rotation capabilities or a rotation stage sufficiently accurate to measure the same spot in the film after rotation. Here, we instead use a simpler method (discussed in detail in Appendix E) that relies on only the 1098/2890 ratio at a single point, as well as measurement of a control CNC film that is random and unaligned to quantify the local degree of alignment.

**6.2.2 Effect of shear rate on CNC alignment.** The effect of shear rate on the degree of CNC alignment is studied by varying the volumetric flow rate of the CNC solution. For example, volumetric flow rates of 0.1 and 100 mL $min^{-1}$ result in shear rates of 19 and 19,000 $s^{-1}$, respectively assuming a planar Poiseuille flow and symmetric parabolic velocity profile (as calculated previously[135], shown in Appendix D). **Fig. 6.2** shows the effect of shear rate on film morphology, characterized by AFM **(a-d)** and polarized Raman spectroscopy **(e)**. The AFM height maps qualitatively indicate that the alignment of the CNC films increases with increasing shear rate. Polarized Raman spectroscopy shows that the half-width at half-maximum (HWHM) of the alignment decreases from 130° at a shear rate of 19 $s^{-1}$ to 33° at a shear rate of 19000 $s^{-1}$. The alignment of CNCs in **Fig. 6.2e** follows a power-law with an exponent of -0.20 in contrast to the alignment of carbon nanotubes, which follows a power-law with an exponent of -0.10 (**Fig. 3.2**).[135] Alignment of anisotropic structures in bulk solution is expected to follow a power-law with an exponent of

-0.33,[106,107] so the alignment of CNCs matching this prediction more closely than nanotubes could be due to the smaller persistence length of CNCs. We hypothesize that the remaining deviation between the exponent measured here and theory is caused by the effect of the substrate or the size polydispersity of the CNCs in solution.

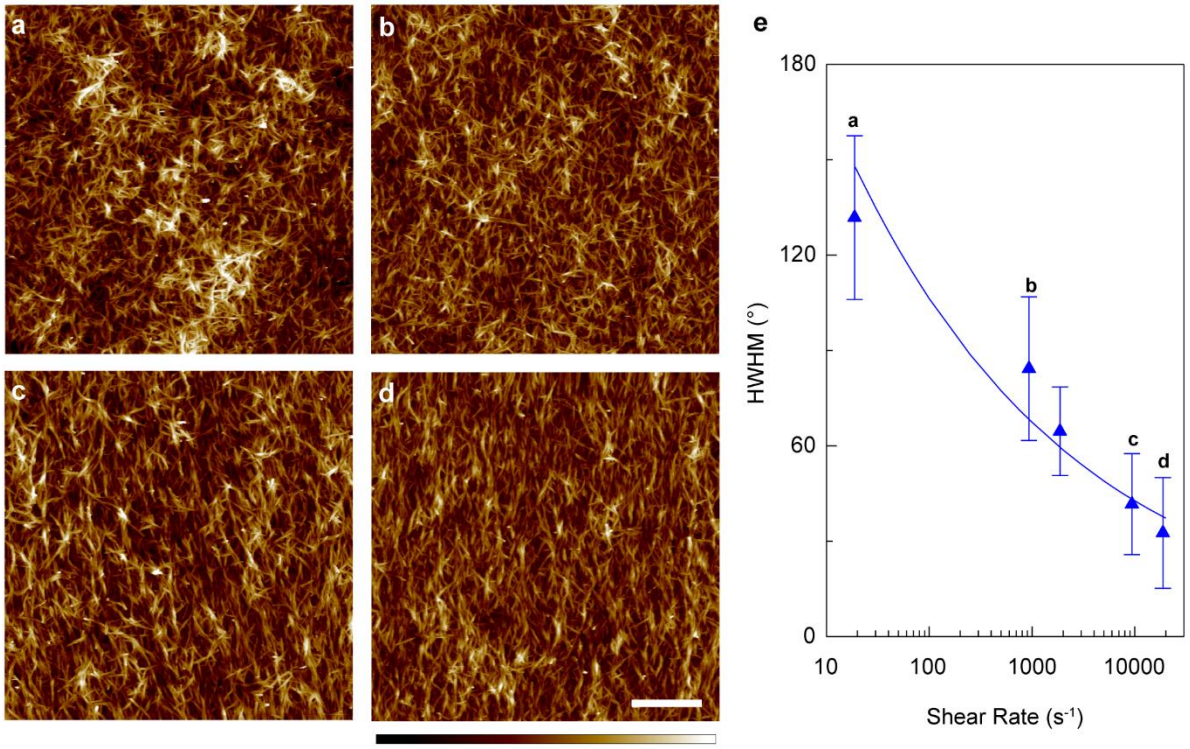


**Figure 6.2.** Effect of shear rate on alignment in ultrathin CNC films. (a-d) AFM height scans at shear rates of 19, 937, 9365, 18730 $s^{-1}$. Scalebar in (d) is 500 nm and applies to (a-d). The range of the height scalebar under (d) is 75 nm and applies to (a-d). (e) HWHM of CNC alignment measured by polarized Raman spectroscopy versus shear rate. Data points corresponding to the AFM height images in (a-d) are indicated.

**6.2.3 Effect of CNC concentration on film thickness and morphology.** Control over the CNC film thickness is important for many applications. We expect that by increasing the concentration of CNCs in solution, it will be possible to deposit thicker films of aligned CNCs. Here, we study the effect of the CNC solution concentration at a constant volume (1 mL) and shear rate (19,000 $s^{-1}$) on the aligned film morphology (**Fig. 6.3**). At a low concentration of 0.1 wt% (**Fig. 6.3b**) the film thickness is 2.4 ± 0.6 nm and the coverage is submonolayer. The film thickness steeply increases with concentration until saturating

around 25 nm. For example, the film thickness obtained at a concentration of 5 wt% (**Fig. 6.3c**) is 26.7 ± 1.1 nm. However, at high concentrations (e.g., 7 wt%), the variation in film height increases—as evidenced by the large error bar in **Fig. 6.3a** and the film morphology observed in polarized optical microscopy (POM) images. In POM images, the film appears as bright yellow when the CNC alignment (here, oriented vertical to the page) is oriented 45° between the perpendicularly aligned polarizers (**Fig. 6.3d**, top of **Fig. 6.3e**). Whereas, when the film alignment is parallel to one of the polarizer directions, the POM images appear dark (bottom of **Fig. 6.3e**). We find that at a lower concentration of 3.5 wt%, the POM image is uniformly bright yellow (**Fig. 6.3d**), indicating that the film is uniformly aligned over the field-of-view. In contrast, at a higher concentration of 7 wt% (top of **Fig. 6.3e**), dark imperfections are seen. These imperfections correspond to divots in the film (increasing the variation of film height), which are likely caused by larger CNC aggregates in solution at larger concentrations.

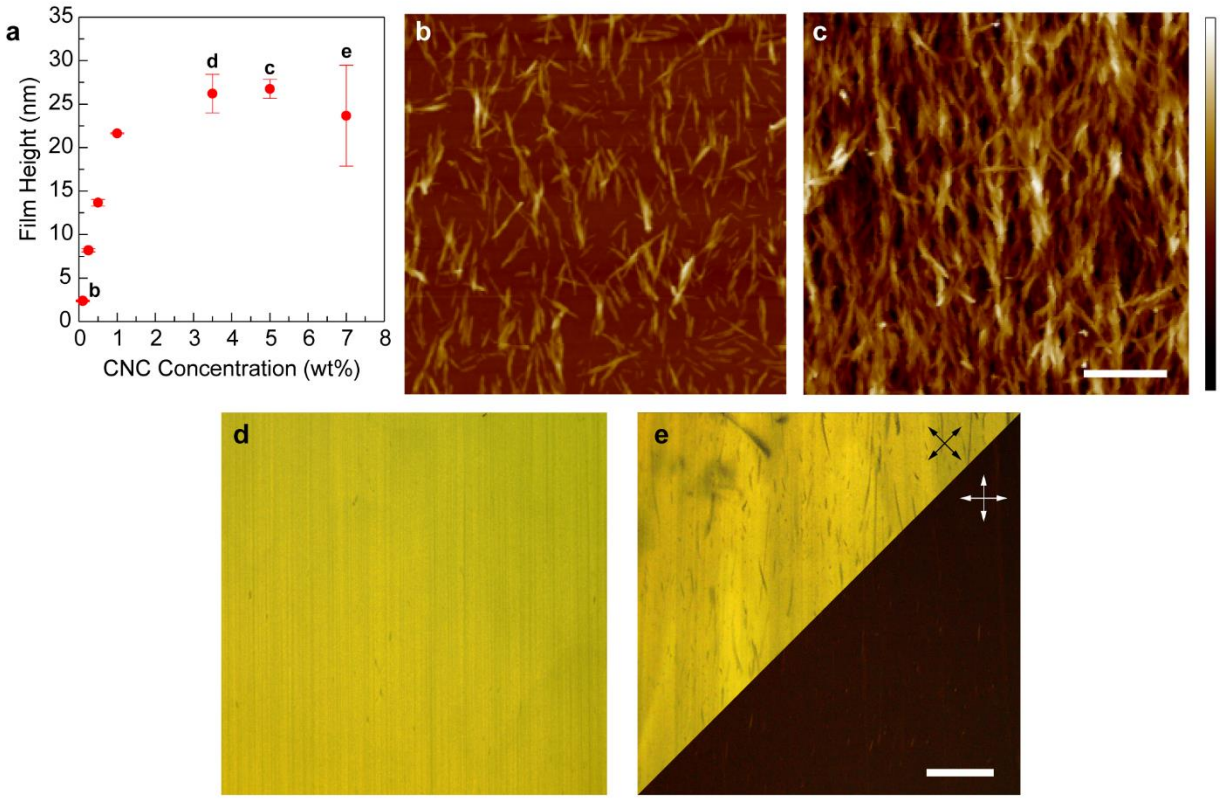


**Figure 6.3.** Effect of CNC concentration on CNC film morphology. (a) Film thickness versus CNC concentration at a constant volume of 1 mL. (b,c) AFM height scans of aligned CNC films fabricated using 1 mL of 0.1 and 5 wt%. Height scalebar at right of (c) is 65 nm and applies to (b) and (c). Scalebar in (c) is

500 nm and applies to (b) and (c). (d,e) POM images of aligned CNC film obtained with 3.5 (d) and 7 (e) wt% concentration. Scalebar in (e) is 250 µm and applies to (d) and (e). Data points corresponding to the AFM and POM images in (b-e) are also noted in (a).

**6.2.4 Effect of CNC solution volume on film thickness.** Another route to control the amount of CNC passing over the substrate, and in turn control the film thickness, is varying the solution volume. We study the effect of the CNC solution volume by varying the volume from 50 to 13,000 µL at constant concentration (3.5 wt%) and shear rate (19,000 $s^{-1}$). Similar to the concentration studies, the film thickness increases with volume until a thickness of approximately 20 nm is reached (**Fig. 6.4**). For example, the film thicknesses using 50 µL (**Fig. 6.4b**) and 1000 mL (**Fig. 6.4c**) of solution are 0.5 ± 0.1 nm (corresponding to submonolayer coverage) and 19.0 ± 0.7 nm, respectively.

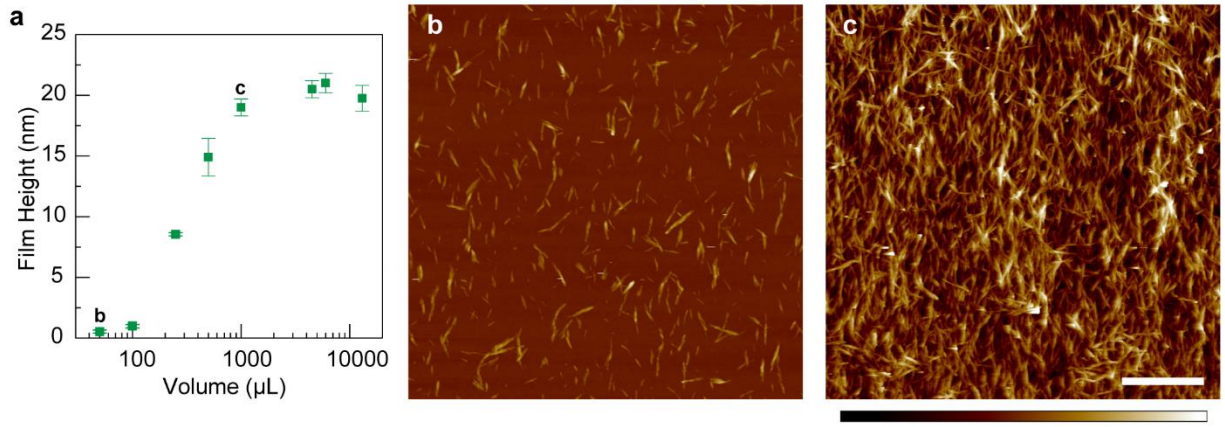


**Figure 6.4.** Effect of CNC solution volume on aligned film thickness. (a) Film thickness versus CNC solution volume at a constant concentration of 3.5 wt%. (b,c) AFM height scan of a film deposited with a solution volume of 50 uL (b) and 1000 mL (c). Data points corresponding to the AFM height images in (b) and (c) are indicated in (a). Scalebar in (c) is 1 um and applies to both (b) and (c). The height scalebar below (c) is 55 nm and applies to both (b) and (c).

**6.3 Conclusion.**

The alignment of CNCs into ultrathin films with control over the alignment and thickness has been difficult to accomplish. Here, we demonstrate solution-based shear is one route to achieve these desired films for coatings or material property studies of model films. The shear rate is controlled by varying the volumetric flow rate of the CNC solution, and a narrow HWHM of alignment of 33° is achieved using a

high shear rate of 19,000 $s^{-1}$. The alignment within the films is measured using a new analysis based on polarized Raman spectroscopy, which enables the degree of alignment to be easily and quickly quantified. Control over the film thickness is demonstrated through either varying the concentration (at fixed solution volume) or the solution volume (at fixed concentration). The film thickness is tuned from submonolayer to approximately 25 nm by increasing the concentration or volume of the CNC solution.

## 6.4 Materials and methods.

**6.4.1 Cellulose nanocrystal solutions.** Solutions of CNC at a concentration of 10.0 wt% in water are obtained from the Forest Products Laboratory in Madison, WI according to published procedure.[140] CNCs were prepared by spraying 64 wt% $H_2SO_4$, preheated to 45°C, to dissolving-pulp drylap that had been stripcut, packed into a glass-lined reactor and placed under vacuum. The acid and pulp slurry was maintained at 45°C with rapid mixing, under a nitrogen atmosphere, for 90 minutes. The hydrolysis treatment is terminated by 10 dilution in water. The aggregated CNCs are bleached for 30 minutes by adding $NaClO_2$ to the acidic solution before neutralizing with NaOH. The CNCs become colloidal when the sodium sulfate solution is displaced using tubular ultrafiltration equipped with 200,000 Dalton PVDF membranes. After removing any dirt and debris with a 50-micron filter, the CNCs are concentrated to 10 wt% solids using the same ultrafiltration equipment. The content of sulfur on dry CNCs is 1.06 wt%. The cellulose nanocrystals are 5-10 nm in diameter and ~150 nm long.

**6.4.2 Preparation of substrates.** Si wafers with 90 nm of dry, thermal oxide are used as target substrates. The substrates are cleaned with a piranha solution of $H_2SO_4$ (91 – 92.5%):$H_2O_2$ (30%) at a 2:1 ratio by volume at 110 °C for 1 h, rinsed with deionized water (resistivity ~18 MΩ), and dried with $N_2$. $SiO_2$/Si wafers are then treated with Surpass 4000, an adhesion promoter.

# Chapter 7. Summary and outlook

In this work, we explore and develop different routes for producing films of aligned carbon nanotubes for semiconductor electronics. Some of the major accomplishments discussed in this work are:

(1) Elucidation of the nanotube alignment mechanism and role of ink/water interface in FESA, and the demonstration of improved control over FESA film morphology (Chapter 2);
(2) Discovery that nanotubes that are collected and trapped at a liquid/liquid interface can form a 2D nematic liquid crystal assembly (Chapter 3);
(3) Development of a novel technique (TaFISA) for fabricating arrays of highly aligned (within ± 5.7°) nanotubes based on the understanding in (2) (Chapter 3);
(4) Uncovering that increasing flow, decreasing temperature, and increasing concentration are all routes for improving nanotube ordering in the TaFISA technique due to the underlying liquid crystal phenomena governing assembly (Chapter 3);
(5) Demonstration that the directed nature of the TaFISA technique enables the deposition and alignment to be performed on the wafer-scale (Chapter 3);
(6) Demonstration that the interfacial assembly of nanotubes at a liquid/liquid interface occurs with different solvents, polymer wrappers, and nanotubes, indicating the utility of this technique for the alignment of nanotubes with different chiralities for various applications (Chapter 4);
(7) Development of a new experimental setup and process for fabricating quasi-aligned nanotube films across $10 \times 10$ cm$^2$ substrates using confined shear-based alignment (Chapter 5);
(8) Discovery that confined, shear-based alignment (Chapter 5) can also be used to fabricate ultrathin films of aligned CNCs with control over degree of alignment and film thickness (Chapter 6).

There are multiple future research directions to further improve upon the results in this work, including:

(1) Demonstrate scaling of the TaFISA technique to align nanotubes uniformly across the entirety of a 10 cm round wafer as used in industry, as opposed to the majority of a 10 cm wafer piece, discussed in Chapter 3.
(2) Further reduce liquid crystal defects observed in TaFISA films, as explored in Chapter 3, through improvements in nanotube ink homogeneity (e.g., reduce nanotube length polydispersity, prevent bundles, eliminate aggregates, etc.).
(3) Explore additional combinations of polymer wrappers and ink solvents in the TaFISA process to determine the limitations of the 2D liquid crystal nematic assembly at liquid/liquid interfaces.
(4) Study nanotube collection and ordering at the ink/water interface *in situ* using interface sensitive and polarization dependent spectroscopies could shed light on the thermodynamics and kinetics of nanotube liquid crystal assembly at liquid/liquid interfaces (Chapter 3,4).
(5) Compared to the results in Chapter 3, improve FET performance through the reduction of bundles, increase in packing density, and improvement in film uniformity.
(6) For nanotubes deposited via shear-based alignment (Chapter 5), study the effects of degree of alignment and channel dimensions on FET performance to determine the optimum alignment for applications requiring different channel lengths.

Further improvements along these lines promise to make aligned films of nanotubes deposited via the alignment processes developed in this work, TaFISA and confined, shear-based alignment, attractive for industrial electronics.

# **Appendix A.** Supporting information for Chapter 2

Appendix A was adapted with permission from Jinkins, K. R., Chan, J., Brady, G. J., Gronski, K. K., Gopalan, P., Evensen, H. T., Berson, A., & Arnold, M. S. Nanotube Alignment Mechanism in Floating Evaporative Self-Assembly. *Langmuir* **33**, 13407-13414 (2017).  K.R.J. fabricated the samples and performed the experiments and data processing for the Dose FESA experiments. J.C. and A.B. developed the MATLAB analysis code for tracking the contact lines. G.J.B., K.K.G., and H.T.E. performed the preliminary back-imaging experiments. G.J.B. and H.T.E. performed the stationary FESA (**Fig. 2.1**) and the deposition from a thick, stagnant layer of nanotube ink experiments (**Fig. A9**). M.S.A. and A.B. supervised the work. All authors contributed to data interpretation. K.R.J. drafted the manuscript, and all authors discussed and revised it.

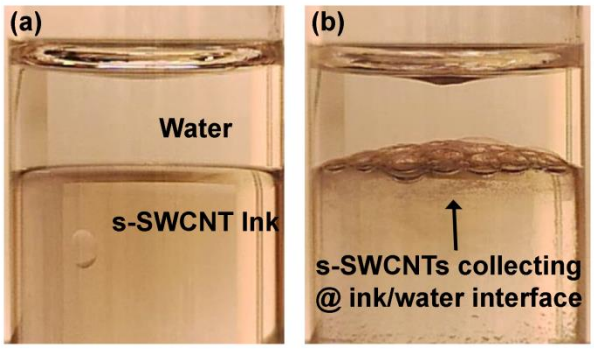


**Figure A1**. Initially, 5 mL of deionized water is layered on 10 mL of 1 µg $mL^{-1}$ nanotube ink (a). After 5 s of gentle shaking by hand, the mixture is allowed to settle. After 60 s, we clearly see the nanotubes collecting and confining at the ink/water interface (b). Bubbles of ink in water or water in ink are also seen at the ink/water interface in (b). While the bubbles make it difficult to observe the ink/water interface prior to 60 s, we expect that assembly of nanotubes at this interface occurs almost instantaneously.

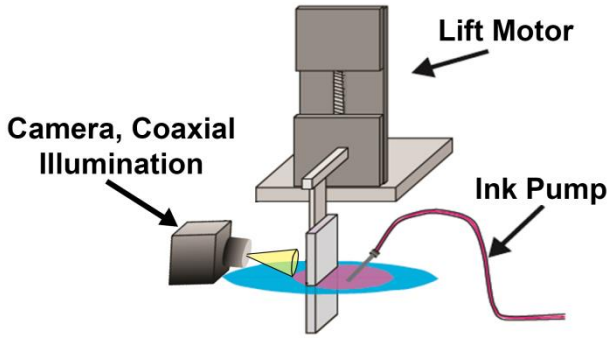


**Figure A2**. Back-imaging setup to image contact lines during FESA deposition. A camera is used to image the deposition through a transparent quartz substrate with coaxial illumination. The back of the substrate is coated with a film of PTFE to suppress the water contact line to more clearly see the contact line behavior on the front of the substrate. The substrate is lifted out of the water at a constant lift rate to record the contact line dynamics of multiple pulses over ~5 s time frame.

**A.1 Alignment characterization with polarized Raman spectroscopy.**

Polarized Raman spectroscopy is used to quantify the degree of nanotube alignment, using the Dose FESA 10 μg $mL^{-1}$ sample in **Fig. 2.4a** and **Fig. A11c** as a representative sample. Raman (Aramis Horiba Jobin Yvon Confocal Raman Microscope, laser excitation wavelength of 532 nm) spectra are collected with a horizontally polarized incident laser and horizontal analyzer orientation (HH) aligned with the long axis of the aligned nanotubes. This measurement yields the strongest Raman peak intensity of the G-band. With no rotation of the sample, the polarization of the incident laser and analyzer are adjusted to both be vertical (VV). From the ratio of the HH and VV G-band intensities, the optical anisotropy is calculated.[21,46,141] The spectra are shown along with a representative SEM of the sample in Fig. S4. Each of the HH and VV spectra are normalized to the Si peak at ~520 $cm^{-1}$. The ratio of the G-band intensity at the HH condition with respect to the VV condition (i.e., the optical anisotropy) is 409. Assuming the nanotubes are oriented within a Gaussian angular distribution, this anisotropy equates to a distribution with an angular width of $\sigma = 9.8°$. This distribution is on the same order of the $\sigma = 14.4°$ measured by Joo et al., for arc-discharge nanotubes aligned via FESA.[46] Joo et al. also showed that σ increased to 31° for smaller diameter nanotubes (produced by the HiPco method). These two types of nanotubes were of similar length, indicating that the improved alignment of the larger diameter nanotubes can be ascribed to the increased structural rigidity of the larger diameter nanotubes.[46]

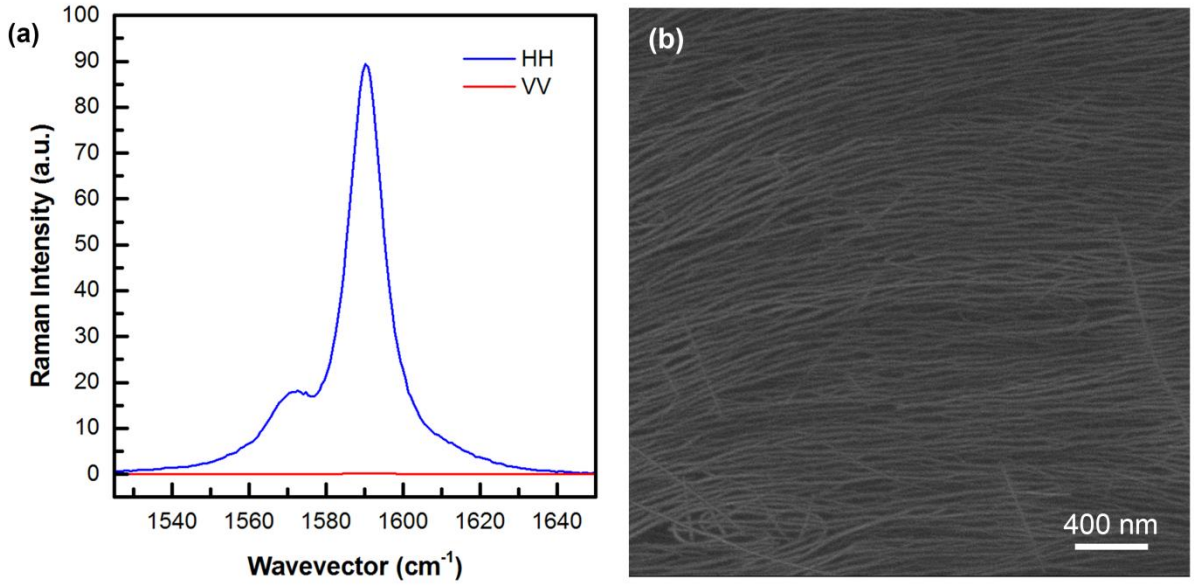


**Figure A3**. (a) Raman spectra of the G-band of the 10 μg $mL^{-1}$ FESA film (sample from data in **Fig. 2.4a**, Fig. S11c), normalized to the Si peak at ~520 $cm^{-1}$. HH and VV polarizations of the incident Raman laser and the analyzer are shown, with the HH polarization oriented with the long-axis of the aligned film. (b) Representative SEM from the 10 μg $mL^{-1}$ sample.

**A.2 Calculation of chloroform evaporation rate.**

The chloroform evaporation rate is determined using a steady-state experiment in which a constant volumetric flow rate, *Q*, of chloroform is added to the surface of the aqueous subphase until a steady-state, circular pool of chloroform of area, *A*, is established from which the evaporation rate must also be *Q*. Using a *Q* of 80 µL $min^{-1}$, a steady-state pool of chloroform, with roughly constant radius of ~5 mm, is established on the water surface. The evaporation rate, *Q*/*A*, is estimated to be 17.3 µm $s^{-1}$. Using this calculation, in the time between doses, 1.2 s, 20.4 µm of chloroform evaporates.

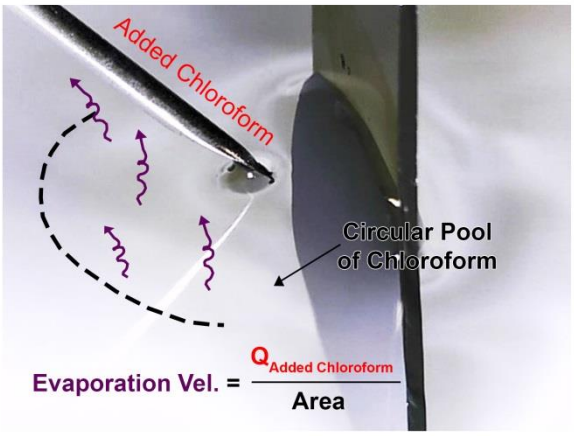


**Figure A4**. A steady-state pool of chloroform is established at the water/substrate interface. At steady-state, the volumetric flow rate of added chloroform is balanced by the evaporation rate multiplied by the area of the circular pool.

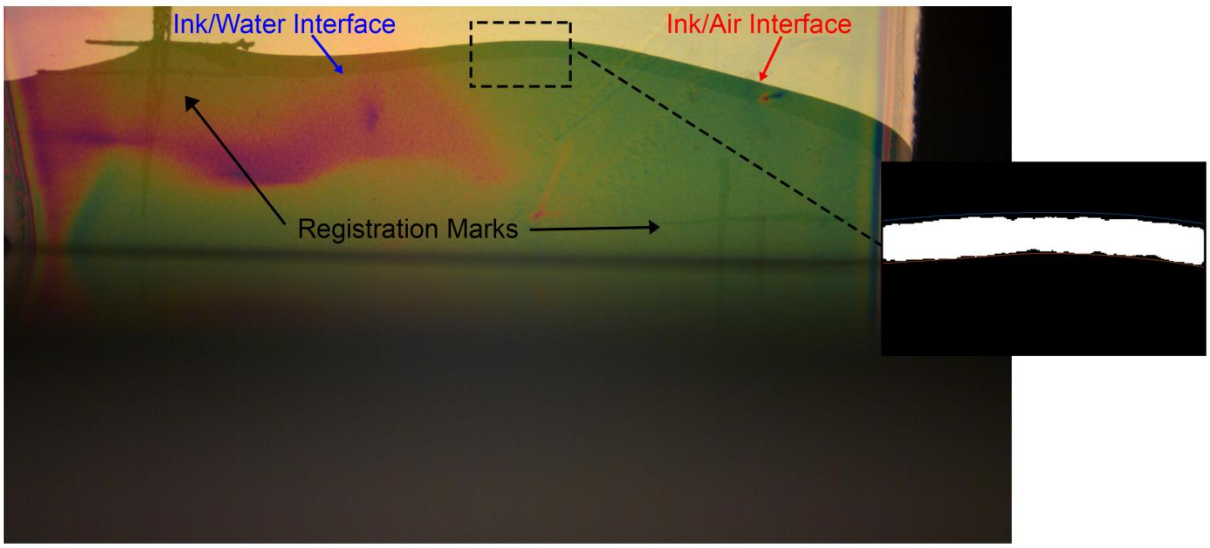


**Figure A5**. Example image from back-imaging video. Ink/water and ink/air interfaces are indicated. Registration marks are used to correlate the video with actual deposition on the substrate. Inset shows the binary crop of the approximate area indicated in the video image, where the ink layer shows in white.

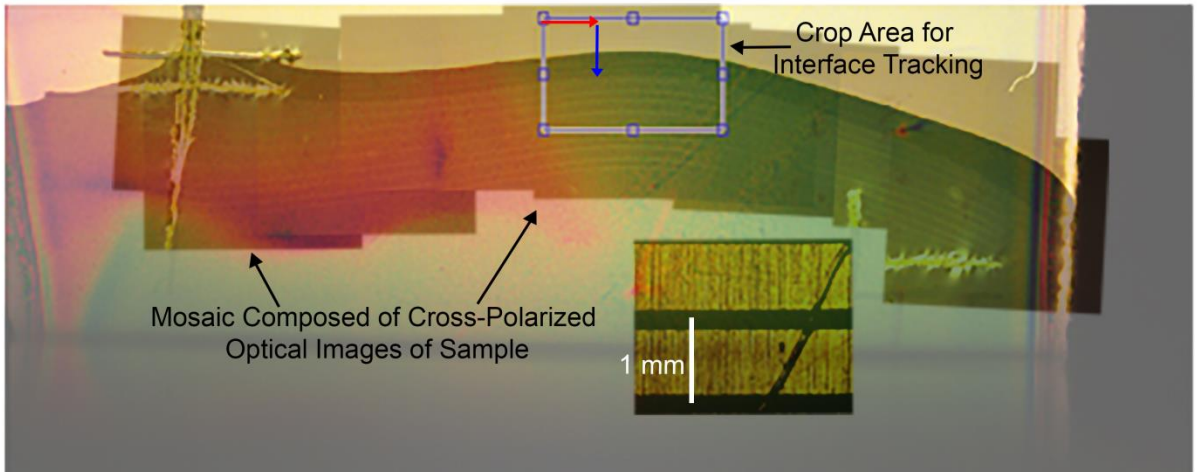


**Figure A6**. Example of contact line tracking and nanotube band position registration. Scratch marks on the quartz substrate provide a means for registering cross-polarized optical microscopy images of the aligned nanotube bands with respect to the video tracking of the contact line positions. Several cross-polarized optical microscopy images are stitched together to form a mosaic and overlaid with the first frame of the video series. The gold and black inset at the bottom of the figure is an optical image of a ruler and shows the length scale used for the calibration procedure.

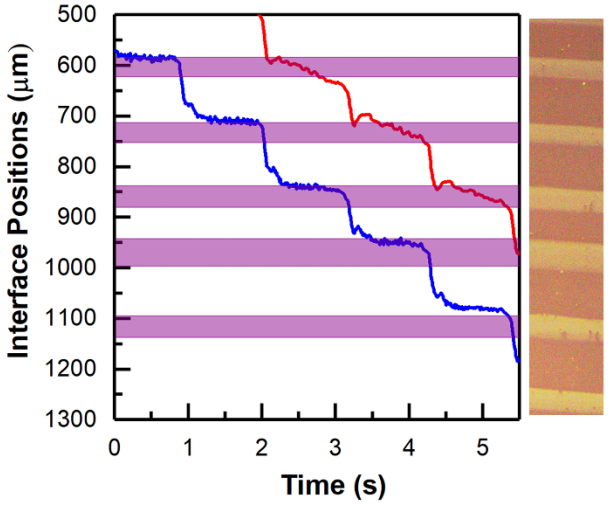


**Figure A7**. Traces of ink/water/substrate and ink/air/substrate contact lines correlated with a cross-polarized optical microscopy image for the experiment shown in **Fig. A6**.

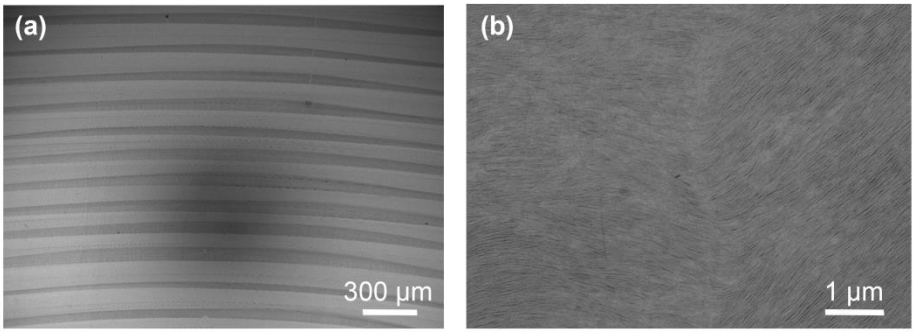


**Figure A8**. (a-b) SEM micrographs from Dose FESA deposition in a near chloroform vapor saturated environment. The alignment (b) is similar to that seen in previous work[46] and in this work (**Fig. 2.1d, Fig. 2.4b, Fig. 2.5c**).

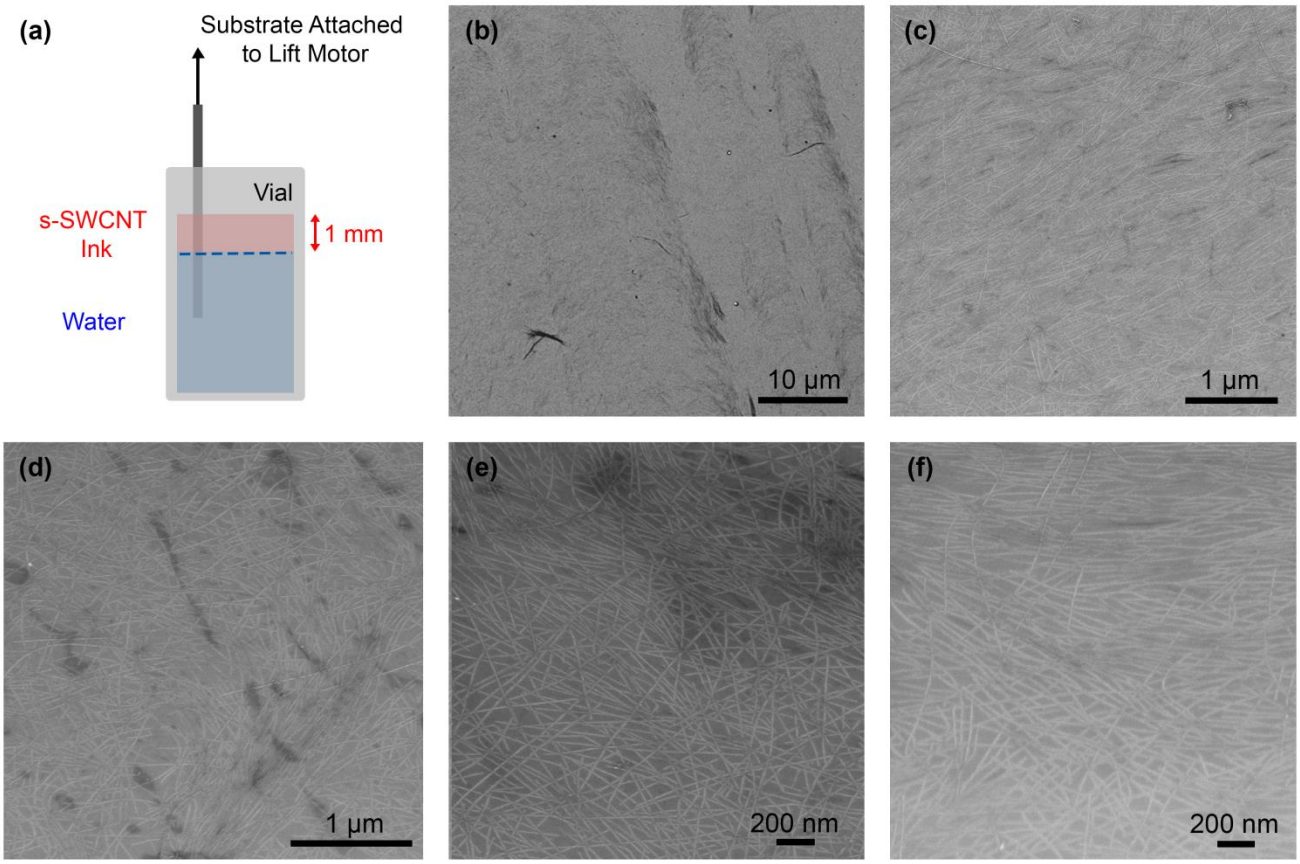


**Figure A9**. Isolating the role of flow and evaporation in FESA. (a) A substrate is suspended in a water subphase in a small vial. After the substrate is in place, a thick (~1 mm) layer of 10 µg $mL^{-1}$ nanotube ink is gently added on the water. The substrate is translated through the ink/water interface. (b-f) SEM micrographs from the area below the initial location of the ink/water interface. The nanotube deposition is not uniform (shown in b) and regions of randomly aligned (d,e) and partially aligned (c,f) nanotubes are present.

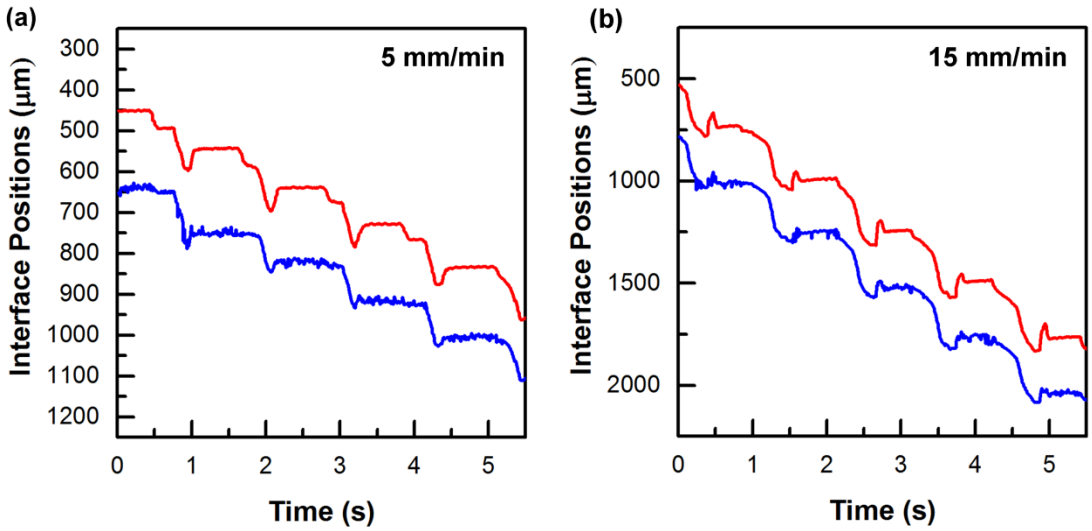


**Figure S10**. Back-imaging traces, plotted in the frame of the substrate, of depositions with 5 and 15 mm $min^{-1}$ lift rates, (a) and (b) respectively. As shown, the faster lift rate simply serves to translate the substrate farther before the new pulse of ink is introduced – this is seen in that the drops caused by pinning and depinning are ~500 µm with a lift rate of 15 mm $min^{-1}$, as compared to a drop of ~100 µm for the slower lift rate of 5 mm $min^{-1}$.

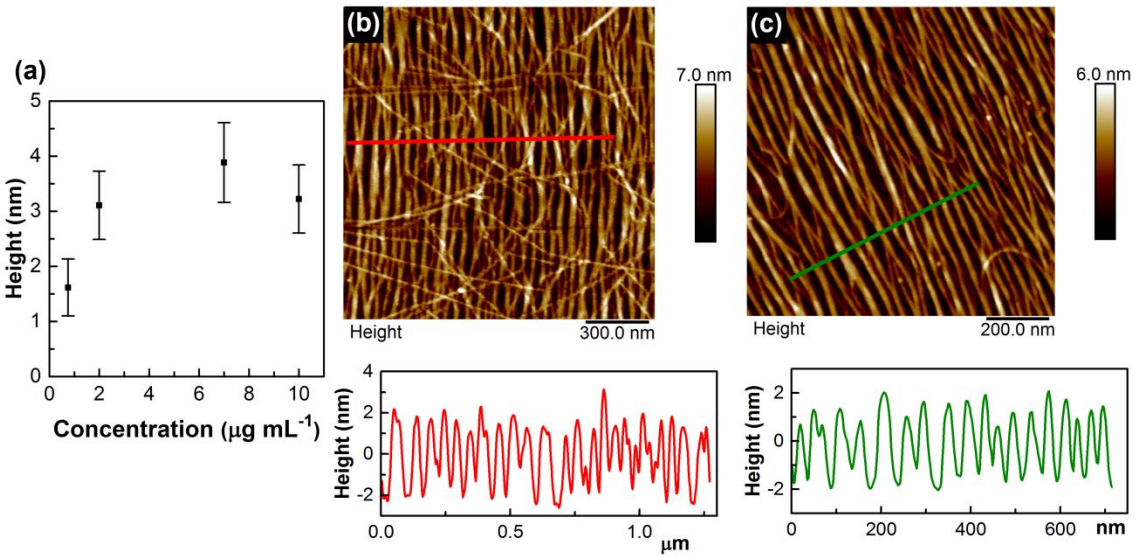


**Figure A11**. (a) AFM (Bruker Nanoscope V) height measurements of FESA aligned nanotubes on $SiO_2$ from the concentration series shown in **Fig. 2.4a**. (b) and (c) show representative AFM images and cross-section profiles from the 7 and 10 μg $mL^{-1}$ samples, respectively. As shown in (a), the measured height of FESA films saturates above 1 μg $mL^{-1}$.

# **Appendix B.** Supporting information for Chapter 3

Appendix B was adapted from Jinkins, K. R., Saraswat, V., Jacobberger, R. M., Berson, A., Gopalan, P., & Arnold, M. S. 2D Nematic Carbon Nanotube Assemblies Aligned by Flow. *In preparation.* (2020). K.R.J. and M.S.A. performed all experiments, data collection, and analysis. V.S. fabricated graphene control samples for normalization of Raman measurements (**Fig. 3.1g-i**). R.M.J. performed all 400 °C vacuum anneals on nanotube films measured using Raman spectroscopy (**Fig. 3.1g-i**) and films used for devices (**Fig. 3.5**) M.S.A., P.G., and A.B. supervised the work. All authors contributed to data interpretation. K.R.J. drafted the manuscript.

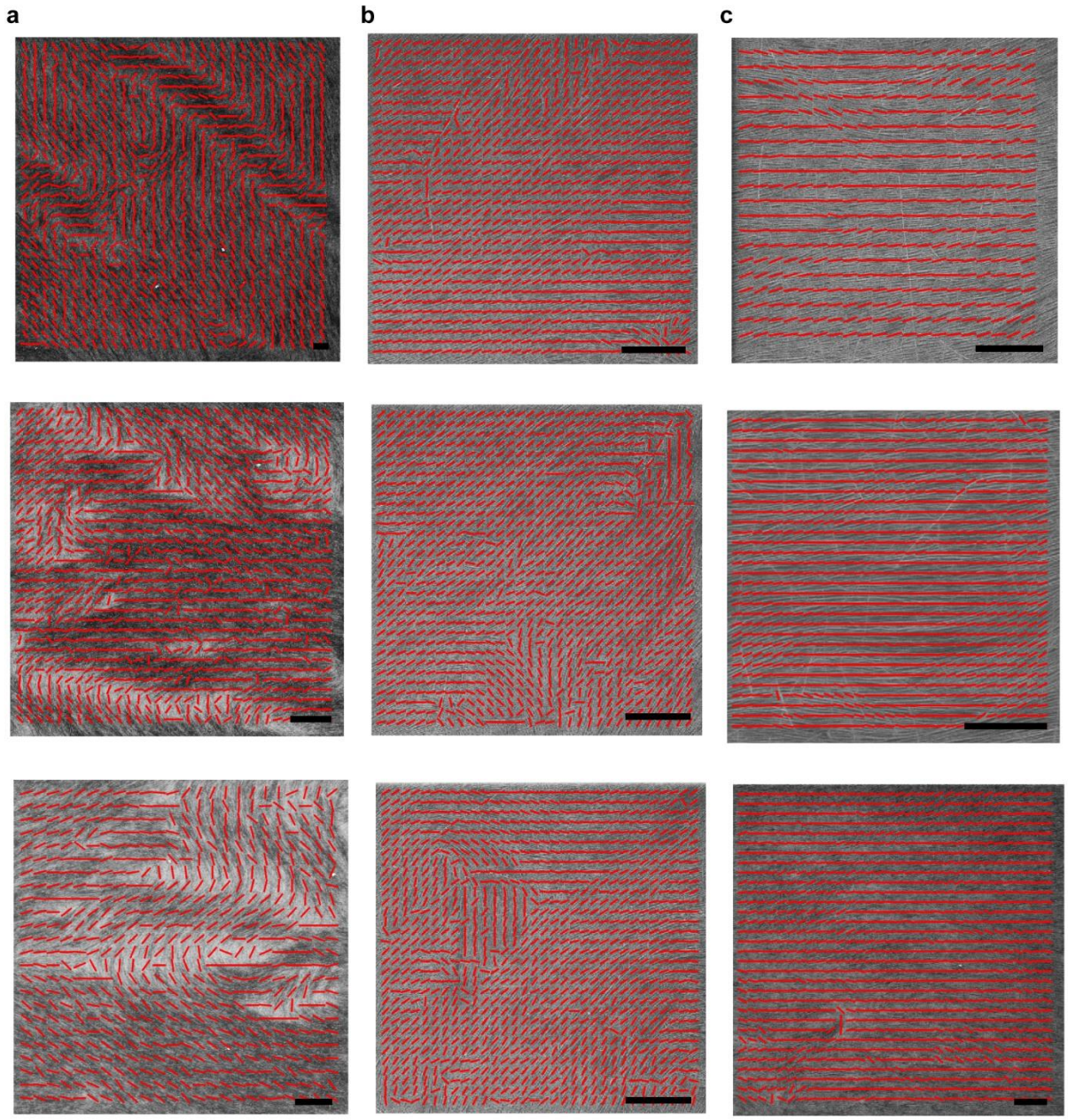


**Figure B1.1.** SEM images from tangential flow interfacial self-assembly (TaFISA) films obtained at 0 (a), 1 (b), and 4 (c) mL $min^{-1}$ analyzed with two-dimensional fast Fourier transforms. Local director orientations are shown overlaid on the scanning electron microscopy (SEM) images as red lines. Scalebars are 1 μm.

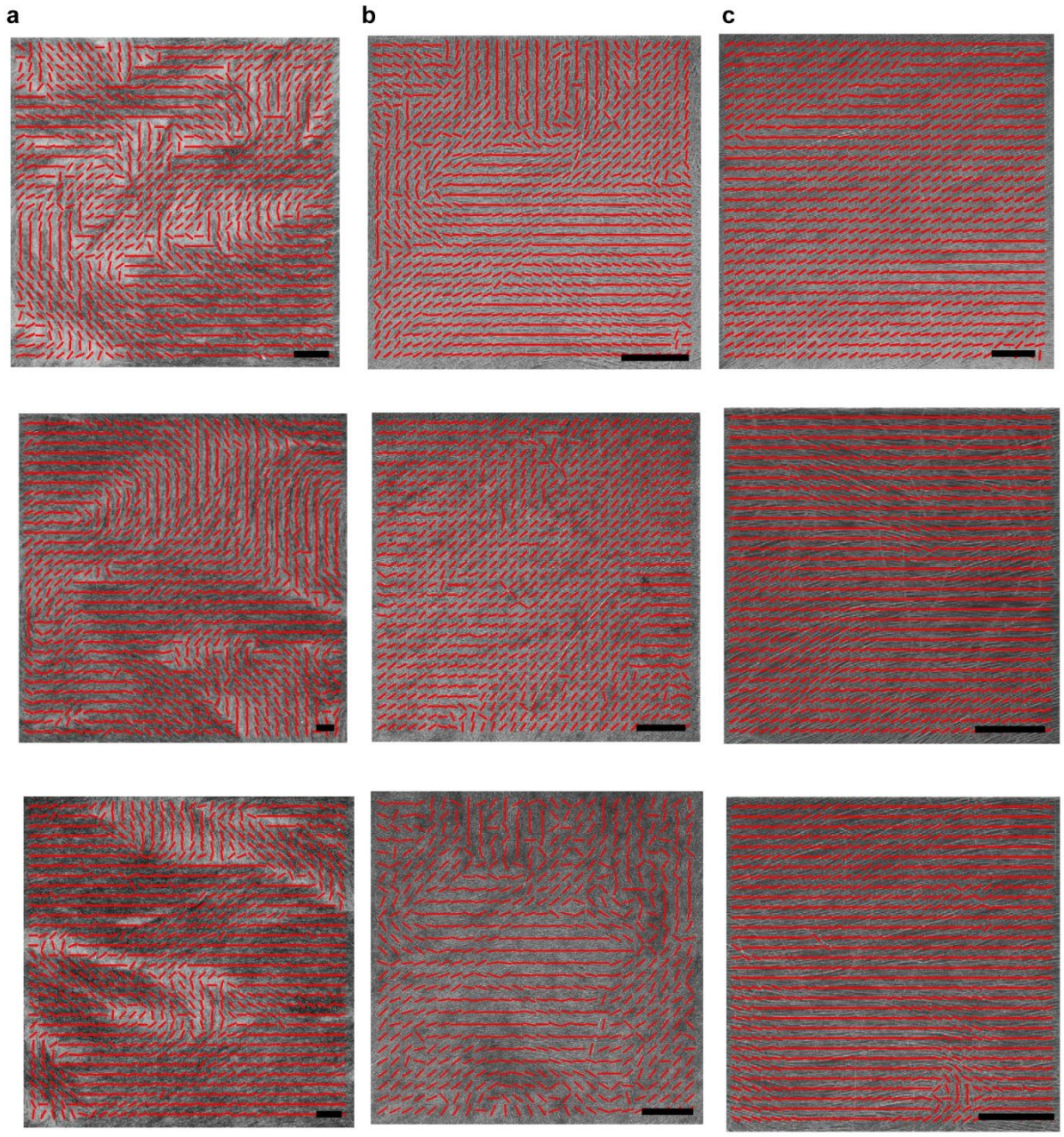


**Figure B1.2.** SEM images from tangential flow interfacial self-assembly (TaFISA) films obtained at 0 (a), 1 (b), and 4 (c) mL $min^{-1}$ analyzed with two-dimensional fast Fourier transforms. Local director orientations are shown overlaid on the scanning electron microscopy (SEM) images as red lines. Scalebars are 1 μm.

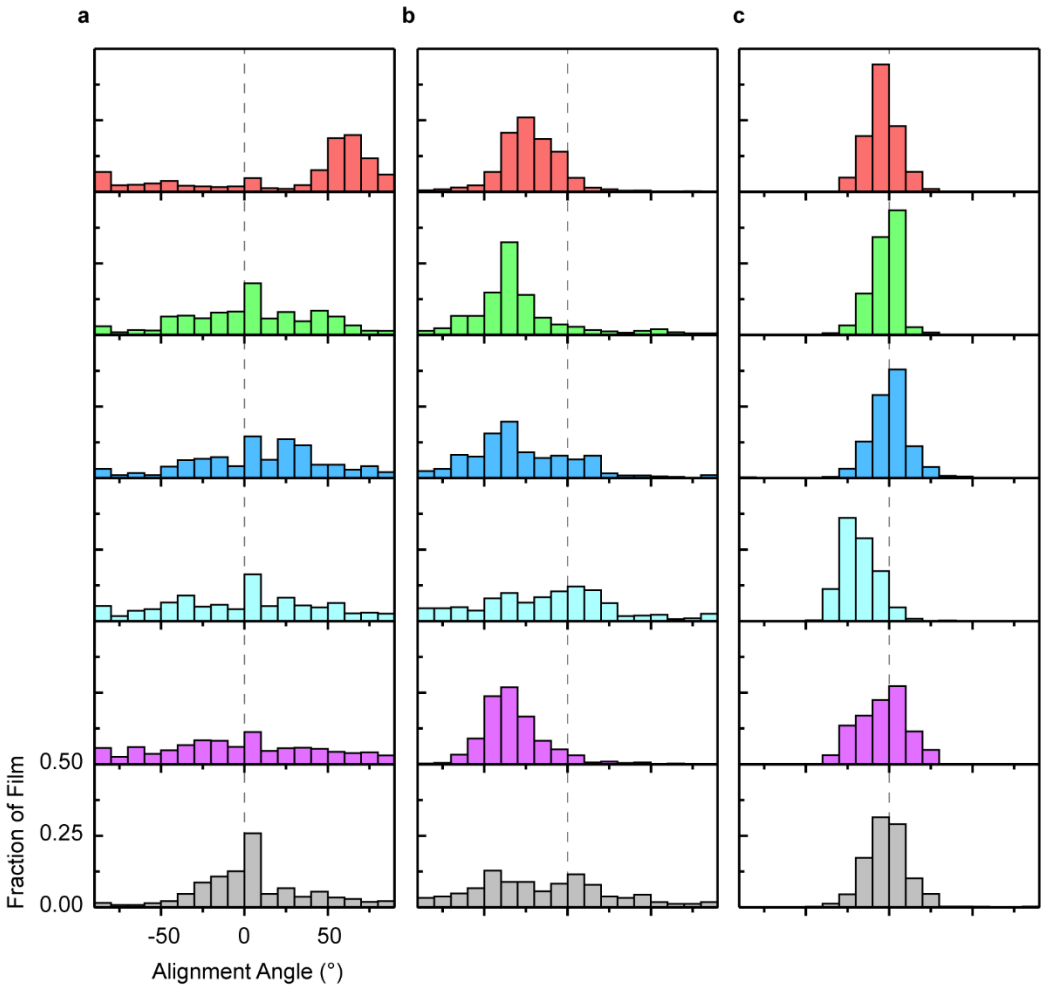


**Figure B2.** Histograms of director orientations from TaFISA films shown in SEM images in **Fig. B1**, where columns (a), (b), and (c) correspond to volumetric flow rates 0, 1, and 4 mL $min^{-1}$.

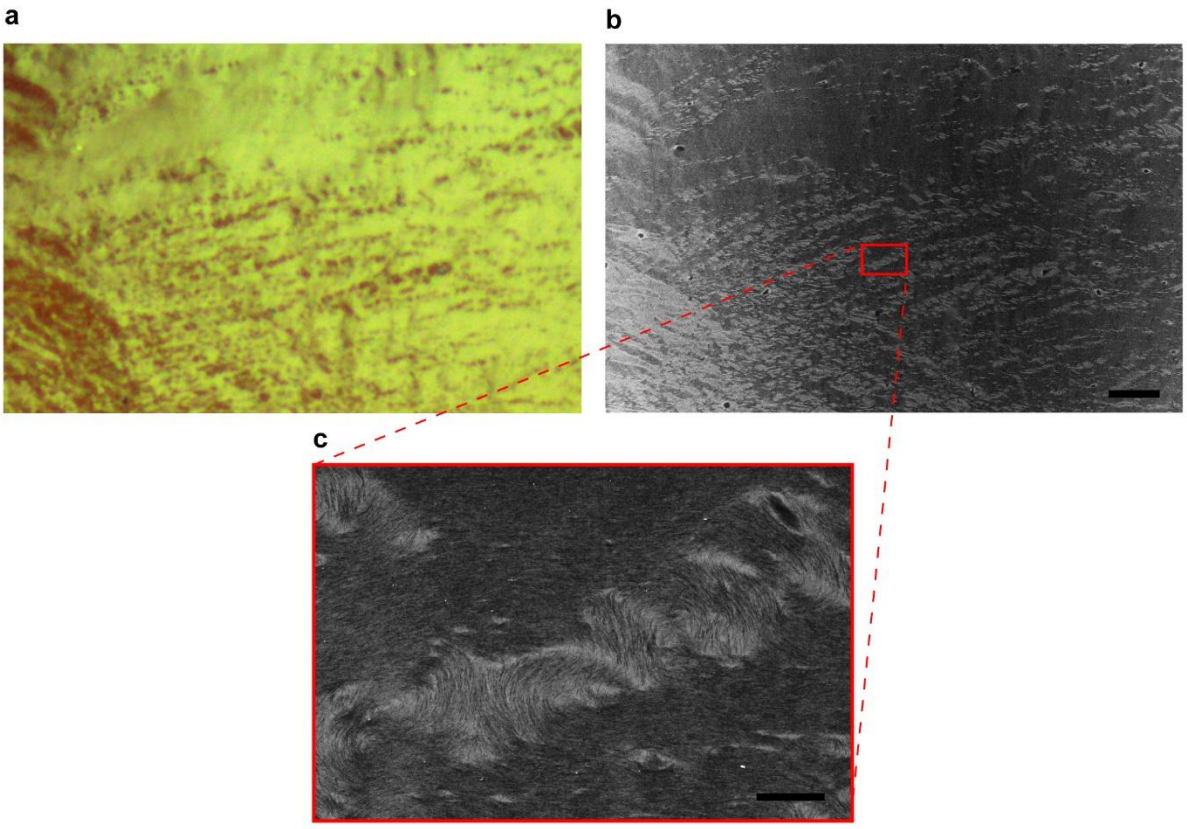


**Figure B3.** Comparison between polarized optical microscopy (POM) and SEM showing that density can also be lower in darker regions of the POM images. (a) POM image of TaFISA film obtained without flow. (b) SEM of region shown in (a). Scalebar is 50 μm and applies to (a) and (b). (c) Magnified view of local region in (a) and (b). Scalebar is 5 μm.

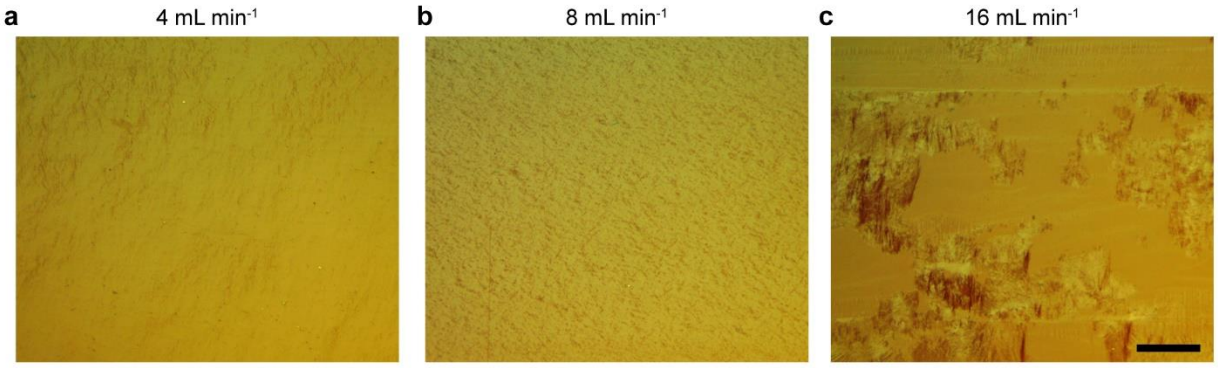


**Figure B4.** POM images from TaFISA films at volumetric flow rates 4 (a), 8 (b), and 16 (c) mL $min^{-1}$. Scalebar is 250 µm and applies to (a-c).

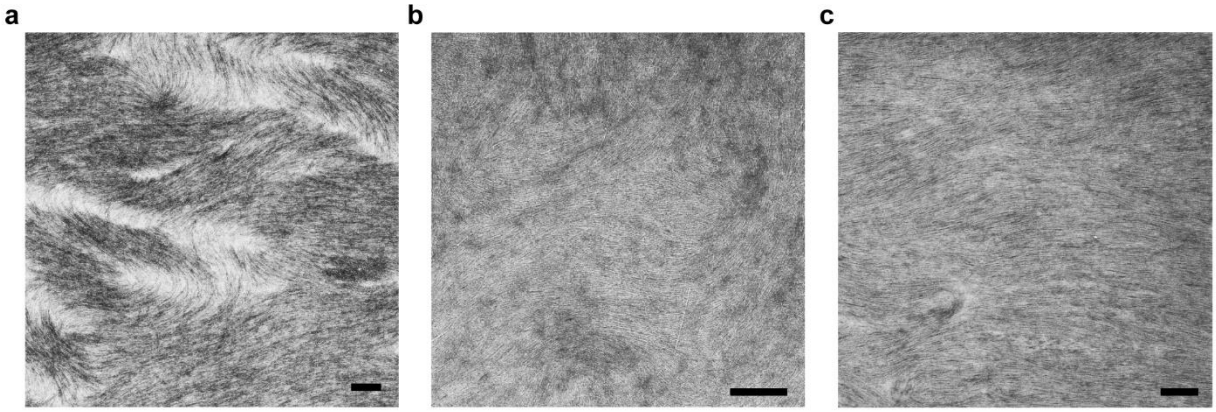


**Figure B5.** SEM images from **Fig. 3.2a-c** without local directors overlaid. Scalebars are 1 μm.

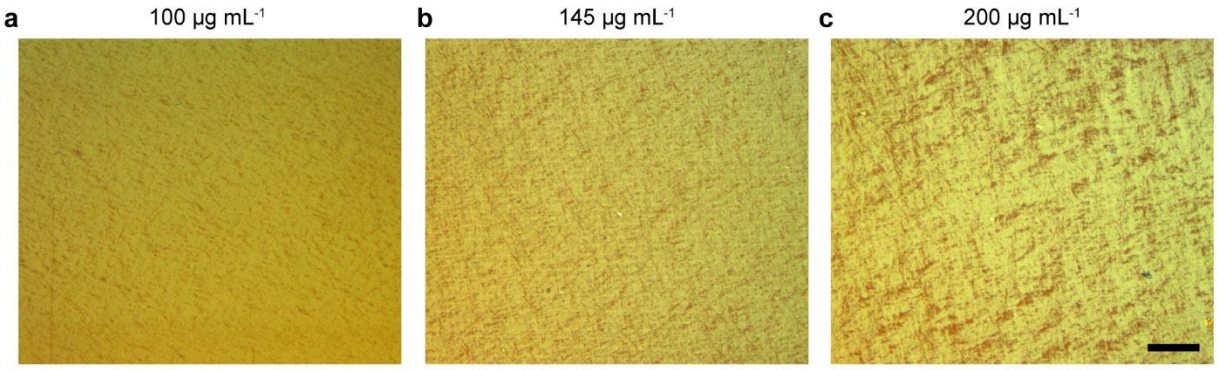


**Figure B6**. POM images from TaFISA films at ink concentrations: 100 (a), 145 (b), and 200 (c) µg $mL^{-1}$. Scalebar is 250 µm and applies to (a-c).

**B.1 Calculation of onset of liquid crystal phase according to Onsager's rigid rod theory.**

According to Onsager's rigid rod theory,[85] the onset of the nematic phase for lyotropic liquid crystals occurs at a concentration expressed by:

$$c_{N\_Rigid} = 3.34\rho\frac{D}{L}$$

where $D$ and $L$ are the nanotube diameter and length, respectively and $\rho$ is the average nanotube density. The average diameter, length, and density of the nanotubes used in this work are: 1.5 nm, 500 nm, and 1.33 g mL$^{-1}$ (calculated from the nanotube dimensions) respectively. Using these values, the concentration $c_{N\_Rigid} = 13.3$ mg mL$^{-1}$.

As seen in the SEM images in **Fig. 3.1d-f**, the nanotubes are not infinitely rigid and do bend slightly. This bending can affect the concentration for the onset of the liquid crystal phase and for persistent semiflexible rods (i.e., where the persistence length ($\ell$) is much greater than the nanotube length: $\ell \gg L \gg d$) the nematic concentration onset is given by[86]:

$$c_{N\_Semiflexible} = 10.48\rho\frac{D}{L}.$$

Using the same $D$, $L$, and $\rho$ above, the concentration $c_{N\_Semiflexible} = 31.7$ mg mL$^{-1}$ for persistent semiflexible rods. Likely, for the nanotubes used in this study, the nematic phase onset would be at a concentration between $c_{N\_Semiflexible}$ and $c_{N\_Rigid}$ , however, here we use $c_{N\_Rigid}$ as a lower bound to the nematic phase onset concentration.

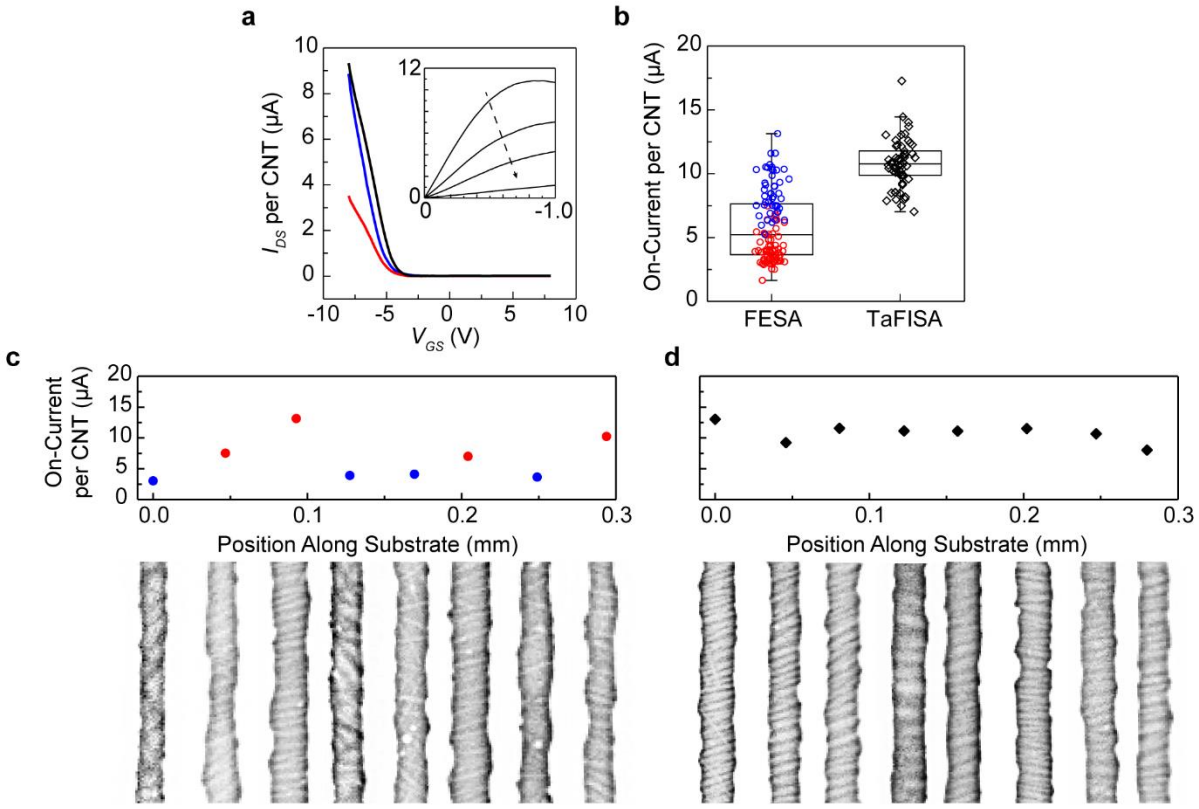


**Figure B7**. Charge transport measurements per nanotube (CNT) of FETs fabricated on FESA and TaFISA carbon nanotube arrays. (a) $I_{DS}$ versus $V_{GS}$ curves for representative TaFISA (black) and FESA (aligned – red, unaligned – blue) FETs measured at $V_{DS}$ of –1 V. Inset: $I_{DS}$ per nanotube versus $V_{DS}$ curves as $V_{GS}$ is varied from –8 to –2 V (top to bottom) in 2 V steps. (b) On-current per nanotube of all FESA and TaFISA FETs measured at $V_{DS}$ of –1 V. (c) On-current per nanotube versus position across the substrate for selected individual FESA FETs. The channels of the FETs in each data point are shown directly below in the SEM images. From left to right, the channel lengths are: 93, 100, 118, 115, 113, 124, 111, and 95 nm. (d) On-current per nanotube versus position along the substrate for individual TaFISA FETs. The charging effects vary, causing the nanotubes to appear different in each image. From left to right, the channel lengths are: 114, 121, 126, 120, 101, 127, 129, and 134 nm.

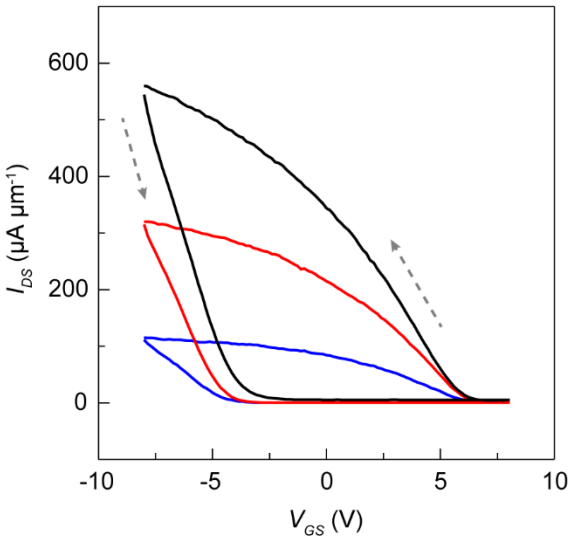


**Figure B8.** Full sweeps (forward—negative to positive $V_{GS}$ and reverse—positive to negative $V_{GS}$) of $I_{DS}$ versus $V_{GS}$ from the data shown in **Fig. 3.5b**. Black, red, and blue data correspond to FETs fabricated on TaFISA, aligned FESA, and unaligned FESA regions, respectively. Hysteresis is observed, likely due to adsorbed oxygen and water molecules or charge traps in the oxide.

# **Appendix C.** Supporting information for Chapter 4

Appendix C was adapted from Jinkins, K. R., Dwyer, J. H., Suresh, A., Gopalan, P., & Arnold, M. S. Parameters Affected Interfacial Assembly and Alignment of Nanotubes. *In preparation*. (2020). K.R.J. and M.S.A. performed all experiments, data collection, and analysis. J.H.D., A.S., and P.G. prepared self-assembled monolayer and polymer surfaces and measured water contact angles in **Fig. 4.3c,e-h**. J.H.D. and P.G. suggested the addition of glycerol to the water subphase (**Fig. 4.4**). M.S.A. and P.G. supervised all experiments. K.R.J. drafted the manuscript.

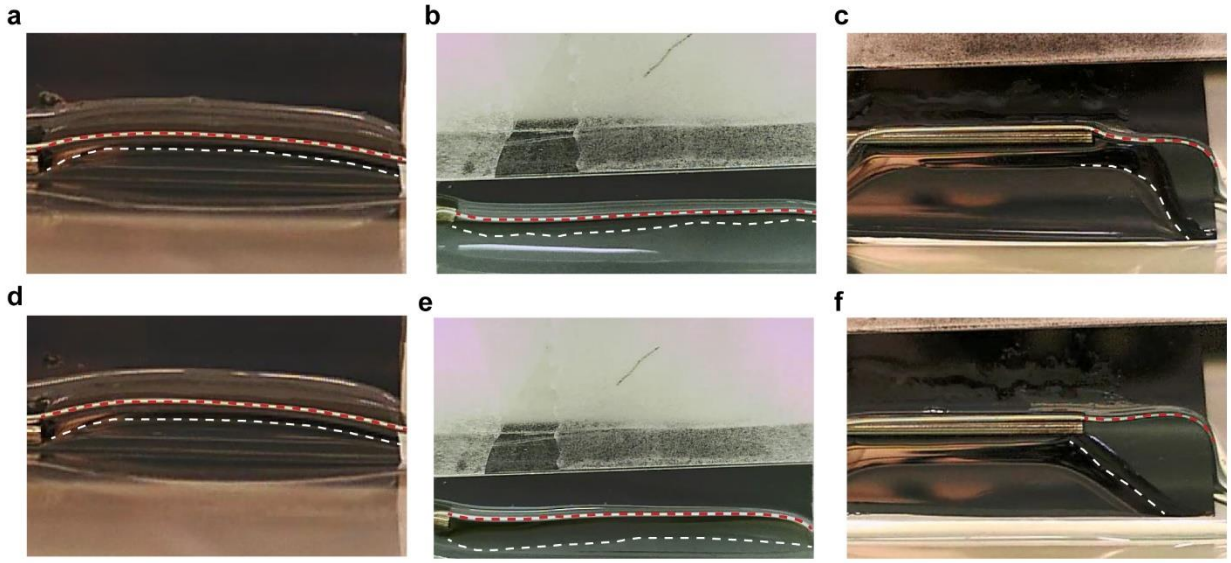


**Figure C1.** Effect of nanotube ink solvent on ink flow dynamics during TaFISA. Screenshots from video at beginning (a-c) and near end (d-f) of TaFISA depositions using nanotube ink with chloroform (a,d), toluene (b,e), and ODCB (c,f) solvents. All images are at approximately the same magnification. The ink/water and air/ink interfaces are outlined in dashed white and red lines, respectively, to indicate the approximate thickness of the ink layer.

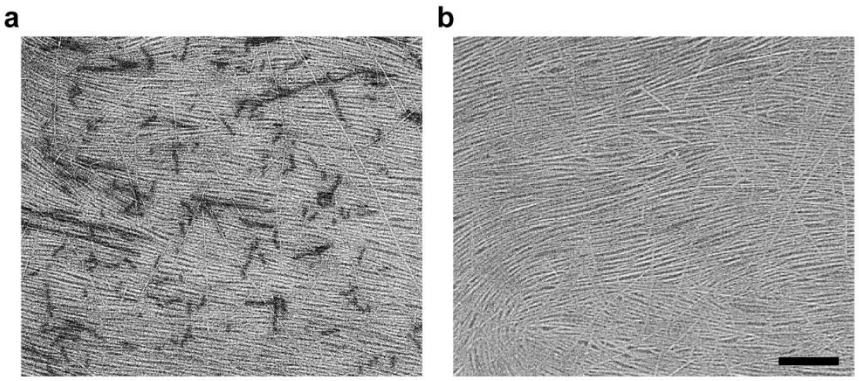


**Figure C2.** Effect of toluene boil to remove free polymer on nanotube films. (a) Before and (b) after boiling the sample in toluene at 120 °C for 1 h to remove free polymer (i.e., the black spots) decorating the film.

# **Appendix D.** Supporting information for Chapter 5

Appendix D was adapted with permission from Jinkins, K. R., Chan, J., Jacobberger, R. M., Berson, A., & Arnold, M. S. Substrate-Wide Confined Shear Alignment of Carbon Nanotubes for Thin Film Transistors. *Adv. Electron. Mater.* **5**, 1800593 (2019). Copyright (2018) WILEY-VCH. K.R.J. and M.S.A. performed all experiments, data collection, and analysis. K.R.J. designed and fabricated the standard confined shear-based alignment apparatus. J.C. fabricated the larger experimental apparatus for depositing aligned nanotubes across 10 cm substrates (used in **Fig. 5.5**) and R.M.J. measured the interior roughness of these shear alignment setups with interferometry. M.S.A. and A.B. supervised the work. All authors contributed to data interpretation. K.R.J. drafted the manuscript, and all authors discussed and revised it.

## D.1 Shear rate calculation assuming a planar Poiseuille flow and symmetric parabolic velocity profile in a rectangular channel.

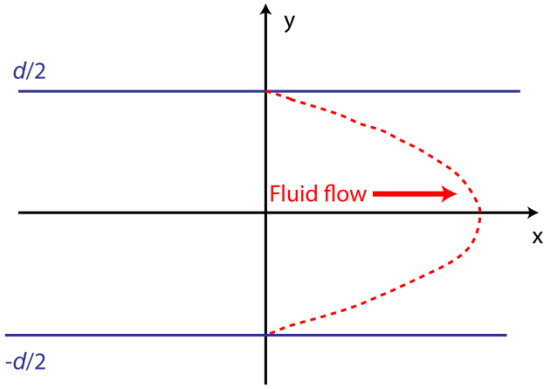


**Figure D1**. Schematic of fluid flow used for calculation of shear rate. The channel is assumed to be infinitely extending along the z-direction and the blue lines at $-d/2$ and $d/2$ indicate the top and bottom channel walls.

We assume fluid flowing through a rectangular channel. The fluid is flowing in the x-direction and the walls are infinitely large in the z-direction – a simplified schematic of this scenario is shown in **Fig. D1**.

An approximate fluid velocity profile is indicated by the red dashed line. For fluid flowing in the x-direction and assuming no slip conditions at the channel walls, the velocity as a function of position perpendicular to the channel in the y-direction is given as

$$V_x(y) = V_{max} - \frac{\Delta P}{2\,\mu\,L}\left[\frac{d^2}{4} - y^2\right] \tag{D.1}$$

where $V_{max}$ is the maximum flow velocity at the center of the channel, μ is the viscosity of the fluid, $L$ is the length of the channel, $d$ is the characteristic length of the rectangular channel cross-section, and $\Delta P$ is the pressure difference across the length of the channel. This pressure difference is given as

$$\Delta P = \frac{Q}{w}\frac{12\,\mu\,L}{d^3} \tag{D.2}$$

where $Q$ is the volumetric flow velocity, $w$ is defined as the width of the channel, and all other variables are as stated previously. The shear rate at the wall can be determined from the derivative of Equation 1 evaluated at the wall of the channel (i.e., y = *d*/2)

$$\frac{dV_x}{dy}\left(\frac{d}{2}\right) = \frac{\Delta P}{\mu\,L}\left[\frac{d}{2}\right] = \frac{6Q}{d^2 w} \tag{D.3}$$

and has units of $s^{-1}$. The maximum Reynold's number in this work is 467, calculated assuming chloroform density and viscosity, so the planar Poiseuille flow assumption in this calculation is valid.

**D.2 Alignment characterization via polarized Raman spectroscopy.**

Polarized Raman spectroscopy is used to quantify the degree of alignment within the nanotube films. The polarization angular ($\theta$) dependence of the nanotube Raman intensity ($I$) can be approximated by a $\cos^4(\theta)$ function,

$$I = A\cos^4(\theta) \tag{D.4}$$

where $\theta$ is the angle between the incident excitation polarization and the axis of the nanotube (in the plane perpendicular to the incident excitation's Poynting vector). The $cos^4(\theta)$ term arises from utilizing both a polarized incident laser and an analyzer oriented in the same direction as the laser polarization.[1] We assume the nanotubes within the film are oriented within a wrapped normal distribution

$$f(\theta;\mu,\sigma) = \frac{1}{\sigma\sqrt{2\pi}}\sum_{k=-\infty}^{\infty} exp\left[\frac{-(\theta-\mu+2\pi k)^2}{2\sigma^2}\right] \tag{D.5}$$

therefore, the Raman intensity for a nanotube parallel with the vertically polarized light and analyzer ($I_{VV}$) is written as

$$I_{VV} = \frac{A}{\sigma\sqrt{2\pi}}\int_{-\pi}^{\pi} cos^4(\theta)\sum_{k=-\infty}^{\infty} exp\left[\frac{-(\theta-\mu+2\pi k)^2}{2\sigma^2}\right] d\theta \tag{D.6}$$

where $\theta$ is the angular degree of misalignment, $\mu$ is the mean (assumed to be zero), and σ is the standard deviation. Similarly, the Raman intensity for a nanotube array with the analyzer and laser polarized horizontal to the alignment direction ($I_{HH}$) is

$$I_{HH} = \frac{A}{\sigma\sqrt{2\pi}}\int_{-\pi}^{\pi} sin^4(\theta)\sum_{k=-\infty}^{\infty} exp\left[\frac{-(\theta-\mu+2\pi k)^2}{2\sigma^2}\right] d\theta. \tag{D.7}$$

Therefore, the Raman intensity anisotropy can be calculated as a function of σ according to,

$$\frac{I_{VV}}{I_{HH}} = \frac{\int_{-\pi}^{\pi} cos^4(\theta)\sum_{k=-\infty}^{\infty} exp\left[\frac{-(\theta-\mu+2\pi k)^2}{2\sigma^2}\right]d\theta}{\int_{-\pi}^{\pi} sin^4(\theta)\sum_{k=-\infty}^{\infty} exp\left[\frac{-(\theta-\mu+2\pi k)^2}{2\sigma^2}\right]d\theta}. \tag{D.8}$$

Raman spectra are collected with a vertically polarized incident laser and vertical analyzer orientation (VV) aligned with the long axis of the aligned nanotubes. This measurement yields the strongest Raman peak intensity of the G-band. With no rotation or translation of the sample, Raman spectra are collected with a horizontally polarized incident laser and horizontal analyzer orientation (HH). From the ratio of the VV and HH G-band intensities ($I_{VV}/I_{HH}$), the optical anisotropy is calculated as discussed above.[2–4] Here, the most aligned sample in the volumetric flow rate series from **Fig. 5.2a and 5.2c** is used as an example. The spectra from the VV and HH orientations, red and black respectively, are shown in **Fig. D2**. Each of the spectra is normalized to the intensity of the Si peak at ~520 $cm^{-1}$. The $I_{VV}/I_{HH}$ in **Fig. D2** is 9.5. Assuming the nanotubes are oriented within a wrapped normal distribution as discussed above, the anisotropy corresponds to a distribution with a half-width at half-maximum (HWHM) of 31.8°. The anisotropy is measured at five different locations on the sample to obtain an average HWHM of 31.3 ± 0.9°.

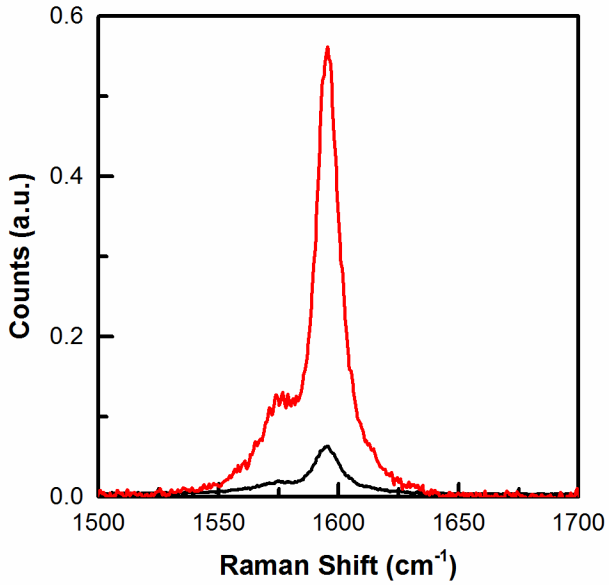


**Figure D2**. Raman spectra of the G-band normalized to the Si peak at ~520 $cm^{-1}$ using VV (red) and HH (black) polarization measured from the nanotube sample with the highest alignment from the volumetric flow rate series in **Fig. 5.2a and 5.2c**.

**D.3 Concentration regime and rotational diffusion coefficient calculation.**

According to Doi-Edwards theory, the semi-dilute regime is the onset when the condition of the number concentration ($c$) is

$$\frac{1}{L^3} \ll c \ll \frac{2\pi}{dL^2} \tag{D.9}$$

where $L$ is the average length of the nanotubes and $d$ is the nanotube diameter.[5–7] The number concentration of nanotubes is approximated by first taking the number of C-atoms in a nanotube with diameter of 1.45 nm and length of 461 nm, which is 36,142 C-atoms, multiplied by the molecular weight of a C atom, which is 12.01 amu. This gives a number concentration of 434,070 amu or $7.2 \times 10^{-22}$ kg per nanotube. As an example ink concentration of 53 µg mL$^{-1}$ in a volume of 350 µL, the number concentration is $7.36 \times 10^{10}$ mm$^{-3}$, which is greater than $\frac{1}{L^3}$ of $1.02 \times 10^{10}$ mm$^{-3}$, and less than $\frac{2\pi}{dL^2}$ of $2.04 \times 10^{13}$ mm$^{-3}$. This places the system in **Fig. 5.2** in a semi-dilute concentration regime. In this regime, there will be some contact between nanotubes (unlike in the infinitely dilute regime as assumed in Equation 5.2 in the Chapter 5). Therefore, on average the degrees of freedom of a given nanotube has been reduced from three to two, which effectively reduces the $D_r$ and makes it easier for the nanotubes to align in shear.[7]

Another factor that must be taken into account when understanding the effect of shear on alignment is the effect of free PFO-BPy polymer within the nanotube ink. The mass ratio of PFO-BPy to nanotubes in solution is 1:1. While it has been shown that the majority of the PFO-BPy wraps the nanotubes when the mass ratio is this low,[8] which minimizes the amount of free polymer, below we instead assume that all of the PFO-BPy is in solution. This assumption provides an upper limit on the effect of free polymer on $D_r$.

If we assume that all of the free polymer is in solution, then the number concentration of PFO-BPy chains is $4.31 \times 10^{11}$ mm$^{-3}$ for a starting ink concentration of 53 µg nanotubes mL$^{-1}$ and 53 µg PFO-BPy mL$^{-1}$ in a volume of 350 µL. This free polymer has been shown to "ball up" into an approximate sphere with a radius of gyration, $R_g$, of 1.2 nm$^2$.[9] This free polymer in solution creates a matrix of these PFO-BPy

"spheres" with which the nanotube will interact, which effectively reduces the nanotube rotational diffusion coefficient. The calculation of the rotational diffusion coefficient of rods in a dilute solution of spheres has been studied by R. Pecora.[10] When using Equation 8 from R. Pecora,[10]

$$D_r^{sph} \propto \frac{k_B T}{6\pi\eta L^4 R N^{\frac{2}{3}}} \tag{D.10}$$

where $k_B$ is the Boltzmann constant, $T$ is the temperature, $\eta$ is the viscosity, $L$ is the length of the rod, $R$ is the radius of the spheres, and $N$ is the number concentration of spheres, we calculate a new $D_r$ within the matrix of PFO-BPy spheres in solution for an average nanotube ($d$ = 1.5 nm, $L$ = 461 nm) to be 227 $s^{-1}$, lower than the $D_r$ = 386 $s^{-1}$ calculated for the same nanotube from Equation 5 from Tirado et al.[11] While not a dramatic reduction of the rotational diffusion coefficient, this approximation shows that the free polymer can retard the rotation of nanotubes, leading to nanotubes that are easier to align via shear.

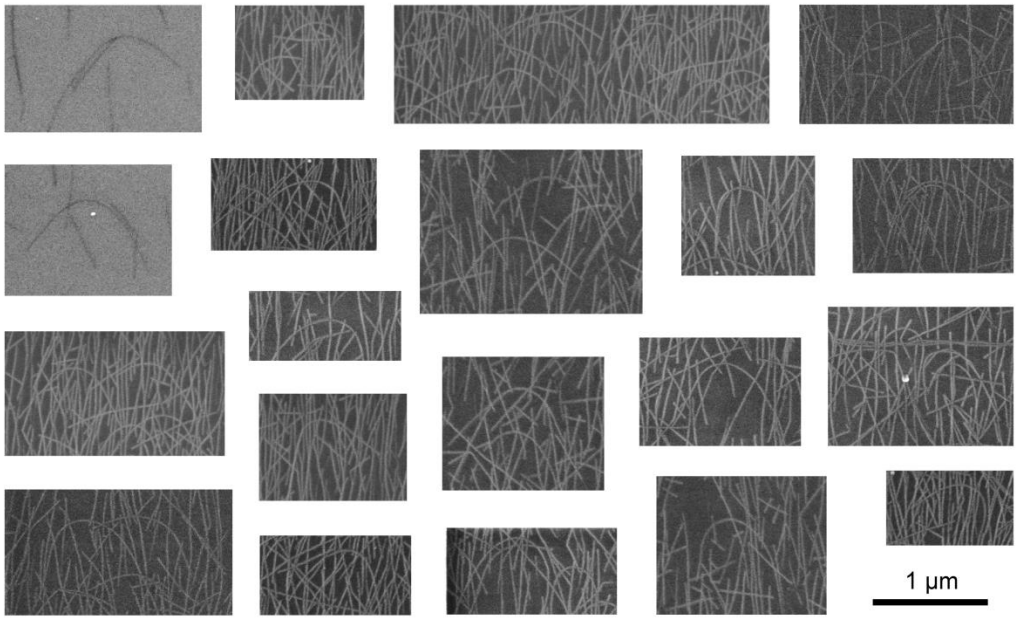


**Figure D3**. Collection of misaligned ‘U’ shaped nanotubes commonly observed in shear aligned carbon nanotube films. The flow direction for all the aligned carbon nanotube films in these images is down from the top of the page.

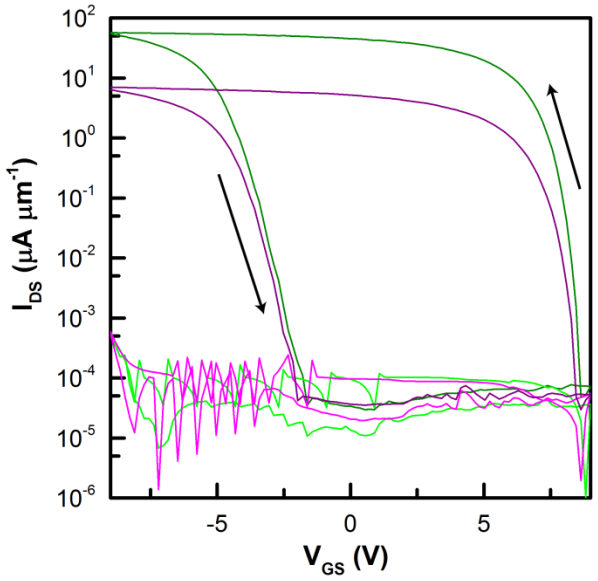


**Figure D4**. Forward (positive to negative $V_{GS}$) and reverse (negative to positive) sweeps of $I_{DS}$ versus $V_{GS}$ from the data ($L_{ch}$ = 1 μm, packing density of 59 μm$^{-1}$) shown in **Fig. 3.4c**. The green and purple curves are from FETs in which the direction of nanotube alignment is parallel and perpendicular, respectively, to the channel. The corresponding gate leakage, $I_{GS}$, from each device is also plotted for the parallel (light green) and perpendicular (pink) nanotube FETs. The hysteresis observed in the full sweeps has been attributed to adsorbed water and oxygen molecules or charge traps on the surface of the oxide, and can be reduced or eliminated via encapsulation,[12] surface treatment,[13] or using hydrophobic substrates.[14]

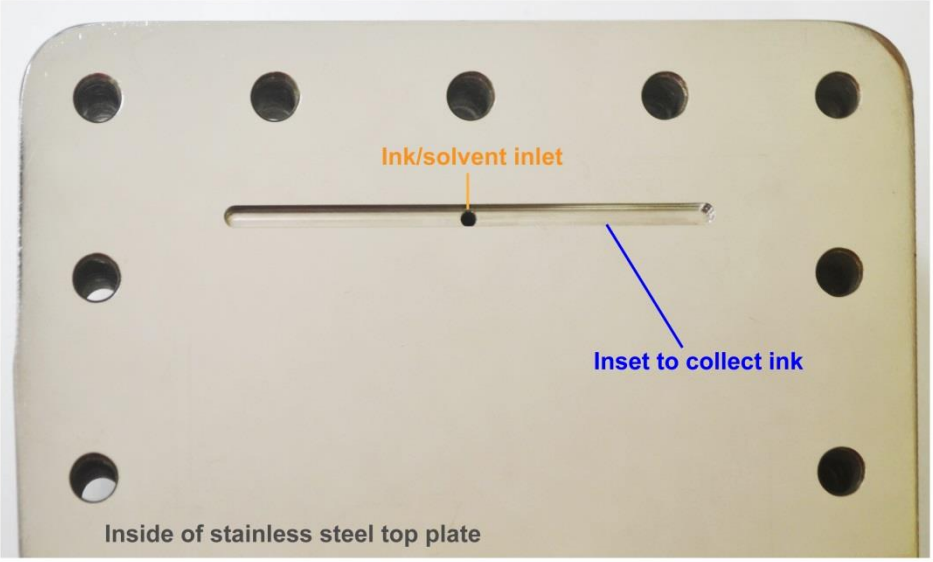


**Figure D5**. Photograph (Nikon D3100) of the inside of the top plate of the scaled shear alignment setup. Similar to the setup in **Fig. 5.1**, the top and bottom plates are held together by bolts along the outside of the substrate through the bolt holes pictured. To achieve a uniform fluid flow across the entire substrate, the inset or trough milled out of the top plate collects the fluid from the ink/solvent inlet before it is forced through the channel mask and across the substrate.

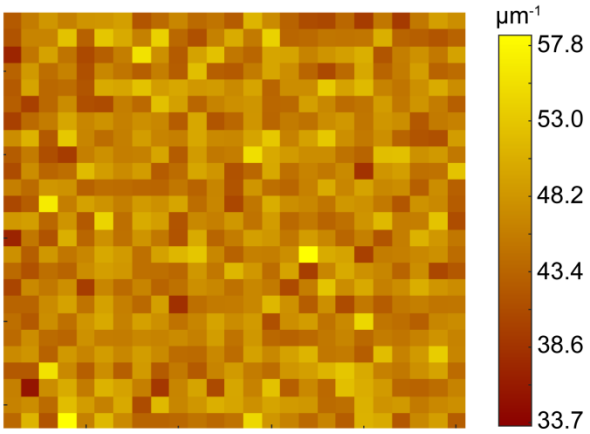


**Figure D6**. Example Raman map from the array of smaller (250 × 250 μm$^2$) Raman maps measured over a 6.8 × 6.0 cm$^2$ area on the aligned nanotube film. The average packing density of this map is 46.1 ± 4.2 μm$^{-1}$.

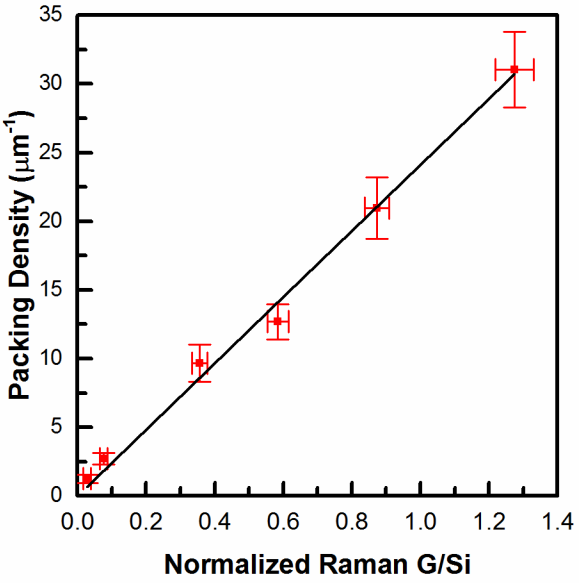


**Figure D7**. Packing density measured via SEM versus normalized Raman G/Si ratio. The best-fit line, with slope of 24.1 $\mu m^{-1}$, is used to convert the Raman G/Si ratio to packing density in the main text.

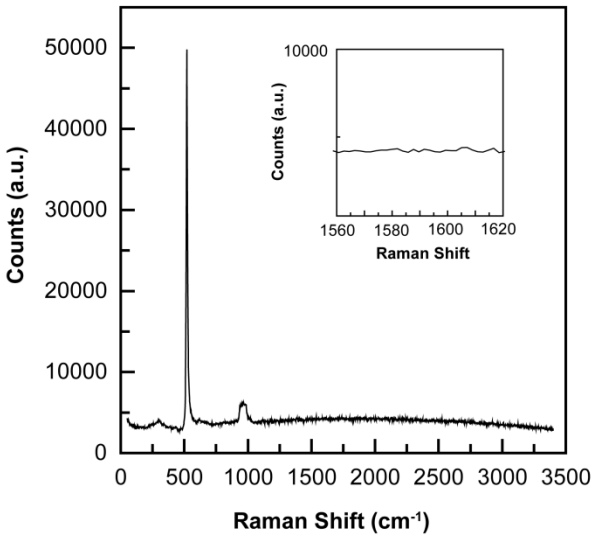


**Figure D8**. Raman spectrum from a control PFO-BPy sample to ensure that no G-band signal is coming from the remaining conjugated PFO-BPy polymer wrapper during Raman spectroscopy of the nanotube films. In this experiment, confined shear alignment is performed with 250 µL of 10 µg $mL^{-1}$ PFO-BPy in chloroform (i.e., without nanotubes in the solution). The sample is boiled in toluene at 120 °C for 1 h and then vacuum annealed at 400 °C for 1 h at ~ $10^{-5}$ Torr prior to the Raman spectroscopy measurement, which is the same procedure conducted before Raman spectroscopy of nanotube films.

# **Appendix E.** Supporting information for Chapter 6

Appendix E was adapted from Jinkins, K. R. & Arnold, M. S. Confined Shear Alignment of Ultrathin Films of Cellulose Nanocrystals. *In preparation*. (2020). K.R.J. and M.S.A. performed all experiments, data collection, and analysis. K.R.J. drafted the manuscript. The cellulose nanocrystals were supplied by Richard S. Reiner at the USDA Forest Products Laboratory.

## E.1 Polarized Raman spectroscopy measurement of alignment in cellulose nanocrystal (CNC) films.

Typical measurements of alignment of CNC assemblies using polarized Raman spectroscopy require the sample or polarizer to be rotated to monitor the change in angle-dependent Raman bands. This rotation is time-consuming and can introduce errors in the measurement. Here, we use a simple method to extract the half-width at half-maximum (HWHM) or spread in alignment of CNCs within assemblies.

First, we extract the angle dependencies of the 1098 and 2890 $cm^{-1}$ Raman bands (obtained with only Raman laser polarization) from published literature.[139]

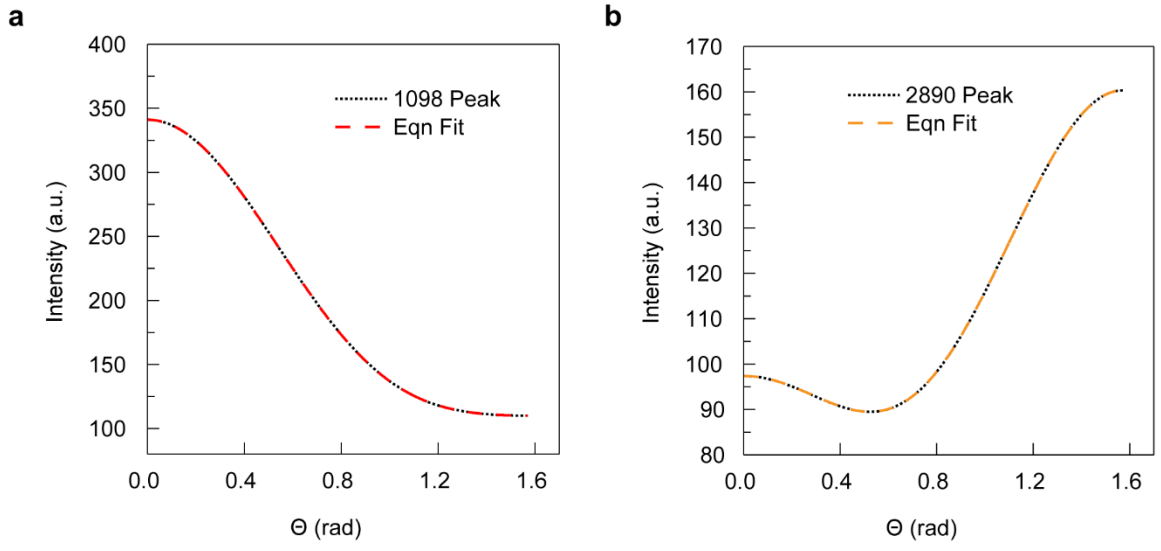


**Figure E1**. Raman intensity and equation fit of 1098 $cm^{-1}$ peak (a) and 2890 $cm^{-1}$ peak (b) as a function of angle (theta) between the polarizer and the long-axis of the cellulose extracted from the literature.

The 1098 $cm^{-1}$ band corresponds to C-O and C-C stretches along the length of the nanocrystal, while the 2890 $cm^{-1}$ band corresponds to the C-H stretches roughly orthogonal to the long-axis of the nanocrystal. The angle relationships of the Raman stretches can be seen above in **Fig. E1**, where the 1098 $cm^{-1}$ peak intensity is maximum when the axis is oriented with the polarizer direction ($\theta = 0$ radians) and decays as the angle between the fiber and the polarizer increases. For the 2890 $cm^{-1}$ peak, the maximum is observed when the fiber and polarizer angle are orthogonal to each other ($\theta = 1.57$ radians). The data relating the dependence of each band intensity to theta in **Fig. E1** are fit to the equations:

$$I_{1098}(\theta) = 341.08 - 427.05\sin^2(\theta) + 196\sin^4(\theta)$$

$$I_{2890}(\theta) = 97.38 - 63.05\sin^2(\theta) + 126\sin^4(\theta).$$

From these equations, the intensities of the 1098 $cm^{-1}$ and 2890 $cm^{-1}$ bands are calculated assuming the CNCs are organized on the substrate in a wrapped normal distribution:

$$f(\theta) = \frac{1}{\sigma\sqrt{2\pi}} \sum_{k=-\infty}^{\infty} exp\left[\frac{-(\theta - \mu + 2\pi k)^2}{2\sigma^2}\right]$$

where $\theta$ is the angle between the laser polarization and the axis of the CNC, $\mu$ is the average orientation (here, the alignment corresponds to 0 radians, so $\mu = 0$), $\sigma$ is the standard deviation of the wrapped normal distribution, and k is the so-called winding number.

Therefore, the Raman intensity of the 1098 $cm^{-1}$ band as a function of angle between the laser polarization and the long axis of the CNC is:

$$I_{1098} = \frac{\int I_{1098}(\theta) * f(\theta) d\theta}{\int f(\theta) d\theta}.$$

Likewise, for the 2890 $cm^{-1}$ band:

$$I_{2890} = \frac{\int I_{2890}(\theta) * f(\theta) d\theta}{\int f(\theta) d\theta}.$$

These Raman intensities are calculated independently as a function of σ and divided to extract a relationship between the 1098/2890 ratio and the standard deviation in alignment, shown in **Fig. E2**.

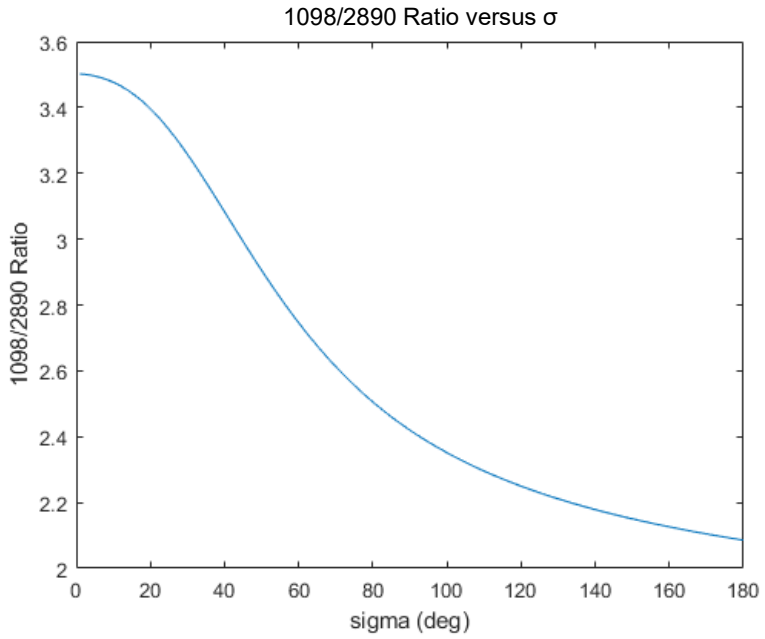


**Figure E2**. Calculated 1098/2890 band ratio as a function of spread in CNC alignment, assuming a wrapped normal distribution.

However, the ratio of the 1098 $cm^{-1}$ and 2890 $cm^{-1}$ bands is dependent upon how much of each bond is present in a given CNC sample and can vary depending on the extraction process and degree of crystallization.[138] Therefore, the relationship shown in **Fig. E2** must be normalized to a sample of CNCs used in the work with a known spread in alignment. We use a randomly oriented CNC sample to normalize this distribution. The random CNC film is deposited by drop-casting CNCs (2 wt%) with 5 mM of $ZnCl_2$ added to the solution to prevent the formation of the chiral nematic structure as the film dried. SEM images and polarized Raman spectroscopy measurements of the random CNC film are shown in **Fig. E3**.

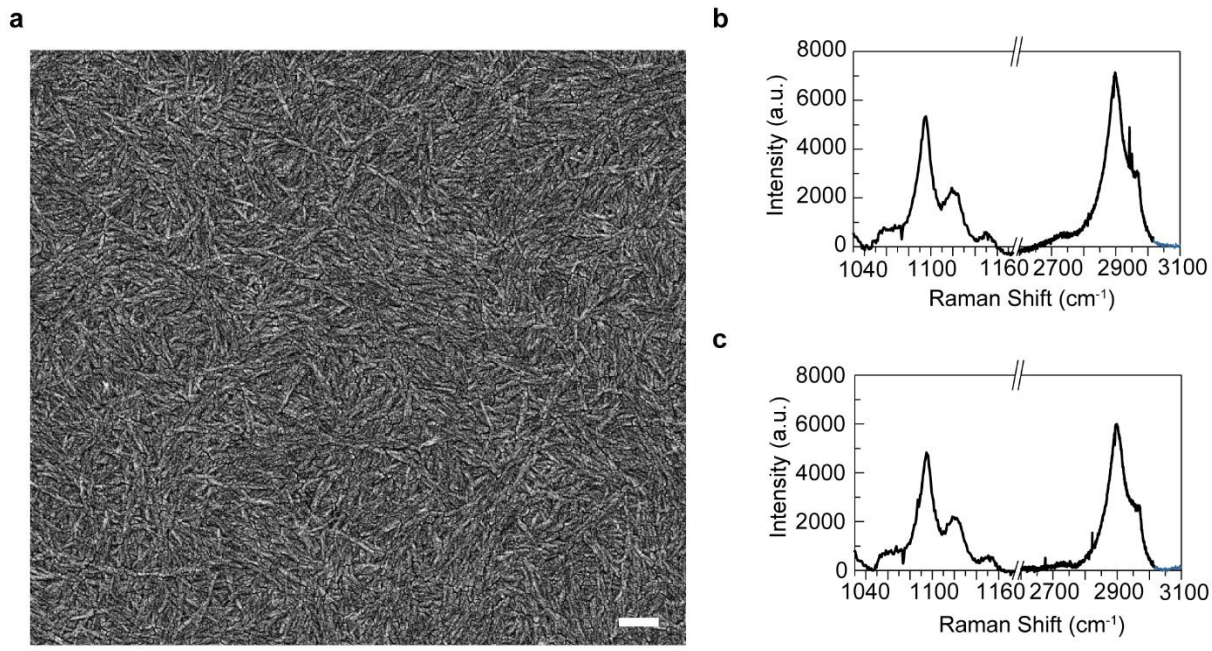


**Figure E3**. Characterization of random CNC film for normalization. (a) SEM image of a random CNC film coated with 10 nm of Pt to enable SEM imaging. (b) and (c) Polarized Raman measurements of 1098 $cm^{-1}$ and 2890 $cm^{-1}$ bands with the sample rotated 90° between measurements. The 1098/2890 ratio for (a) is 0.83 and for (b) is 0.79.

Measurements of the 1098/2890 band ratio are conducted at different locations and at different sample angles to ensure that the film is truly random. These measurements are averaged to find an average 1098/2890 ratio of 0.83 ± 0.10. Using this averaged ratio of the random CNC film, the relationship shown in **Fig. E2** is normalized. The normalized relationship of 1098/2890 ratio versus half-width at half-maximum (HWHM) of spread in alignment of CNCs is shown in **Fig. E4**.

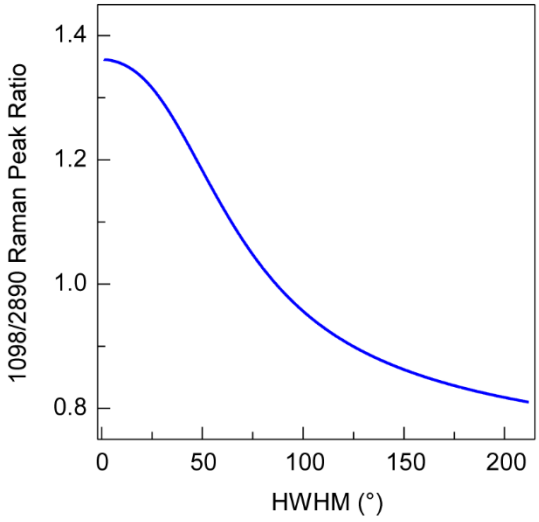


**Figure E4**. Normalized 1098/2890 Raman ratio vs HWHM of CNC alignment.

Finally, this relationship shown in **Fig. E4** is used to directly relate the 1098/2890 ratio from CNC films with the spread in alignment. For example, at an intermediate shear rate of 1900 $s^{-1}$, at one location on the film, the 1098/2890 Raman peak ratio is 1.11, which corresponds to a HWHM of 65°. The 1098/2890 Raman peak ratio and HWHM were measured at five different locations across the sample, resulting in an average HWHM of 65 ± 14°.

# References.


1. Avouris, P., Chen, Z. & Perebeinos, V. Carbon-based Electronics. *Nat. Nanotechnol.* **2**, 605 (2007).
2. Tulevski, G. S. *et al.* Toward High-Performance Digital Logic Technology with Carbon Nanotubes. *ACS Nano* **8**, 8730–8745 (2014).
3. Brady, G. J. *et al.* Polyfluorene-Sorted, Carbon Nanotube Array Field-Effect Transistors with Increased Current Density and High On/Off Ratio. *ACS Nano* **8**, 11614–11621 (2014).
4. Saito, R., Dresselhaus, G. & Dresselhaus, M. S. *Physical Properties of Carbon Nanotubes*. (Imperial College Press, 1998).
5. Lundstrom, M. S. & Antoniadis, D. A. Compact Models and the Physics of Nanoscale FETs. *IEEE Trans. Electron Devices* **61**, 225–233 (2014).
6. Lee, C.-S., Pop, E., Franklin, A. D., Haensch, W. & Wong, H.-S. P. A Compact Virtual-Source Model for Carbon Nanotube FETs in the Sub-10-nm Regime—Part I: Intrinsic Elements. *IEEE Trans. Electron Devices* **62**, 3061–3069 (2015).
7. Franklin, A. D. *et al.* Sub-10 nm Carbon Nanotube Transistor. *Nano Lett.* **12**, 758–762 (2012).
8. Javey, A., Guo, J., Wang, Q., Lundstrom, M. & Dai, H. Ballistic Carbon Nanotube Field-Effect Transistors. *Nature* **424**, 654–657 (2003).
9. Chen, Z., Appenzeller, J., Knoch, J., Lin, Y. & Avouris, P. The Role of Metal−Nanotube Contact in the Performance of Carbon Nanotube Field-Effect Transistors. *Nano Lett.* **5**, 1497–1502 (2005).
10. Bradley, K., Gabriel, J.-C. P. & Grüner, G. Flexible Nanotube Electronics. *Nano Lett.* **3**, 1353–1355 (2003).
11. Cao, Q. *et al.* Medium-scale Carbon Nanotube Thin-Film Integrated Circuits on Flexible Plastic Substrates. *Nature* **454**, 495–500 (2008).
12. Yamada, T. *et al.* A Stretchable Carbon Nanotube Strain Sensor for Human-Motion Detection. *Nat. Nanotechnol.* **6**, 296–301 (2011).
13. Sangwan, V. K. *et al.* Fundamental Performance Limits of Carbon Nanotube Thin-Film Transistors Achieved Using Hybrid Molecular Dielectrics. *ACS Nano* **6**, 7480–7488 (2012).
14. Geier, M. L. *et al.* Solution-processed Carbon Nanotube Thin-film Complementary Static Random Access Memory. *Nat. Nanotechnol.* **10**, 944–948 (2015).
15. Snow, E. S., Novak, J. P., Campbell, P. M. & Park, D. Random Networks of Carbon Nanotubes as an Electronic Material. *Appl. Phys. Lett.* **82**, 2145–2147 (2003).
16. Hu, L., Hecht, D. S. & Grüner, G. Percolation in Transparent and Conducting Carbon Nanotube Networks. *Nano Lett.* **4**, 2513–2517 (2004).
17. Nirmalraj, P. N., Lyons, P. E., De, S., Coleman, J. N. & Boland, J. J. Electrical Connectivity in Single-Walled Carbon Nanotube Networks. *Nano Lett.* **9**, 3890–3895 (2009).
18. Rutherglen, C., Jain, D. & Burke, P. Nanotube Electronics for Radiofrequency Applications. *Nat. Nanotechnol.* **4**, 811–819 (2009).
19. Datta, S. *Quantum Transport: Atom to Transistor*. (Cambridge University Press, 2005).
20. Shulaker, M. M. *et al.* High-performance carbon nanotube field-effect transistors. in *2014 IEEE International Electron Devices Meeting* 33.6.1-33.6.4 (2014). doi:10.1109/IEDM.2014.7047164.
21. Cao, Q. *et al.* Arrays of Single-walled Carbon Nanotubes with Full Surface Coverage for High-performance Electronics. *Nat. Nanotechnol.* **8**, 180–186 (2013).
22. Brady, G. J. *et al.* Quasi-ballistic Carbon Nanotube Array Transistors with Current Density Exceeding Si and GaAs. *Sci. Adv.* **2**, (2016).
23. Liu, X., Han, S. & Zhou, C. Novel Nanotube-on-Insulator (NOI) Approach toward Single-Walled Carbon Nanotube Devices. *Nano Lett.* **6**, 34–39 (2006).
24. Hu, Y. *et al.* Growth of High-density Horizontally Aligned SWNT Arrays using Trojan Catalysts. *Nat. Commun. Lond.* **6**, 6099 (2015).
25. Li, J. *et al.* Growth of High-Density-Aligned and Semiconducting-Enriched Single-Walled Carbon Nanotubes: Decoupling the Conflict between Density and Selectivity. *ACS Nano* **8**, 554–562 (2014).

26. Che, Y. *et al.* Selective Synthesis and Device Applications of Semiconducting Single-Walled Carbon Nanotubes Using Isopropyl Alcohol as Feedstock. *ACS Nano* **6**, 7454–7462 (2012).
27. Nish, A., Hwang, J.-Y., Doig, J. & Nicholas, R. J. Highly Selective Disperion of Single-walled Carbon Nanotubes using Aromatic Polymers. *Nat. Nanotechnol.* **2**, 640–646 (2007).
28. Hersam, M. C. Progress Towards Monodisperse Single-walled Carbon Nanotubes. *Nat. Nanotechnol.* **3**, 387–394 (2008).
29. Lee, H. W. *et al.* Selective Dispersion of High Purity Semiconducting Single-walled Carbon Nanotubes with Regioregular Poly(3-alkylthiophene)s. *Nat. Commun.* **2**, 541 (2011).
30. Mayo, M. L., Hogle, D., Yilmaz, B., Köse, M. E. & Kilina, S. Morphology and Dispersion of Polycarbazole Wrapped Carbon Nanotubes. *RSC Adv.* **3**, 20492 (2013).
31. Rice, N. A. *et al.* Polycarbazole-Sorted Semiconducting Single-Walled Carbon Nanotubes for Incorporation into Organic Thin Film Transistors. *Adv. Electron. Mater.* **5**, 1800539 (2019).
32. Salazar-Rios, J. M. *et al.* Understanding the Selection Mechanism of the Polymer Wrapping Technique toward Semiconducting Carbon Nanotubes. *Small Methods* **2**, 1700335 (2018).
33. Fong, D. & Adronov, A. Recent Developments in the Selective Dispersion of Single-walled Carbon Nanotubes using Conjugated Polymers. *Chem Sci* **8**, 7292–7305 (2017).
34. Remillard, E. M. *et al.* Electric-field Alignment of Aqueous Multi-walled Carbon Nanotubes on Microporous Substrates. *Carbon* **100**, 578–589 (2016).
35. Kordás, K. *et al.* Magnetic-Field Induced Efficient Alignment of Carbon Nanotubes in Aqueous Solutions. *Chem. Mater.* **19**, 787–791 (2007).
36. He, X. *et al.* Wafer-scale Monodomain Films of Spontaneously Aligned Single-walled Carbon Nanotubes. *Nat. Nanotechnol.* **11**, 633–638 (2016).
37. King, B. & Panchapakesan, B. Vacuum Filtration Based Formation of Liquid Crystal Films of Semiconducting Carbon Nanotubes and High Performance Transistor Devices. *Nanotechnology* **25**, 175201 (2014).
38. Puech, N. *et al.* Highly Ordered Carbon Nanotube Nematic Liquid Crystals. *J. Phys. Chem. C* **115**, 3272–3278 (2011).
39. Li, X. *et al.* Langmuir−Blodgett Assembly of Densely Aligned Single-Walled Carbon Nanotubes from Bulk Materials. *J. Am. Chem. Soc.* **129**, 4890–4891 (2007).
40. Sgobba, V. *et al.* Langmuir–Schaefer Films for Aligned Carbon Nanotubes Functionalized with a Conjugate Polymer and Photoelectrochemical Response Enhancement. *ACS Appl. Mater. Interfaces* **6**, 153–158 (2014).
41. Yu, G., Cao, A. & Lieber, C. M. Large-area Blown Bubble Films of Aligned Nanowires and Carbon Nanotubes. *Nat. Nanotechnol.* **2**, 372–377 (2007).
42. Si, J. *et al.* Scalable Preparation of High-Density Semiconducting Carbon Nanotube Arrays for High-Performance Field-Effect Transistors. *ACS Nano* **12**, 627–634 (2018).
43. Hedberg, J., Dong, L. & Jiao, J. Air Flow Technique for Large Scale Dispersion and Alignment of Carbon Nanotubes on Various Substrates. *Appl. Phys. Lett.* **86**, 143111 (2005).
44. Lay, M. D., Novak, J. P. & Snow, E. S. Simple Route to Large-Scale Ordered Arrays of Liquid-Deposited Carbon Nanotubes. *Nano Lett.* **4**, 603–606 (2004).
45. Kim, P. & Kang, T. J. Large-area Fluidic Assembly of Single-walled Carbon Nanotubes through Dip-coating and Directional Evaporation. *Micro Nano Syst. Lett.* **5**, (2017).
46. Joo, Y., Brady, G. J., Arnold, M. S. & Gopalan, P. Dose-Controlled, Floating Evaporative Self-assembly and Alignment of Semiconducting Carbon Nanotubes from Organic Solvents. *Langmuir* **30**, 3460–3466 (2014).
47. Liu, L. *et al.* Aligned, High-density Semiconducting Carbon Nanotube Arrays for High-performance Electronics. *Science* **368**, 850–856 (2020).
48. Cao, Q., Tersoff, J., Farmer, D. B., Zhu, Y. & Han, S.-J. Carbon Nanotube Transistors Scaled to a 40-nanometer Footprint. *Science* **356**, 1369–1372 (2017).
49. Qiu, C. *et al.* Scaling Carbon Nanotube Complementary Transistors to 5-nm Gate Lengths. *Science* **355**, 271–276 (2017).

50. Dürkop, T., Getty, S. A., Cobas, E. & Fuhrer, M. S. Extraordinary Mobility in Semiconducting Carbon Nanotubes. *Nano Lett.* **4**, 35–39 (2004).
51. Avouris, P., Appenzeller, J., Martel, R. & Wind, S. J. Carbon Nanotube Electronics. *Proc. IEEE* **9**, 1772–1784 (2003).
52. Iakoubovskii, K. Techniques of Aligning Carbon Nanotubes. *Open Phys.* **7**, (2009).
53. Li, H., Hain, T. C., Muzha, A., Schöppler, F. & Hertel, T. Dynamical Contact Line Pinning and Zipping during Carbon Nanotube Coffee Stain Formation. *ACS Nano* **8**, 6417–6424 (2014).
54. Shastry, T. A. *et al.* Large-Area, Electronically Monodisperse, Aligned Single-Walled Carbon Nanotube Thin Films Fabricated by Evaporation-Driven Self-Assembly. *Small* **9**, 45–51 (2013).
55. Zhang, S.-Y., Liu, J.-W., Zhang, C.-L. & Yu, S.-H. Co-assembled Thin Films of Ag Nanowires and Functional Nanoparticles at the Liquid–Liquid Interface by Shaking. *Nanoscale* **5**, 4223 (2013).
56. Kim, K. *et al.* Interfacial Liquid-state Surface-enhanced Raman Spectroscopy. *Nat. Commun.* **4**, (2013).
57. Biswas, S. & Drzal, L. T. A Novel Approach to Create a Highly Ordered Monolayer Film of Graphene Nanosheets at the Liquid−Liquid Interface. *Nano Lett.* **9**, 167–172 (2009).
58. Matsui, J. *et al.* Fabrication of Densely Packed Multi-walled Carbon Nanotube Ultrathin Films using a Liquid–liquid Interface. *J. Mater. Chem.* **17**, 3806 (2007).
59. Binder, W. H. Supramolecular Assembly of Nanoparticles at Liquid–Liquid Interfaces. *Angew. Chem. Int. Ed.* **44**, 5172–5175 (2005).
60. Schwenke, K., Isa, L. & Del Gado, E. Assembly of Nanoparticles at Liquid Interfaces: Crowding and Ordering. *Langmuir* **30**, 3069–3074 (2014).
61. Zhang, Y. *et al.* Langmuir Films and Uniform, Large Area, Transparent Coatings of Chemically Exfoliated $MoS_2$ Single Layers. *J. Mater. Chem. C* **5**, 11275–11287 (2017).
62. DeCamp, S. J., Redner, G. S., Baskaran, A., Hagan, M. F. & Dogic, Z. Orientational Order of Motile Defects in Active Nematics. *Nat. Mater.* **14**, 1110–1115 (2015).
63. Jordens, S., Isa, L., Usov, I. & Mezzenga, R. Non-equilibrium Nature of Two-dimensional Isotropic and Nematic Coexistence in Amyloid Fibrils at Liquid Interfaces. *Nat. Commun.* **4**, (2013).
64. Matsui, J. *et al.* Simple Fabrication of Carbon Nanotube Monolayer Film. *Chem. Lett.* **35**, 42–43 (2006).
65. Wang, H. & Hobbie, E. K. Amphiphobic Carbon Nanotubes as Macroemulsion Surfactants. *Langmuir* **19**, 3091–3093 (2003).
66. Zhang, Y. *et al.* Directing Single-walled Carbon Nanotubes to Self-assemble at Water/oil Interfaces and Facilitate Electron Transfer. *Chem. Commun.* 4273 (2008) doi:10.1039/b805789c.
67. Feng, T., Hoagland, D. A. & Russell, T. P. Assembly of Acid-Functionalized Single-Walled Carbon Nanotubes at Oil/Water Interfaces. *Langmuir* **30**, 1072–1079 (2014).
68. Matsui, J., Yamamoto, K. & Miyashita, T. Assembly of Untreated Single-walled Carbon Nanotubes at a Liquid–liquid Interface | Elsevier Enhanced Reader. *Carbon* **47**, 1444–1450 (2009).
69. Zhang, S. & Kumar, S. Carbon Nanotubes as Liquid Crystals. *Small* **4**, 1270–1283 (2008).
70. Kleinerman, O. *et al.* Direct Imaging of Carbon Nanotube Liquid-Crystalline Phase Development in True Solutions. *Langmuir* **33**, 4011–4018 (2017).
71. Lee, H. W. *et al.* Lyotropic Liquid-Crystalline Solutions of High-Concentration Dispersions of Single-Walled Carbon Nanotubes with Conjugated Polymers. *Small* **5**, 1019–1024 (2009).
72. Zhang, S., Kinloch, I. A. & Windle, A. H. Mesogenicity Drives Fractionation in Lyotropic Aqueous Suspensions of Multiwall Carbon Nanotubes. *Nano Lett.* **6**, 568–572 (2006).
73. Badaire, S. *et al.* Liquid Crystals of DNA-Stabilized Carbon Nanotubes. *Adv. Mater.* **17**, 1673–1676 (2005).
74. Ko, H. & Tsukruk, V. V. Liquid-Crystalline Processing of Highly Oriented Carbon Nanotube Arrays for Thin-Film Transistors. *Nano Lett.* **6**, 1443–1448 (2006).
75. Jinkins, K. R. *et al.* Nanotube Alignment Mechanism in Floating Evaporative Self-Assembly. *Langmuir* **33**, 13407–13414 (2017).

76. Brady, G. J., Jinkins, K. R. & Arnold, M. S. Channel Length Scaling Behavior in Transistors Based on Individual versus Dense Arrays of Carbon Nanotubes. *J. Appl. Phys.* **122**, 124506 (2017).
77. Cao, Y. *et al.* Radio Frequency Transistors Using Aligned Semiconducting Carbon Nanotubes with Current-Gain Cutoff Frequency and Maximum Oscillation Frequency Simultaneously Greater than 70 GHz. *ACS Nano* **10**, 6782–6790 (2016).
78. Rutherglen, C. *et al.* Wafer-scalable, Aligned Carbon Nanotube Transistors Operating at Frequencies of over 100 GHz. *Nat. Electron.* **2**, 530–539 (2019).
79. Mirri, F. *et al.* High-Performance Carbon Nanotube Transparent Conductive Films by Scalable Dip Coating. *ACS Nano* **6**, 9737–9744 (2012).
80. Xiang, L. *et al.* Carbon Nanotube Dual-material Gate Devices for Flexible Configurable Multifunctional Electronics. *Carbon* **161**, 656–664 (2020).
81. Larson, R. G. *The Structure and Rheology of Complex Fluids*. (Oxford University Press).
82. Lu, L. & Chen, W. Large-Scale Aligned Carbon Nanotubes from Their Purified, Highly Concentrated Suspension. *ACS Nano* **4**, 1042–1048 (2010).
83. Song, W. & Windle, A. H. Size-Dependence and Elasticity of Liquid-Crystalline Multiwalled Carbon Nanotubes. *Adv. Mater.* **20**, 3149–3154 (2008).
84. Zakri, C. *et al.* Liquid crystals of Carbon Nanotubes and Graphene. *Philos. Trans. R. Soc. Math. Phys. Eng. Sci.* **371**, 20120499 (2013).
85. Onsager, L. The Effects of Shape on the Interaction of Colloidal Particles. *N Acad Sci* **51**, 627–659 (1949).
86. Khokhlov, A. R. & Semenov, A. N. Liquid-Crystalline Ordering in the Solution of Long Persistent Chains. *Physica* **108A**, 546–556 (1981).
87. Puica, M.-R. Lyotropic Liquid Crystals at Phase Transitions. 28.
88. Mistry, K., Larsen, B. & Blackburn, J. High-Yield Dispersions of Large-Diameter Semiconducting Single-Walled Carbon Nanotubes with Tunable Narrow Chirality Distributions. *ACS Nano* **7**, 2231–2239 (2013).
89. Appenzeller, J. *et al.* Carbon Nanotube Electronics. *IEEE Trans. Nanotechnol.* **1**, 184–189 (2002).
90. Jinkins, K. R. *et al.* 2D Nematic Carbon Nanotube Assemblies Aligned by Flow. *Prep.* (2020).
91. Dwyer, J. H. *et al.* Solvent-Mediated Affinity of Polymer-Wrapped Single-Walled Carbon Nanotubes for Chemically Modified Surfaces. *Langmuir* **35**, 12492–12500 (2019).
92. Shea, M. J. & Arnold, M. S. 1% Solar Cells Derived from Ultrathin Carbon Nanotube Photoabsorbing Films. *Appl. Phys. Lett.* **102**, 243101 (2013).
93. Wang, J. *et al.* Role of Defects as Exciton Quenching Sites in Carbon Nanotube Photovoltaics. *J. Phys. Chem. C* **121**, 8310–8318 (2017).
94. Han, E. & Gopalan, P. Cross-Linked Random Copolymer Mats As Ultrathin Nonpreferential Layers for Block Copolymer Self-Assembly. *Langmuir* **26**, 1311–1315 (2010).
95. Salvetat, J.-P. *et al.* Mechanical properties of Carbon Nanotubes. *Appl. Phys. A* **69**, 255–260 (1999).
96. Huang, Y., Duan, X., Wei, Q. & Lieber, C. M. Directed Assembly of One-Dimensional Nanostructures into Functional Networks. *Science* **291**, 630–633 (2001).
97. Gang, A. *et al.* Microfluidic Alignment and Trapping of 1D Nanostructures – a Simple Fabrication Route for Single-nanowire Field Effect Transistors. *RSC Adv* **5**, 94702–94706 (2015).
98. Kim, P., Baik, S. & Suh, K. Y. Capillarity-Driven Fluidic Alignment of Single-Walled Carbon Nanotubes in Reversibly Bonded Nanochannels. *Small* **4**, 92–95 (2008).
99. Li, J., Zhang, Q., Yan, Y., Li, S. & Chen, L. Fabrication of Carbon Nanotube Field-Effect Transistors by Fluidic Alignment Technique. *IEEE Trans. Nanotechnol.* **6**, 481–484 (2007).
100. Zhu, R., Lai, Y., Nguyen, V. & Yang, R. Scalable Alignment and Transfer of Nanowires in a Spinning Langmuir Film. *Nanoscale* **6**, 11976–11980 (2014).
101. Lay, M. D., Novak, J. P. & Snow, E. S. Simple Route to Large-Scale Ordered Arrays of Liquid-Deposited Carbon Nanotubes. *Nano Lett.* **4**, 603–606 (2004).
102. Camponeschi, E. *et al.* Uniform Directional Alignment of Single-Walled Carbon Nanotubes in Viscous Polymer Flow. *Langmuir* **22**, 1858–1862 (2006).

103. Tannous, C. Orientation Control of Rodlike Objects by Flow. *ArXiv09050091 Phys.* (2009).
104. Jinkins, K., R. *et al.* Nanotube Alignment Mechanism in Floating Evaporative Self-Assembly. *Langmuir* **33**, 13407–13414 (2017).
105. Tirado, M. M., Martinez, C. L. & de la Torre, J. G. Comparison of Theories for the Translational and Rotational Diffusion Coefficients of Rod-like Macromolecules. Application to Short DNA Fragments. *J. Chem. Phys.* **81**, (1984).
106. Gerashchenko, S. & Steinberg, V. Statistics of Tumbling of a Single Polymer Molecule in Shear Flow. *Phys. Rev. Lett.* **96**, (2006).
107. Celani, A., Puliafito, A. & Turitsyn, K. Polymers in Linear Shear Flow: a Numerical Study. *Europhys. Lett. EPL* **70**, 464–470 (2005).
108. Joo, Y. *et al.* Isolation of Pristine Electronics Grade Semiconducting Carbon Nanotubes by Switching the Rigidity of the Wrapping Polymer Backbone on Demand. *ACS Nano* **9**, 10203–10213 (2015).
109. Joo, Y. *et al.* Polymer-Free Electronic-Grade Aligned Semiconducting Carbon Nanotube Array. *ACS Appl. Mater. Interfaces* **9**, 28859–28867 (2017).
110. Engel, M. *et al.* Thin Film Nanotube Transistors Based on Self-Assembled, Aligned, Semiconducting Carbon Nanotube Arrays. *ACS Nano* **2**, 2445–2452 (2008).
111. Maruyama, T., Kozawa, A., Saida, T., Naritsuka, S. & Iijima, S. Low Gemperature Growth of Single-walled Carbon Nanotubes from Rh Catalysts. *Carbon* **116**, 128–132 (2017).
112. Habibi, Y., Lucia, L. A. & Rojas, O. J. Cellulose Nanocrystals: Chemistry, Self-Assembly, and Applications. *Chem. Rev.* **110**, 3479–3500 (2010).
113. Moon, R. J., Martini, A., Nairn, J., Simonsen, J. & Youngblood, J. Cellulose Nanomaterials Review: Structure, Properties and Nanocomposites. *Chem. Soc. Rev.* **40**, 3941 (2011).
114. Dri, F. L., Hector, L. G., Moon, R. J. & Zavattieri, P. D. Anisotropy of the Elastic Properties of Crystalline Cellulose Iβ from First Principles Density Functional Theory with Van der Waals Interactions. *Cellulose* **20**, 2703–2718 (2013).
115. Frka-Petesic, B., Jean, B. & Heux, L. First Experimental Evidence of a Giant Permanent Electric-Dipole Moment in Cellulose Nanocrystals. *EPL Europhys. Lett.* **107**, 28006 (2014).
116. Rajala, S. *et al.* Cellulose Nanofibril Film as a Piezoelectric Sensor Material. *ACS Appl. Mater. Interfaces* **8**, 15607–15614 (2016).
117. Pirich, C. L., de Freitas, R. A., Torresi, R. M., Picheth, G. F. & Sierakowski, M. R. Piezoelectric Immunochip Coated with Thin Films of Bacterial Cellulose Nanocrystals for Dengue Detection. *Biosens. Bioelectron.* **92**, 47–53 (2017).
118. Kargl, R. *et al.* Selective Immobilization and Detection of DNA on Biopolymer Supports for the Design of Microarrays. *Biosens. Bioelectron.* **68**, 437–441 (2015).
119. Wolfberger, A. *et al.* Photolithographic Patterning of Cellulose: a Versatile Dual-tone Photoresist for Advanced Applications. *Cellulose* **22**, 717–727 (2015).
120. Manfredi, G., Mayrhofer, C., Kothleitner, G., Schennach, R. & Comoretto, D. Cellulose Ternary Photonic Crystal Created by Solution Processing. *Cellulose* **23**, 2853–2862 (2016).
121. Kontturi, E. & Spirk, S. Ultrathin Films of Cellulose: A Materials Perspective. *Front. Chem.* **7**, 488 (2019).
122. Kontturi, E., Tammelin, T. & Österberg, M. Cellulose—model Films and the Fundamental Approach. *Chem Soc Rev* **35**, 1287–1304 (2006).
123. Habibi, Y., Hoeger, I., Kelley, S. S. & Rojas, O. J. Development of Langmuir−Schaeffer Cellulose Nanocrystal Monolayers and Their Interfacial Behaviors. *Langmuir* **26**, 990–1001 (2010).
124. Notley, S. M., Eriksson, M., Wågberg, L., Beck, S. & Gray, D. G. Surface Forces Measurements of Spin-Coated Cellulose Thin Films with Different Crystallinity. *Langmuir* **22**, 3154–3160 (2006).
125. Edgar, C. D. & Gray, D. G. Smooth Model Cellulose I Surfaces from Nanocrystal Suspensions. 8.
126. Fleming, K., Gray, D. G. & Matthews, S. Cellulose Crystallites. *Chem Eur J* **7**, 1831–1835 (2001).
127. Wang, J. *et al.* Piezoelectric Nanocellulose Thin Film with Large-Scale Vertical Crystal Alignment. *ACS Appl. Mater. Interfaces* **12**, 26399–26404 (2020).

128. Lagerwall, J. P. F. *et al.* Cellulose Nanocrystal-based Materials: From Liquid Crystal Self-assembly and Glass Formation to Multifunctional Thin Films. *NPG Asia Mater.* **6**, e80–e80 (2014).
129. Shrestha, S., Diaz, J. A., Ghanbari, S. & Youngblood, J. P. Hygroscopic Swelling Determination of Cellulose Nanocrystal (CNC) Films by Polarized Light Microscopy Digital Image Correlation. *Biomacromolecules* **18**, 1482–1490 (2017).
130. Cranston, E. D. & Gray, D. G. Formation of Cellulose-based Electrostatic Layer-by-layer Films in a Magnetic Field. *Sci. Technol. Adv. Mater.* **7**, 319–321 (2006).
131. Sugiyama, J., Chanzy, H. & Maret, G. Orientation of Cellulose Microcrystals by Strong Magnetic Fields. *Macromolecules* **25**, 4232–4234 (1992).
132. Bordel, D., Putaux, J.-L. & Heux, L. Orientation of Native Cellulose in an Electric Field. *Langmuir* **22**, 4899–4901 (2006).
133. Habibi, Y., Heim, T. & Douillard, R. AC Electric Field-assisted Assembly and Alignment of Cellulose Nanocrystals. *J. Polym. Sci. Part B Polym. Phys.* **46**, 1430–1436 (2008).
134. Hoeger, I., Rojas, O. J., Efimenko, K., Velev, O. D. & Kelley, S. S. Ultrathin Film Coatings of Aligned Cellulose Nanocrystals from a Convective-shear Assembly System and their Surface Mechanical Properties. *Soft Matter* **7**, 1957 (2011).
135. Jinkins, K. R., Chan, J., Jacobberger, R. M., Berson, A. & Arnold, M. S. Substrate-Wide Confined Shear Alignment of Carbon Nanotubes for Thin Film Transistors. *Adv. Electron. Mater.* **5**, 1800593 (2019).
136. Zimmerley, M. *et al.* Molecular Orientation in Dry and Hydrated Cellulose Fibers: A Coherent Anti-Stokes Raman Scattering Microscopy Study. *J. Phys. Chem. B* **114**, 10200–10208 (2010).
137. Gierlinger, N. *et al.* Cellulose microfibril orientation of Picea abies and its Variability at the Micron-level Determined by Raman Imaging. *J. Exp. Bot.* **61**, 587–595 (2010).
138. Agarwal, U. P. Raman Spectroscopy of CNC- and CNF-Based Nanocomposites. in *Handbook of Nanocellulose and Cellulose Nanocomposites* (eds. Kargarzadeh, H., Ahmad, I., Thomas, S. & Dufresne, A.) 609–625 (Wiley-VCH Verlag GmbH & Co. KGaA, 2017). doi:10.1002/9783527689972.ch18.
139. Wiley, J. H. & Atalla, R. H. Band Assignments in the Raman Spectra of Celluloses. *Carbohydr. Res.* **160**, 113–129 (1987).
140. Reiner, R. S. Process Scale-Up of Cellulose Nanocrystal Production to 25 kg per Batch at the Forest Products Laboratory. 6.
141. Hwang, J. *et al.* Polarized Spectroscopy of Aligned Single-wall Carbon Nanotubes. *Phys. Rev. B* **62**, R13310–R13313 (2000).